Improved Boundary Layer Heat Transfer Calculations near a Stagnation Point

Final Report

Dr. Ibrahim

Period Covered: 5/1/89 to 9/11/89

Cleveland State University
1983 East 24th Street
Cleveland, Ohio 44115

Grant Number: NCC 3-50

TRANSIENT THERMAL ANALYSIS OF A BRAYTON CYCLE SOLAR DYNAMIC HEAT RECEIVER

KYUNG HWAN AHN

Bachelor of Science in Mechanical Engineering

Sung Kyun Kwan University

February, 1981

Master of Science in Mechanical Engineering

Youngstown State University

March, 1985

submitted in partial fulfillment of requirements for the degree

DOCTOR OF ENGINEERING

at the

CLEVELAND STATE UNIVERSITY

March, 1990

TRANSIENT THERMAL ANALYSIS OF A BRAYTON CYCLE SOLAR DYNAMIC HEAT RECEIVER

KYUNG-HWAN AHN

ABSTRACT

In the present investigation a thermal design of solar receiver has been developed for the solutions of problems involving phase-change thermal energy storage and natural convection loss. Two dimensional axisymmetrical solidification and melting of materials contained between two concentric cylinders of finite length has been studied for thermal energy storage analysis. For calculation of free convection loss inside receiver cavity, two dimensional axisymmetrical, laminar, transient free convection including radiation effects has been studied using integral/finite difference method. Finite difference equations are derived for the above analysis subject to constant or variable material properties, initial and boundary conditions. The validity of the analyses has been substantiated by comparing results of the present general method with available analytic solutions or numerical results reported in the literature. Both explicit and implicit schemes are tested in phase change analysis with different number of nodes ranging from 4 to 18.

The above numerical methods have been applied to the existing solar receiver analizing computer code as additional subroutines. The results were computed for one of the proposed Brayton cycle solar receiver models running under the actual environmental conditions. Effect of thermal energy storage on the thermal behavour of the receiver has been estimated. Due to the thermal energy storagy, about 65% reduction on working gas outlet temperature fluctuation has

This dissertation has been approved for the Department of Mechanical Engineering and the College of Graduate Studies by

_____
Dissertation Committee Chairperson

_____
(Department/Date)

_____

_____
(Department/Date)

_____

_____
(Department/Date)

_____

_____
(Department/Date)

_____

_____
(Department/Date)

_____

_____
(Department/Date)

been obtained, however maximum temperature of thermal energy storage containment has been increased about 18%.

Also, effect of natural convection inside a receiver cavity on the receiver heat transfer has been analyzed. The finding indicated that thermal stratification occurs during the sun time resulting in higher receiver temperatures at the outlet section of the gas tube, and lower temperatures at the inlet section of the gas tube when compared with the results with no natural convection. Due to heat supply from the air during the shade time, minimum temperature has been increased, while maximum temperature has been reduced due to convection loss to air. Consequently, cyclic temperature fluctuation has been reduced 29% for working gas and 16% for thermal energy storage containment. Despite of the presence of the natural convection, on the other hand, the time-averaged temperatures for receiver components were found to be similar for two cases with/without natural convection (maximum difference was 1.8%).

TABLE OF CONTENTS

LIST OF TABLES

LIST OF FIGURES

NOMENCLATURE

a	Exponent of temperature profile
A	Aspect ratio, L/r_T
A_o	Area of receiver aperture
A_i	Area of node i
b	Wall thickness
B	$\frac{NP\pi Dh}{\dot{m}Cp_G}$
$C(i,j)$	Thermal conductance between node i and j
Cp	Specific heat
D	Diameter of the gas tube
E	Solid-liquid interface position in axial direction
$f(r')$	Normalized velocity distribution in boundary layer
$\mathcal{F}_{\mathcal{A}}$	Total radiation view factor to aperture
$\mathcal{F}(i,j)$	Total radiation view factor from node i to node j
g	Acceleration of gravity
$g(r')$	Normalized temperature distribution in boundary layer
h	Convective heat transfer coefficient
H	Depth of mixing region

k	Thermal conductivity
k_s	Thermal conductivity of solid PCM
k_l	Thermal conductivity of liquid PCM
k_f	Thermal conductivity of fluid
L	Axial length of the cylinder
M	Total number of mesh points in axial direction
N	Total number of mesh points in radial direction
$\dot{m}$	Mass flow rate of gas
NP	Number of the gas tubes
Nu	Nusselt number, $h\,z/k$
P	Pressur
PCM	Phase change material
Pr	Prandtl number, ν_f/α_f
q_I	Insulation loss flux
q_w	Wall heat flux
Q	Heat transfer
Q^*	Dimensionless heat transfer
$\dot{Q}_A$	Rate of energy loss through aperture
$\dot{Q}_G$	Rate of energy extracted by gas
$\dot{Q}_I$	Rate of energy loss through insulation
$\dot{Q}_L$	Rate of energy loss
$\dot{Q}_S$	Rate of solar energy input
$\dot{Q}_{ST}$	Energy stored during sun period
r	Radial coordinate
r'	Non-dimensional radial coordinate, r/δ_0
r_T	Total radius of cylindrical enclosures

r_{in}	Inner radius
r^*	Ratio, $\delta R/\Delta R$
R	Dimensionless radial coordinate, $(r - r_{in})/r_{in}$
Ra	Rayleigh number, $\frac{g\,\beta_f\,r_T^3(T-T_c)}{\nu_f\,\alpha_f}$
Ra_w	Rayleigh number at wall, $\frac{g\,\beta_f\,r_T^3(T_w-T_c)}{\nu_f\,\alpha_f}$
S	Shear stress
t	Time coordinate
t'	Non-dimensionalized time defined in Equation 3.12
T	Temperature
TES	Thermal energy storage
T_c	Core fluid temperature
T_w	Wall temperature
T_G	Gas temperature
T_I	Initial temperature
T_m	Melting (or solidification) temperature
T_M	Temperature of the mixing region
T_p	Constant boundary temperature around upper perimeter of enclosure
T_∞	Ambient temperature
U	Axial velocity of boundary layer
U'	Non-dimensionalized axial velocity of boundary layer defined in Equation 3.12
U_c	Axial velocity of core fluid
U_m	Maximum axial velocity at any height
$U_{i,j}$	Overall heat transfer coefficient at node (i,j)
$U^*_{i,j}$	Dimensionless overall heat transfer coefficient at node (i,j)
z	Axial coordinate
Z	Dimensionless axial coordinate, z/r_{in}

Greek symbols

α	Thermal diffusivity
α_w	Thermal diffusivity of wall
α_f	Thermal diffusivity of fluid
β_f	Coefficient of volumetric expansion of fluid
γ	Dimensionless material property, $k\,L/(k_s\,C_p\,T_m)$
δ_0	Boundary layer thickness defined at $U = 0$
δR	Radial space quotient defined in Figure 2.2, $-0.5\Delta R \leq \delta R \leq 0.5\Delta R$
η	Non-dimensional boundary layer thickness, δ_0 / r_T
θ	Normalized temperature difference between wall and core fluid temperature, $\frac{T_w - T_c}{T_p - T_I}$
ν_f	Kinemetic viscosity of fluid
ρ	Density
σ	Stefan-Boltzman radiation constant
ΔR	Radial space step size
ΔS	Space step along the boundary under consideration
Δt_{shade}	Length of shade period
Δt_{sun}	Length of sun
ΔT	Temperature difference, $T_p - T_I$
ΔZ	Axial space step size
τ	Dimensionless time coordinate, $\frac{T_m\,k_f}{\rho\,L\,r_{in}^2}\,t$
Θ	Dimensionless temperature, $(T - T_m)/T_m$

CHAPTER I

INTRODUCTION

In engineering practice, industrial processes, and laboratory work it is often necessary to find the temperature distribution and heat flow in bodies under transient conditions. Among these transient heat transfer problems, attention is given for cases involved in phase change of a material and natural convection inside an enclosure.

1.) Case related to Phase change of a material: heat transfer due to solidification or melting of materials is of considerable importance in many technical fields. Recent interest in the storage of thermal energy from intermittent sources such as the sun, as well as ongoing interest in many processes in metal casting, food freezing, aerodynamic heating of high speed traveling objects such as missiles and space craft and freezing or thawing of soil, etc. has highlighted the importances of phase change phenemena.

2.) Case related to natural convection inside an enclosure: heat transfer due to bouyance-driven flow of the fluid contained in a solid boundaries is encounted in many engineering applications, including the storage of cryogenic fluids, petroleum storage vessels , air circulation in the building. In all these cases, the heat loss from or to the enclosure is an important problem. Chapter II provides extensive literature survey for the two-dimensional

axisymmetrical solidification and melting problem. This is followed by a detailed presentation of the different numerical methods used along with results and comparisons for sample cases. Similarly, in chapter III, numerical derivation of a heating process by the natural convection is given with a related literature survey. In chapter IV, these numerical methods are applied to thermal analyses of the solar receiver of the space station freedom solar dynamic power system by incorporating the phase change subroutine developed in Chapter II and the natural convection subroutine in Chapter III to the existing receiver program, namely HEAP code, which will discussed later. In addition, several sensitivity analysis will be conducted to examine the receiver thermal performance.

1.1 Energy Storage Solar Dynamic Receiver

1.1.1 *Background* A solar dynamic power system for generation of auxiliary electrical power in space has been recently developed using solar energy as heat source. A thermodynamic power cycle for such system is the closed-loop Brayton cycle (see Figure 1.1). The solar Brayton heat receiver is a combination of heat exchanger and heat storage device which transfers energy to a Brayton cycle working gas during both the sun and shade period of an Earth orbit. During a sun period, a parabolic collector is used to focus solar radiation into the heat receiver through a small aperture located at the collector focal point. The solar input is normally designed to be greater than that required to heat the working gas at the design outlet temperature so that the excess solar energy input during a sun period could be stored in phase change material of heat storage system and then withdrawn by the working gas during the following shade period.

Thermal energy can be stored by two different ways: a) Sensible heat storage system and b) Latent heat storage system. The sensible heat storage

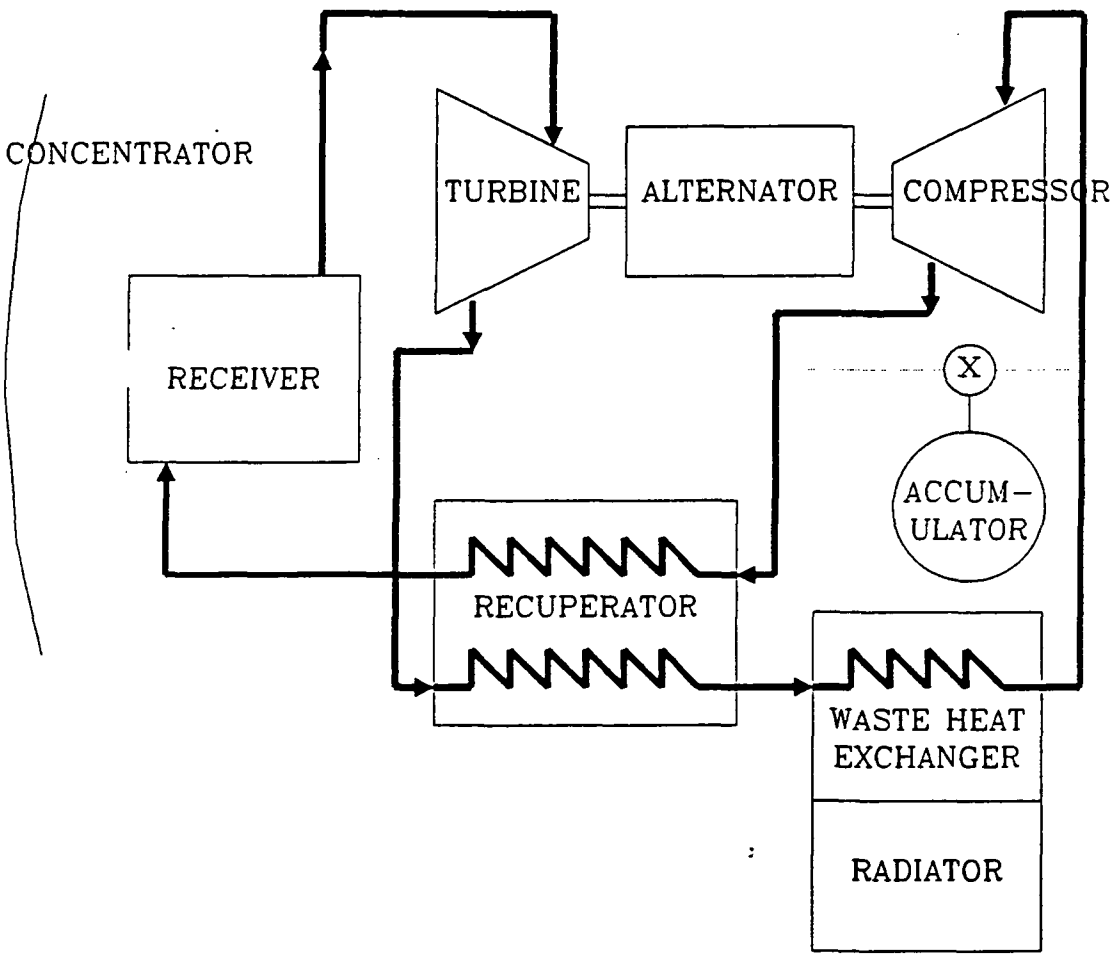

Figure 1.1 Schematic diagram of the closed Brayton cycle solar dynamic power conversion system.

systems utilize the specific heat capacities of liquids such as water or solids such as rocks. On the other hand the latent heat storage systems utilize the latent heat of phase change material(PCM). The energy storage systems using phase change materials are particularly attractive for the following reasons:

(1) Their ability to store or release large amount of thermal energy in the form of latent heat, per unit weight of storage material, resulting in smaller thermal energy storage system weight as compared with sensible heat storage systems;

2. Their ability to store or release thermal energy during phase change at a nearly constant temperature.

1.1.2 *Heat Storage Receiver Energy Balance* In general, the temperature distribution of the heat receiver and of the receiver outlet gas will vary in time depending on the mass flow rate and inlet temperature of the gas, on the solar input rate, on the rate of energy losses through the aperture and through the insulation, on the lengths of the sun and shade periods for one orbit cycle.

If the orbit cycle is such that the excess solar energy input available for storage during a sun period is much in excess of the energy requirements during the following shade period, then all the phase change material would melted and temperature become too high. Accordingly the system will be overheated and burn out. In order to prevent that situation, it is necessary to determine proper values for the aforementioned parameters which brings stable system performance.

A design objective for the solar receiver is to minimize time variations in gas outlet temperature. Therfore, a heat balance must be carefully performed on the total receiver during an orbit. Figure 1.2 shows the different type of energy involved in the solar receiver during the sun and shade period of an orbit. These

energies are:

$\dot{Q}_S$, the rate of solar energy input;

$\dot{Q}_G$, the rate of energy extracted by gas;

$\dot{Q}_L$, the rate of energy loss;

Q_{ST}, the energy stored during a sun period.

An energy balance for these quantities during the sun period provides the energy that should be picked up by the PCM. In turn this energy would be drained from the PCM during the following shade period.

In the general situation each of the above quantities is a function of time. For cyclic equilibrium operation, the energy stored during a sun period equals the energy extracted from the receiver during the following shade period; also equals energy absorbed or released by the PCM, that is,

$$\int_{\Delta t,sun} \left[\dot{Q}_S(t) - \dot{Q}_G(t) - \dot{Q}_L(t)\right] dt = Q_{ST} = \int_{\Delta t,shade} \left[\dot{Q}_G(t) + \dot{Q}_L(t)\right] dt \tag{1.1}$$

The solar energy input term ($\dot{Q}_S$) of Equation 1.1 is a function of the following: 1) receiver and concentrator geometry; 2) receiver and concentrator radiative surface properties; 3) receiver-concentrator orientation with respect to the sun and with respect to each other; 4) solar constant and solar collimation angle.

The heat loss term ($\dot{Q}_L$) in Equation 1.1 consists of loss of radiative energy through the aperture ($\dot{Q}_A$) and energy losses through the insulated surfaces of the receiver ($\dot{Q}_I$); that is,

$$\dot{Q}_L(t) = \int_A \left\{\mathcal{F}_A\left[\sigma T_i(t)^4 - \sigma T_\infty^4\right] + q_{I,i}(t)\right\} dA_i \tag{1.2}$$

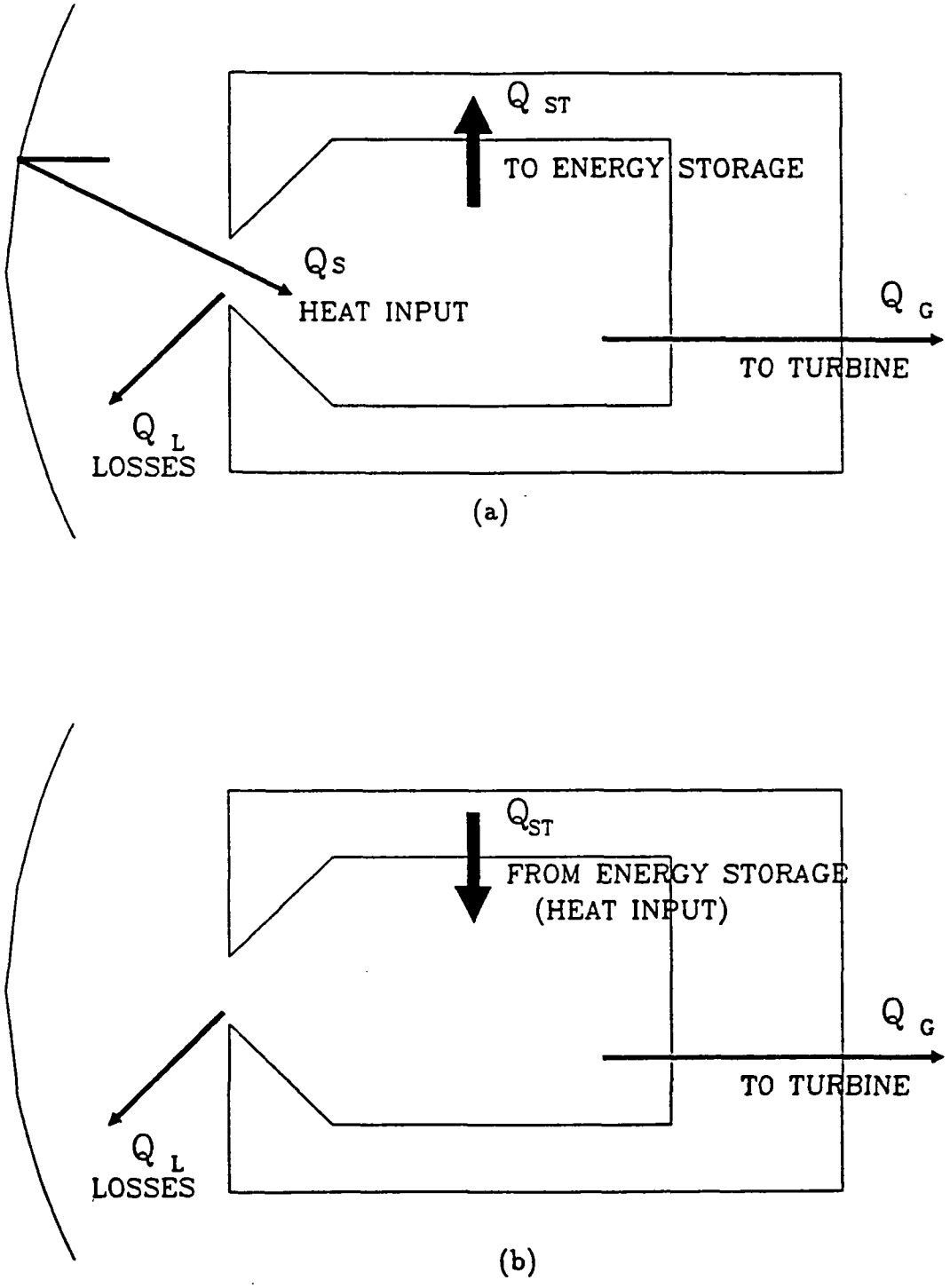

Figure 1.2 Orbital receiver thermal energy balance. (a) During sun period. (b) During shade period.

where the integration is carried out over all of the receiver inside surface and $\mathcal{F}_A$ represents the total radiation view factor from the node i to the aperature. The insulation heat loss (q_I) is dependent on local insulation properties and temperature difference across the insulation. It should be noted that, under 1-g operation for the receiver, natural convection inside the receiver cavitywill contribute to the heat losses, and additional terms should be included in Equation 1.2 as will be shown later.

Finally, the required heat transfer to the working gas ($\dot{Q}_G$) is determined by the Brayton cycle design operating points as follows:

$$\dot{Q}_G(t) = \dot{m}\, Cp_G \left(T_{G_{out}} - T_{G_{in}} \right) \tag{1.3}$$

where $T_{G_{out}}$ and $T_{G_{in}}$ are the specified gas temperatures at exit and inlet to the receiver respectively. On the other hand the heat transfered to the gas can also be expressed as

$$\dot{Q}_G(t) = \sum_{i=1}^{NP} \int_0^L h\, \pi\, D \left[T_w(z) - T_G(z) \right] dz \tag{1.4}$$

where the summation is to include all gas tubes and the integration is carried out along the length of each tube. Equations 1.3 and 1.4 can be used to yield the working fluid tube size and temperature as well as conductance necessary to meet the design requirements of the receiver. In Equation 1.1, one could substitute for $\dot{Q}_L$ and $\dot{Q}_G$ from Equations 1.2 and 1.4 respectively. Thus, the workinf fluid tube wall temperature is directly related to the surface temperature of the receiver cavity, which in turn is dependent on the solar input and the length of the sun and shade period.

Since the PCM is separating the working fluid tube wall and receiver cavity surface, a detailed heat transfer analysis for the PCM should be introduced to ensure a local heat balance at each point within the receiver. Such an analysis will be considered in Chapter IV.

Before getting into the detailed anaysis for the phase change problem and natural convection loss, simplified receiver heat balance should be performed by assuming uniform temperature for the receiver materials to understand a relationship between the different type of energies described above. In order to minimize variation in the receiver and the outlet gas temperatures with time, the independent parameters including geometry should be chosen so as to keep the PCM in the two phase condition. As long as there is the phase change occuring within thermal energy storage container, the exterior surface of the gas tube wall temperature is expected to be near the fusion temperature of the PCM.

In order then to use Equation 1.1 for obtaining a gross estimate of the potential performance, one should assume that the PCM always remains in a two phase condition and that the temperature variations through the PCM can be neglected. This leads to the simplification that the surface temperatures appearing in Equations 1.2 and 1.4 are the melting temperature of the PCM (T_m) which is independent of time. Under these conditions Equation 1.1 can be rewritten as follows:

$$(\dot{Q}_s - \dot{Q}_G - \dot{Q}_L)\Delta t_{sun} = (\dot{Q}_G + \dot{Q}_L)\Delta t_{shade} = Q_{ST} \qquad (1.5)$$

Furthermore if one assume that the gas side conductance used is a mean value, independent of time, the expression for heat transfer to the gas can be written as

$$\dot{Q}_G = \dot{m}\, Cp_G \left[T_w - T_G(0)\right] \left(1 - e^{-BL}\right) \tag{1.6}$$

where

$$B = \frac{NP\,\pi\, D\, h}{W\, C_{p,G}}$$

Since the mass flow rate, inlet and outlet temperatures are specified by the Brayton cycle design points, $\dot{Q}_G$ is also specified from Equation 1.3 and Equation 1.6 yields the required gas side conductance necessary to meet the design requirements when the tube surface temperature is held constant.

The loss term appearing in Equation 1.5 consists of radiative losses through the aperture $\dot{Q}_A$, and of losses through the insulation $\dot{Q}_I$ (Equation 1.2). Using the previously made assumption that the cavity temperature is the same as melting temperature of the PCM, the radiative losses through the aperture can be written as followes:

$$\dot{Q}_A = A_0 \left(\sigma T_m^4 - \sigma T_\infty^4\right) \tag{1.7}$$

With the value of $\dot{Q}_G$ specified by the Brayton cycle requirements and the value of $\dot{Q}_A$ from Equation 1.7, Equation 1.5 can be used to solve either the required minimum solar energy input $\dot{Q}_S$ for a given insulation loss $\dot{Q}_I$, or the maximum allowable insulation loss for a given solar input. Accordingly the energy storage capacity (Q_{ST}), defined as the product of total PCM mass and the heat of fusion of PCM, can be obtained.

The actual sun-shade period encountered during an orbit mainly depend on the orbit altitude and on the angle between the orbit plane and the ecliptic. For a given circular orbit, the maximum shade time occurs when the intersection

of the orbital plane and the ecliptic plane coincides with the Earth-Sun line. Considering circular orbits for a given altitude there is a critical value of orbit inclination above which a satellite would encounter some orbits of continuous sun time during a year. The illumination conditions of several orbits are summarized in Table I. Although the receiver must be designed and insulated to operate under maximum shade conditions, these conditions are encountered only during a small percentage of orbits per year as shown in Table I. Accordingly, during most orbits, the required energy for a shade time is less than the maximum, and it is necessary to develop a method to reject some of the excess solar energy so that the receiver temperatures and the outlet gas temperature are kept at acceptable levels in the sun period.

Recently, computer code has been developed for prediction of the thermal behavior of solar receivers and was given the name HEAP, an acronym for Heat Energy Analysis Program. HEAP has a basic structure that fits any general heat transfer problem with specific features that are "custom-made" for solar receivers. However, this code doesn't include any analysis for a thermal energy storage, and accordingly can not be used to predict the thermal characteristics of the real receiver which has a thermal energy storage unit. Preliminary study has been conducted assuming no property variations between the liquid and solid phases without calculating the location of the liquid-solid interface resulted in a conclusion that more rigorous analysis which allows not only property variations between the liquid and solid phase but also interface motion is needed for the accurate prediction under time dependent environmental boundary condition. Since HEAP program is divided into many subroutines, another subroutine that solves phase change energy storage problem using the method described in chapter II is added into the existing program.

Table I. Orbital Illumination Conditions

Altitude, n mi(km)	Period, min	Maximum shade time, min(% of orbit)	Minimum sun time, min	Critical inclination, deg	Orbit inclination, deg Maximum days/year of continus sun		
					30	60	90
200(370)	91.8	36.2(39.4)	55.6	47.4	0	26	78
300(556)	95.4	35.5(37.2)	59.9	43.4	0	36	95
500(926)	103.2	34.9(33.8)	68.3	37.3	0	52	119
700(1296)	111.6	34.8(31.2)	76.8	32.7	0	76	139
1000(1852)	123.6	34.9(28.2)	88.7	27.3	17	100	160
5000(9260)	324.0	43.3((13.4)	280.7	.6	203	267	268

1.2 Earth-based Receiver Code

Due to time and cost constraints it is likely that most components of the space station solar dynamic power system will undergo extensive earth based testing as opposed to orbital testing. This will expose them to gravity driven effects such as natural convection. This natural convection could influence the heat transfer in the working fluid loops. In most cases the Reynolds number of the flows will be sufficiently large so that the effect will be insignificant. The free convection effects could be expected to be important in two cases [Evans (1987)]. In the receiver. two regimes are considered where natural convection might be important: 1) In the working fluid tube flow, natural convection will be important only if the flow is running at low Reynolds number or undergoing phase change; 2) In the receiver cavity, particularly if the chamber where the receiver is tested is not evacuated (Figure 1.3). Under the current design conditions the working fluid flows are at high Reynolds number and kept in one phase throughout the receiver. Therefore, only natural convection in the receiver cavity will be considered in this analysis.

Preliminary study has been made to examine the effect of free convection on the receiver utilizing an overall convection coefficient for the receiver cavity. One can estimate the size of the convection heat loss rate. While this overall effect was small, there was substantial changes in the wall temperature that might be enough to effect significantly the stresses that are generated in the receiver materials. It should be noted that the above overall convection heat transfer coefficient has been calculated using equations developed for related geometries and not from the test results on actual receivers. Therfore it is necessary that a detailed analysis of the convection inside the receiver be under taken to fully understand the convection effects in receiver performance.

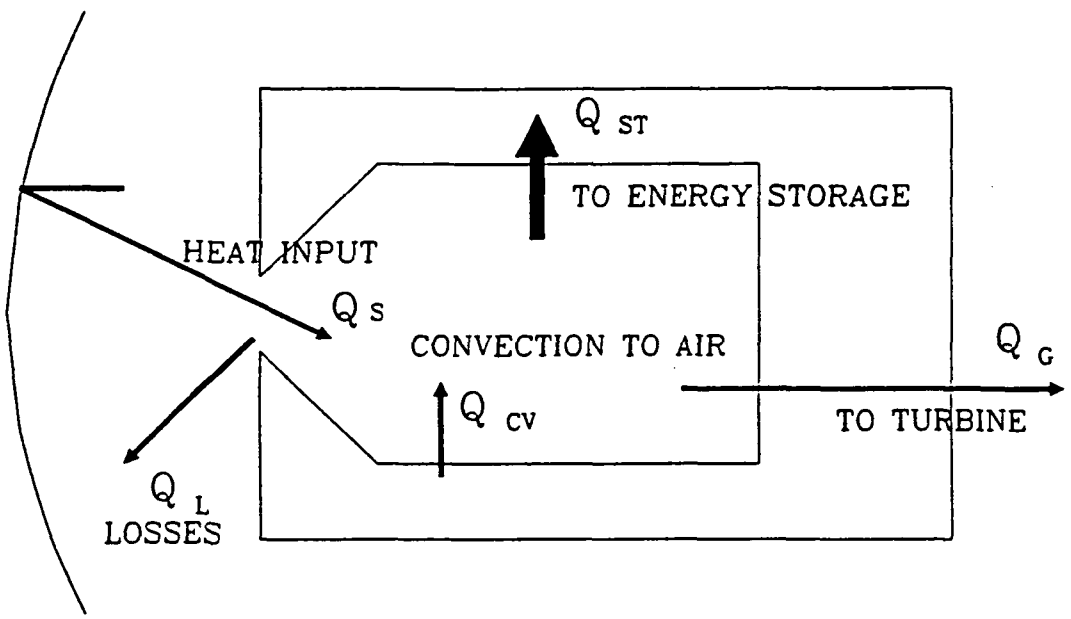

Figure 1.3 Earth-based receiver thermal energy balance.

Hitherto, thermal design of solar receiver in solar dynamic power system for ground test as well as in solar thermal central receiver system is commonly investigated with approximate models where the receiver is treated as an isothermal box with lumped quantities of heat losses by free convection to the surroundings. These approximate models, are not detailed enough to distinguish between receiver designs, to predict transient performance, or to accurately express the performance sensitivity to variations occuring in the system parameters.

For more adequate determination of convection loss, it is necessary to develop a procedure which applies state-of-the-art numerical techniques to analyze the complexities of buoyance-induced flow in cavity-type receiver geometries, and provide finite difference solutions to the equations governing mass, momentum, and energy conservation for the axisymmetrical fluid flow.

1.3 Objective and Scope

The main objective of this thesis is to thermally analyze the performance of the heat receiver under different orbital and terrestrial operating conditions. This objective can be achieved by conducting systematic study on following:

(1) The *phase-change* problem in order to find the temperature distribution and solid-liquid interface motion of the thermal energy storage (TES) material, and heat transfer rates in and out of the material in Chapter II;

(2) The *enclosure natural convection* problem in order to find the temperature and velocity distribution of the fluid inside the enclosure and heat transfer coefficient in Chapter III;

(3) The effect of (1) and (2) on the receiver thermal performances under real environmental conditionsin Chapter IV. And the above analysis will be summarized and resulting conclusions will be drawn in Chapter V.

At this point it is obvious that the natures of these transient problems are such that no known general solutions exist and the problems must be solved by using numerical techniques. In the present thesis, therefore, efficient numerical scheme will be developed and presented with comparison with available data and finally applied to the solar dynamic receiver thermal analysis.

CHAPTER II

HEAT CONDUCTION ANALYSIS OF PHASE CHANGE PROCESS

2.1 Introduction

Heat conduction problems involving freezing or melting are complicated due to the coupling of the temperature field with the rate of propagation of the phase boundary between the solid and liquid phases. The first published discussion of such problems seems to be that by Stefan in a study of the thickness of polar ice [1891], and for this reason the problem of freezing is frequently referred to as the problem of Stefan.

The essential new feature of such problems is the existence of a moving surface of separation between the two phases. Associated with this, the way in which this surface moves has to be determined. Heat is liberated or absorbed on it, and the Thermal properties of the two phases on different sides of it may be different, so that the problem is highly non-linear and special solutions must be determined and cannot be superposed.

In the past, there has been many attempts to obtain solutions to these problems. Only for one dimensional problems, however, fruitful results were obtained. This is due to the complexity of the problem whose solutions have to be obtained simulteneously from the following three non-linear partial differential

equations [Ozisik (1980)]:

$$C_{p_s}\,\rho\,\frac{\partial T_s}{\partial t} = \nabla\cdot\left(k_s\,\nabla T_s\right) \tag{2.1a}$$

$$k_s\,\nabla T_s\cdot\nabla F - k_l\nabla T_l\cdot\nabla F = -\rho\,L\frac{\partial F}{\partial t} \tag{2.1b}$$

$$C_{p_l}\,\rho\,\frac{\partial T_l}{\partial t} = \nabla\cdot\left(k_l\,\nabla T_l\right) \tag{2.1c}$$

where Equation 2.1a and 2.1.c are the conduction heat equations for solid and liquid phases respectively. While Equation 2.1b is the interface condition to be satisfied at the surface of separation.

In most cases idealizations and simplifications have been made to obtain solutions for the above general equations. In Figure 2.1, three-dimensional solidification is illustrated where the solid and liquid phases are separated by a sharp interface defined by the equation

$$F(x,y,z,t) = 0$$

and n denotes the unit vector normal to this interface at any location P on the interface and pointing toward the liquid region.

A survey of the literature shows the major assumptions on which these past solutions are based and indicates the need for future research. Only a few exact analytical solutions have been found and most available solutions are obtained by analytical approximations and numerical methods. The principal approachs to a solution of the solidification processes which have been tried in the past can be divided into two classes:

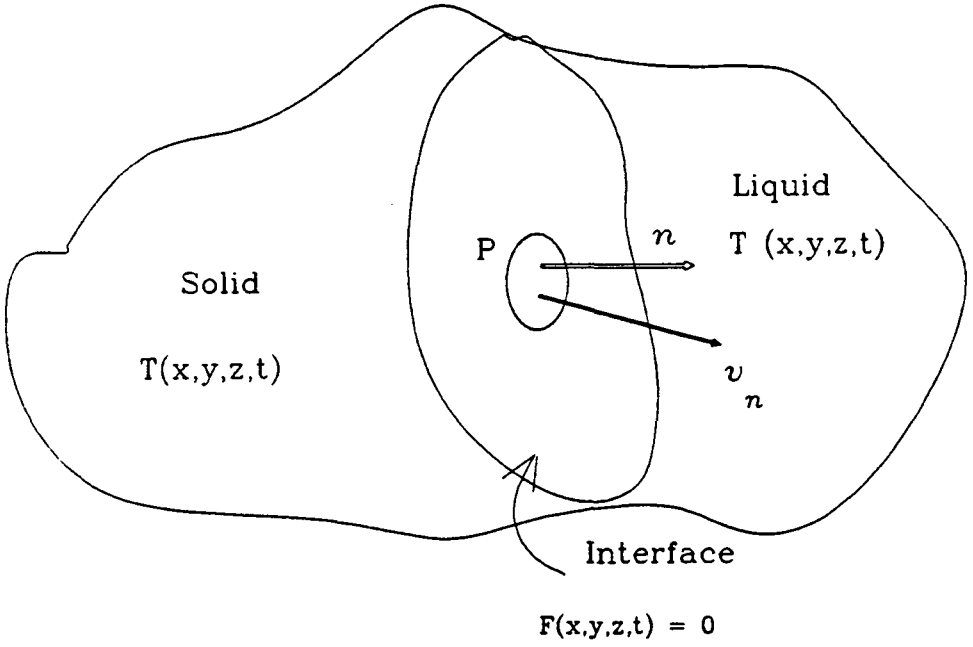

Figure 2.1 Solidification in three dimensions: interface moving in the n direction.

(a) Analytical method

(b) Numerical method

Each of these groups will be discussed separately.

(a) Analytical Methods

For constant material properties and for proper initial and boundary conditions formal analytical solutions can be obtained. In most cases, however, the results are seriously limited, on one hand by the assumptions made, and on the other hand by the difficulties encountered in finding proper solution methods.

The most well-known exact solution is that of Neumann for the semi-infinite region $x > 0$ initially at a constant temperature which is greater than the melting-point, and with the surface $x = 0$ maintained at melting temperature. Exact solutions are also available for a number of problems on the infinite region in which $x < 0$ is initially solid at constant temperature and $x > 0$ is initially liquid at constant temperature.

No exact solutions are available for other geometries such as the slab $-a < x < a$ with its surface maintained at zero, or for the region $-a < x < a$ initially liquid and $|x| > a$ initially solid.

One-dimensional problem for simple shapes has been treated by various analytical techniques, e.g., the perturbation method by Jiji (1970), the heat balance integral method by Goodman (1958), the variational method by Biot (1957), the method of moving heat sources by Lightfoot (1929), and the method of polynomial approximation by Megerlin . Analytical solutions are scarce for problems of more than one dimension.

For problems on radial flow in cylinder or spherical coordinates, the only simple exact solution in cylindrical coordinates corresponds to supply or removal of heat by a continuous line source. An exact solution is given by Ingersoll for

materials extended radially to infinity and cooled by a line source with constant heat flux. For the region bounded internally or externally by a circular cylinder with constant surface temperature, only an approximate solution is available.

London and Seban obtained solutions of quasi-steady temperature distribution to problems involving freezing processes of water. By assuming that the heat capacity of the solidified or melted substance is negligible relative to the latent heat of fusion, they deduced exact closed-form solutions. The equations resulting from this method describe the fusion front motion in bars, cylinders and spheres for different heat transfer coeffcients but are restricted to cases where the materials extend to infinity, where the initial temperatures are at the freezing point. They concluded that an analysis of the degree of approximation introduced by the idealization of negligible capacity effect indicates that the resulting solutions are sufficiently accurate for most engineering calculations and the neglect of ice thermal capacity introduces no greater error than the uncertainty of the correct magnitude of the unit thermal conductivity k. This analysis was further expanded for general orthogonal curvilinear coordinates and validity of neglecting the sensible heat effects for low Stefan numbers was confirmed by Bledjian (1980) who compared his results with Magerlin (1968) and S hamsunder and sparrow (1975).

Most of the analytical investigations presented above neglect latent heat effects and the thermal capacity of the solid and doesn't include finite heat transfer coefficients at the boundaries. Furthermore, no variation with time or temperature is considered in the material properties.

(b) Numerical Methods

Most phase change heat transfer problems, particularly those that are multi-dimensional, have been solved using numerical techniques. Numerical

methods can be divided into two groups, based on the choice of dependent variables used:

1. The temperature is the only dependent variable, and energy conservation equations are written separately in the solid region and in the liquid region.
2. The enthalpy is used as a dependent variable along with the temperature, and energy equation is applied over the whole domain covering both solid liquid phases.

Koeger and Ostrach (1974), Springer and Olson (1963), Gooding and Khader (1976) , and Lajaridis (1970) used the first approach to obtain numerical solutions. The second approach, termed the enthalpy method, was used by Shamsunder and Sparrow (1975), Meyer (1970), Dusinberre (1949), and Griggs et al.

Experimental investigation of phase change problems is important in order to check the validity of various analytic and numerical models. Thus far, however, surprisingly little experimental work has been done and only a limited number of experimental studies are available in the literature. Richter (1978) tested a thermal energy storage material contained in an annulus bounded by a heat pipe. White et al. (1977) performed experiments to observe the melting from an electrically heated cylinder cylinder embedded in a phase change material. Further experimental work was performed by Thomas et al. (1963), Boger et al. (1967), Jiji et al. (1970), and Bailey et al. (1971).

In the present thesis, first method of numerical method was used for cylindrical annulus geometry to determine the temperature distribution and interface location of a PCM using explicit and fully implicit finite-difference scheme. It is the purpose of this chapter not only to calculate temperatures and interface location but also to evaluate the above mentioned numerical schemes in order to

find an efficient finite-different scheme for the phase change problem

2.2 Fomulation of the Problem

In the present investigation, attention is given to the following type of problem: A given material with a distinct fusion temperature is contained between two concentric cylinders. Initially the temperature distribution must be known at all points inside the material. Heat is then transfered in or transfered out of the material, changing its phase from solid to liquid or vice versa. The heat flow in the material is assumed to be such that the fusion front resulting from the phase change move towards the outer or inner radial surfaces. Also the boundary conditions have to be specified in the form of temperature distributions or the heat flow rates along the boundaries of the cylinder and the overall heat transfer coefficients at the boundary surfaces. In general these boundary conditions may depend on time and on the axial, radial and angular coordinates. However, in the present treatment only those processes are independent of the angular coordinates and consequently where the temperature distribution is axially symmetric at all times. Typically in these problems temperature is the basic unknown. Once the temperature distribution is known throughout the material it is relatively easy to determine other principal variables, such as the heat transfer rates and the position of the solid-liquid interface.

The followings are the assumptions which have been made for the present solution method. 1). Phase change meterial(PCM) inside two cylinders is homogeneous. 2). Physical properties of PCM are taken to be uniform in the same phase. 3). PCM inside two cylinders has a distinct fusion temperature. 4). The density of PCM is taken to be same in both solid and liquid phase. 3). The natural convection effects are negligible.

Considering the above assumption, the governing equation for two dimensional axisymmetrical phase change heat-conduction problem is given in the dimensionless form:

$$\frac{\partial \Theta}{\partial \tau} = \gamma \left[\frac{\partial^2 \Theta}{\partial R^2} + \frac{1}{1+R} \frac{\partial \Theta}{\partial R} + \frac{\partial \Theta}{\partial Z^2} \right] \tag{2.2}$$

$$\text{in} \quad R_i < R < E(Z,\tau) \quad \text{or} \quad E(Z,\tau) < R < R_o$$

$$\text{and} \quad Z_f < Z < Z_e$$

$$\text{for} \quad \tau > 0$$

with associated boundary conditions and initial conditions:

1) For $\tau > 0$

$$\begin{cases} \dfrac{\partial \Theta}{\partial R} = f_1(Z,\tau) & \text{or} \\ \Theta_\infty = f_2(Z,\tau) \quad \text{and} \quad H = f_3(Z,\tau) \end{cases} \tag{2.2.a}$$

$$\text{at } R = R_i \text{ or } R = R_o \quad \text{and} \quad Z_f < Z < Z_e$$

and

$$\begin{cases} \dfrac{\partial \Theta}{\partial Z} = g_1(R,\tau) & \text{or} \\ \Theta_\infty = g_2(R,\tau) \quad \text{and} \quad H = g_3(R,\tau) \end{cases} \tag{2.2.b}$$

$$\text{at } Z = Z_f \text{ or } Z = Z_e \quad \text{and} \quad R_i < R < R_o$$

2) For $\tau = 0$

$$\begin{cases} \Theta = f_0(R,Z) & \text{and} \\ E = g_0(R,Z) \end{cases} \tag{2.2.c}$$

$$\text{in } R_i < R < R_o \quad \text{and} \quad Z_f < Z < Z_e$$

and with the solid-liquid interface condition as

$$\begin{cases} \Theta_l = \Theta_s = \Theta_m = 0 & \text{and} \\ \dfrac{\partial E}{\partial \tau} = \left[\dfrac{\partial \Theta_s}{\partial R} - \dfrac{k_l}{k_s}\dfrac{\partial \Theta_l}{\partial R}\right]\left[1 + \left(\dfrac{\partial E}{\partial Z}\right)^2\right] \end{cases} \tag{2.2.d}$$

$$\text{at } R = E(Z,\tau) \qquad \text{for } \tau > 0$$

2.3 Finite-Difference Representation of the Problem

2.3.1 *Finite Differencing of Time Derivatives*

Two different schemes were used to evaluate and compare the results in order to estimate the accuracys and efficiencies (computer storage and CPU time requirements) of each scheme.

(a) Explicit Scheme

To obtain the stable time dependant two dimensional axisymmetrical heat equation, the Fourier stability analysis was performed to yield

$$dt < \frac{8}{\beta} \frac{dR^2\, dZ^2\, (dR^2 + dZ^2)}{16\, dR^4 + 16\, dZ^4 + 32\, dR^2\, dZ^2 + dR^2\, dZ^4} \tag{2.3}$$

The derivation of the Equation 2.3 is given in Appendix A. The above equation is valid for the axisymmetric two dimensional transient heat conduction problem providing periodic boundary conditions are imposed. Since, generally, very small

time step size is required to satisfy the Equation 2.3, prohibitively a large number of time steps are required for the problems that are to be performed over a large period of time. For this reason, an implicit was also investigated to estimate trade offs between the time step size (computer CPU time) and degree of accuracy.

(b) Implicit Scheme

An implicit finite difference scheme is derived for the problem. Unfortunately, the resulting system of linear algebraic equations is no longer tridiagonal and Thomas algorithm can not be applied because of the five unknowns. The system of equations was solved directly using Gauss Jordan method with maximum column pivoting at each time level.

2.3.2 *Finite Differencing of Space Derivatives*

Phase change material of an axisymmetrical geometry is discretized into finite difference grids for numerical calculation as in Figure 2.2. Because of the discontinuity of the temperature distribution across the solid-liquid interface, The computation domain should be subdivided into different regions namely inner region, interface region, and boundary region. The choice of the finite differencing, therfore, has to be different depending upon grid location.

(a) Inner Region

This is the region away from the interface and boundaries, therefore the points used in any one of the following difference formulas are not separated by the interface or the boundary (Figure 2.3). This region also includes the region near the interface and boundary provided that all of the grid points used in any one expression are in the same phase. Two or three-point central difference formula are used which has second-order accuracy:

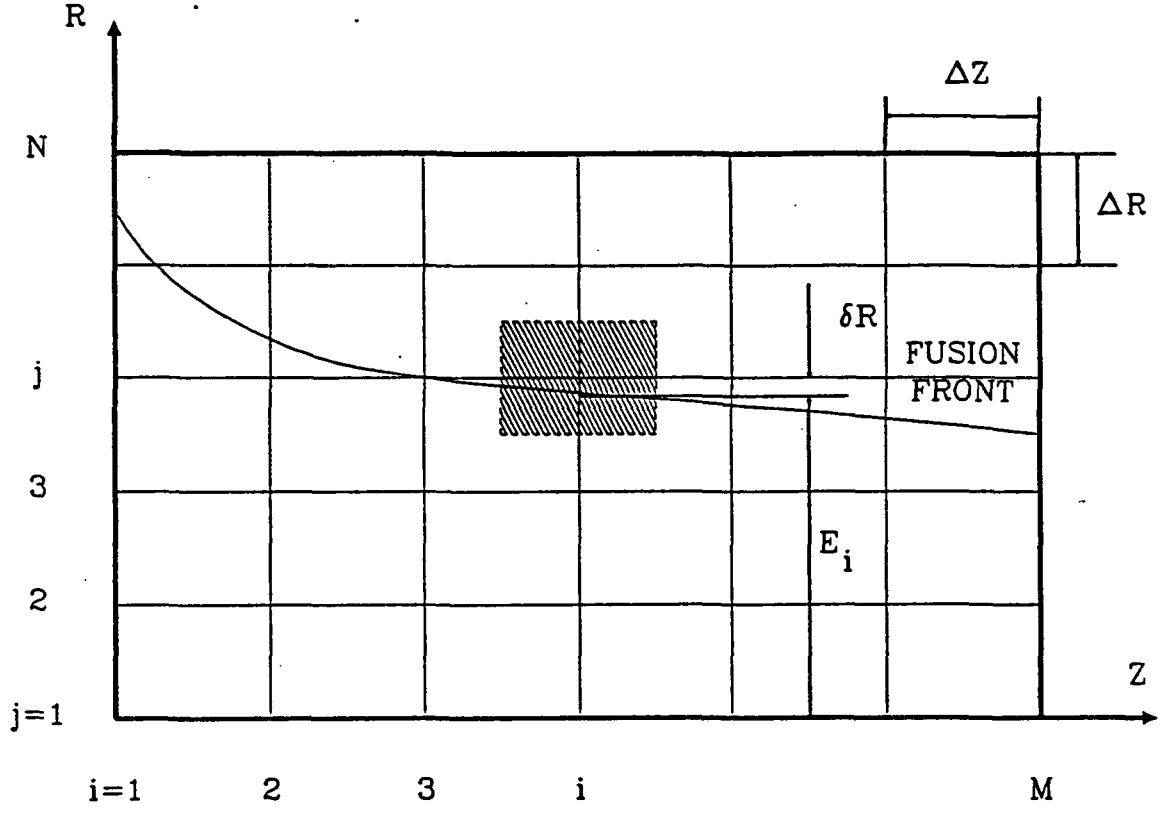

Figure 2.2 Nomenclature and finite difference grid of a axisymmetrical phase change material.

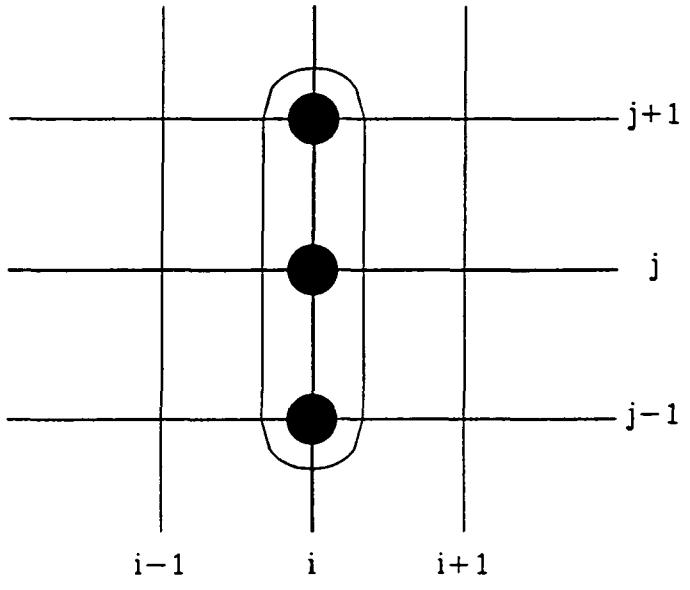

(a)

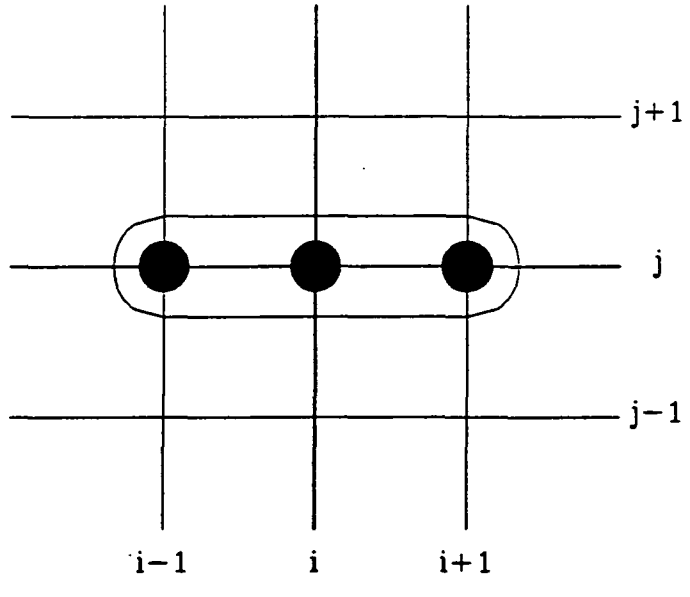

(b)

Figure 2.3 Nodal representation of the finite differencing for inner region. (a) For radial derivatives. (b) For axial derivatives.

$$\frac{\partial \Theta}{\partial R} \cong \frac{\Theta_{i,j+1} - \Theta_{i,j-1}}{2\Delta R} \tag{2.4}$$

$$\frac{\partial^2 \Theta}{\partial R^2} \cong \frac{\Theta_{i,j+1} - 2\Theta_{i,j} + \Theta_{i,j-1}}{(\Delta R)^2} \tag{2.5}$$

$$\frac{\partial^2 \Theta}{\partial Z^2} \cong \frac{\Theta_{i+1,j} - 2\Theta_{i,j} + \Theta_{i-1,j}}{(\Delta Z)^2} \tag{2.6}$$

(b) Interface Region

This region is defined for those three grid points in either radial or axial direction: one containing the interface (interface node) and the other two points (semi-interface node) directly adjacent to it (Figure 2.4). For these points, previous three-point central formulas can not be used because of the discontinuity of the temperature at the interface.

Either three-point forward differencing or backward differencing has been used for the grid points containing the interface according to the phase of the points relative to the interface.

The backward difference formula is used when the point lies between the interface and the inner radius:

$$\frac{\partial \Theta}{\partial R} \cong \frac{1}{\Delta R}\left[\frac{3}{2}\Theta_{i,j} - 2\Theta_{i,j-1} + \frac{1}{2}\Theta_{i,j-2}\right] \tag{2.7}$$

$$\frac{\partial^2 \Theta}{\partial R^2} \cong \frac{2}{(\Delta R)^2}\left[\frac{1}{2}\Theta_{i,j} - \Theta_{i,j-1} + \frac{1}{2}\Theta_{i,j-2}\right] \tag{2.8}$$

and the forward differencing is used when the point lies between the outer radius and the interface:

$$\frac{\partial \Theta}{\partial R} \cong \frac{1}{\Delta R}\left[-\frac{3}{2}\Theta_{i,j} + 2\Theta_{i,j+1} - \frac{1}{2}\Theta_{i,j+2}\right] \tag{2.9}$$

$$\frac{\partial^2 \Theta}{\partial R^2} \cong \frac{2}{(\Delta R)^2}\left[\frac{1}{2}\Theta_{i,j} - \Theta_{i,j+1} + \frac{1}{2}\Theta_{i,j+2}\right] \tag{2.10}$$

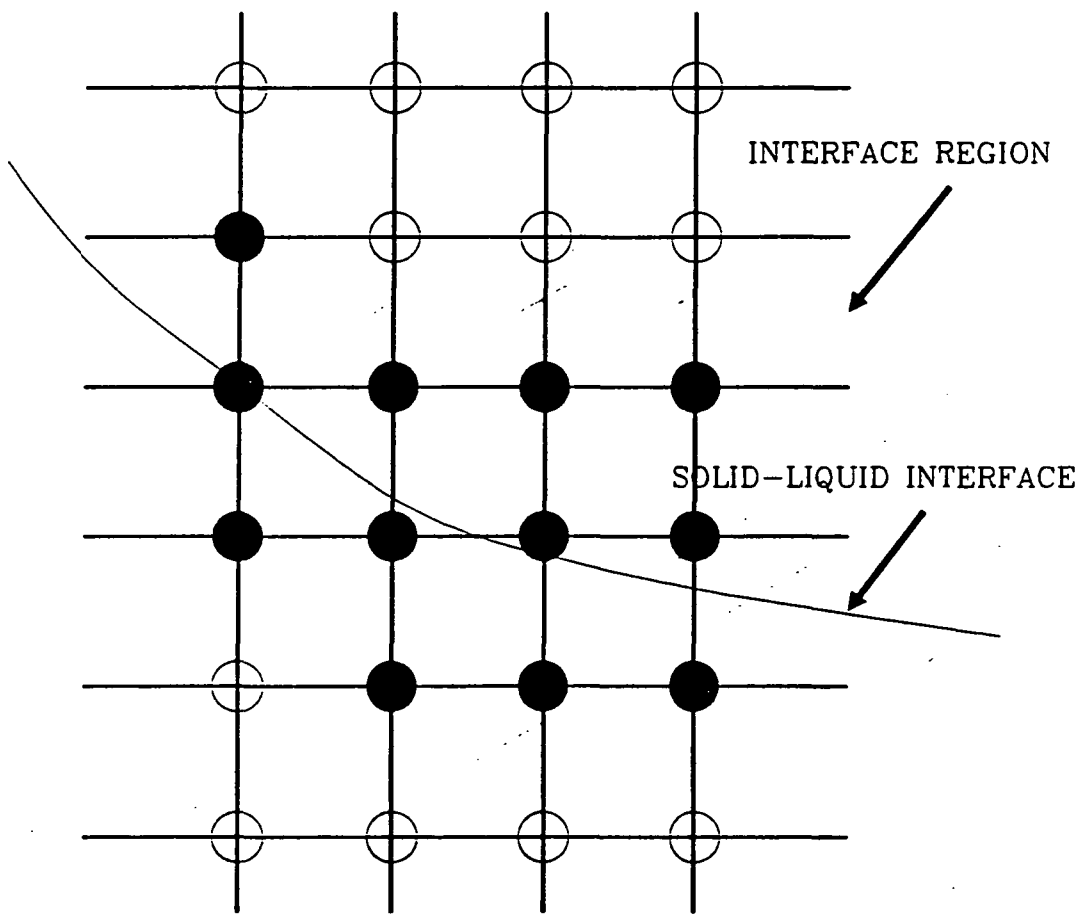

Figure 2.4 Nodal definition of the interface region.

In Equations 2.7 to 2.10 for the interface grid point used by Springer and Olson (1962), temperature of the interface was not included which also means the first interface boundary condition of Equation 2.2.d was not utilized. Since present author experienced that using Equations 2.7 to 2.10 resulted in numerical instabilities in temperatures near the interface, modification has been made to remedy that defect. Instead of using three point differencing which excludes the interface temperature, two-point (linear) interpolation between the interface and the node of same phase adjacent to the interface node is applied as follows (Figure 2.5).

$$\frac{\partial \Theta}{\partial R} \cong -\frac{\Theta_{i,j}}{\Delta R + \delta R} \tag{2.11}$$

$$\frac{\partial^2 \Theta}{\partial R^2} \cong 0 \tag{2.12}$$

Also, for the interface node points near the boundary where the point lies between the interface line and the boundary point (Figure 2.6), the same two-point (linear) interpolation can be used by replacing $\Delta R + \delta R$ with ΔE_j.

$$\frac{\partial \Theta}{\partial R} \cong -\frac{\Theta_{i,j}}{\Delta E_j} \tag{2.13}$$

$$\frac{\partial^2 \Theta}{\partial R^2} \cong 0 \tag{2.14}$$

where ΔE_j is the radial distance between the interface and either inner or outer boundary.

For the grid points directly adjacent to the interface points, three-point unequal-spacing centered difference formulas are used (Figure 2.7). The difference formula is written as

$$\frac{\partial \Theta}{\partial R} \cong \frac{1}{\Delta R}\left[\Theta_{i,j}\left(\frac{r^*}{1+r^*}\right) - \Theta_{i,j-1}\left(\frac{1+r^*}{2+r^*}\right)\right] \tag{2.15}$$

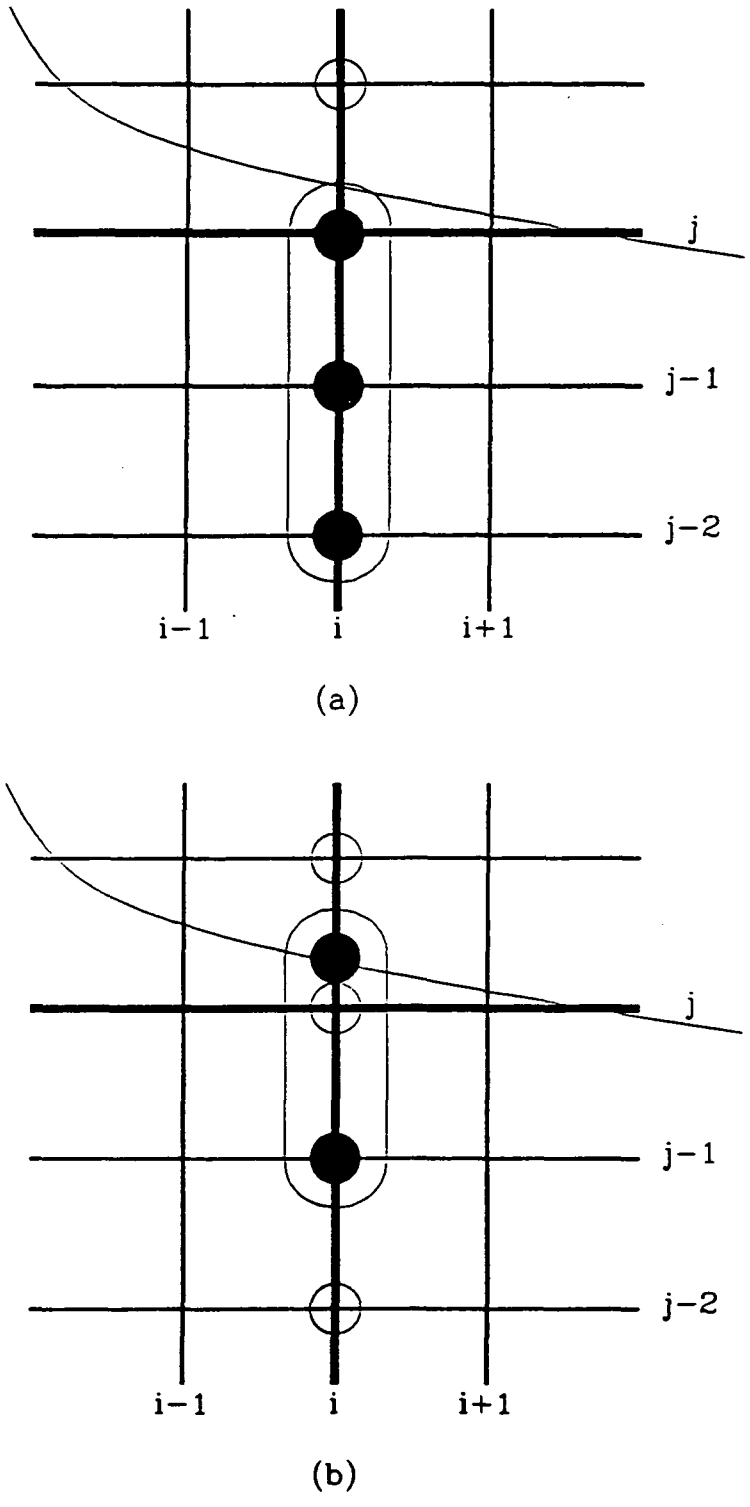

Figure 2.5 Modification of nodal representation of the finite differencing for the interface node. (a) Approach by Springer and Olson. (b) Present approach.

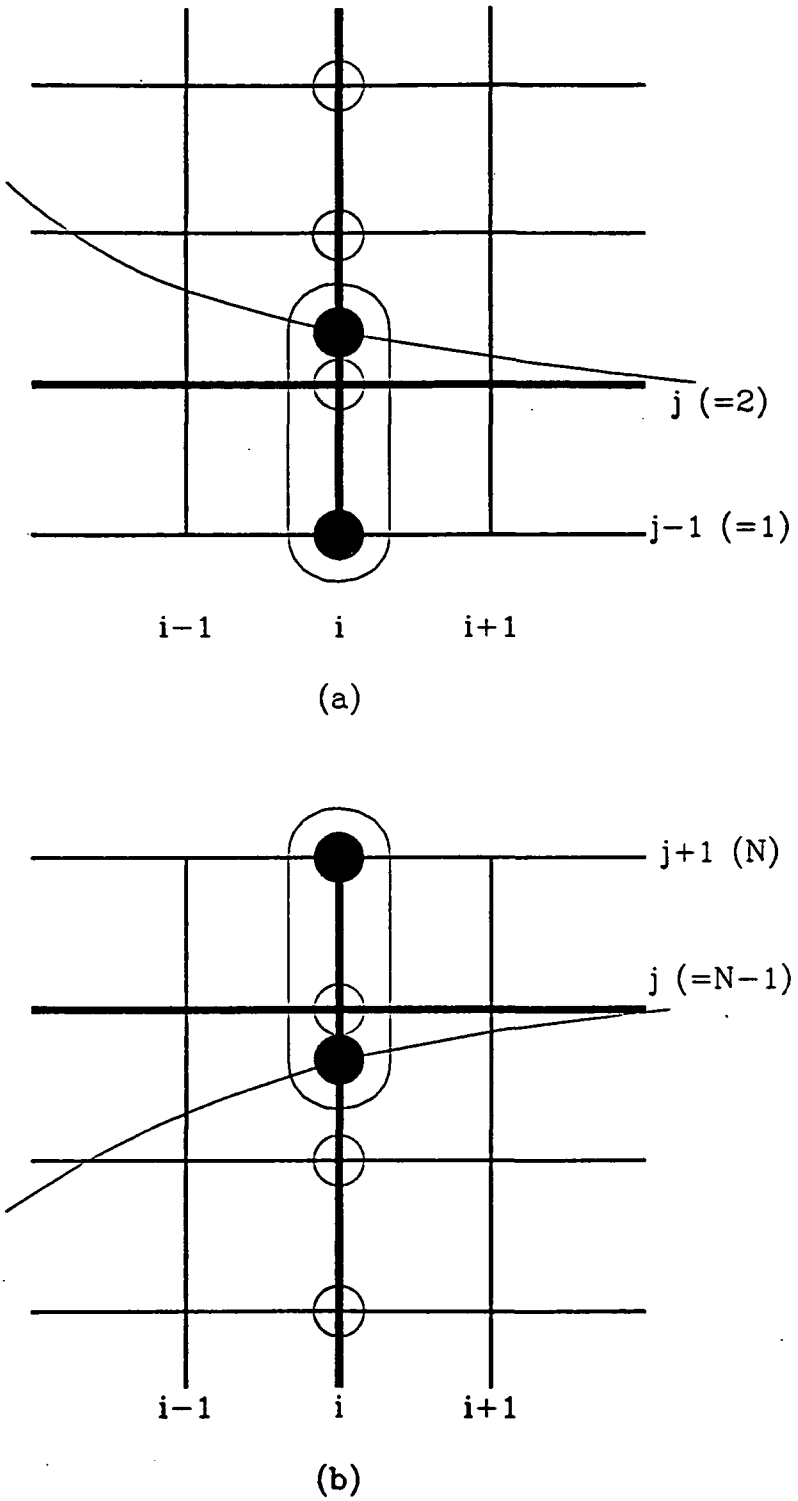

Figure 2.6 Nodal representation of the finite differencing for the interface node near the boundaries. (a) Near the inner radial boundary. (b) Near the outer radial boundary.

$$\frac{\partial^2 \Theta}{\partial R^2} \cong \frac{2}{(\Delta R)^2}\left[\frac{\Theta_{i,j-1}}{2+r^*} - \frac{\Theta_{i,j}}{1+r^*}\right] \tag{2.16}$$

for the point lies between the interface and the inner radius (Figure 2.7.a). And another formula is written as

$$\frac{\partial \Theta}{\partial R} \cong -\frac{1}{\Delta R}\left[\Theta_{i,j}\left(\frac{-r^*}{1-r^*}\right) + \Theta_{i,j+1}\left(\frac{1-r^*}{2-r^*}\right)\right] \tag{2.17}$$

$$\frac{\partial^2 \Theta}{\partial R^2} \cong \frac{2}{(\Delta R)^2}\left[\frac{\Theta_{i,j-1}}{2-r^*} - \frac{\Theta_{i,j}}{1-r^*}\right] \tag{2.18}$$

for the point lies between the interface and the outer radius (Figure 2.7.b).

To find the axial derivatives in this region, central difference formula, Equation 2.6 is used for point when the two axially neighboring points to the left and right of it, are in the same phase. If the points are in different phases, the same linear interpolation of Equation 2.33 is used as the radial case.

(c) Boundary Region

This region contains the points on the boundaries (Figure 2.8). Therefore, the boundary points can be eliminated from the calculation matrix for the problems with boundary conditions of the first kind (boundary temperatures are prescribed). For the boundary conditions of the second kind (heat fluxes are prescribed) and the third kind (ambient temperatures are specified), the temperature derivatives normal to the boundarys have to be expressed in terms of the boundary conditions.

The first and second derivatives in R direction at the inner and outer radial boundaries are given as

$$\frac{\partial \Theta}{\partial R} \cong -Q^*_{i,j}\frac{r_{in}}{r_{i,j}}\frac{k_f}{k} \tag{2.19}$$

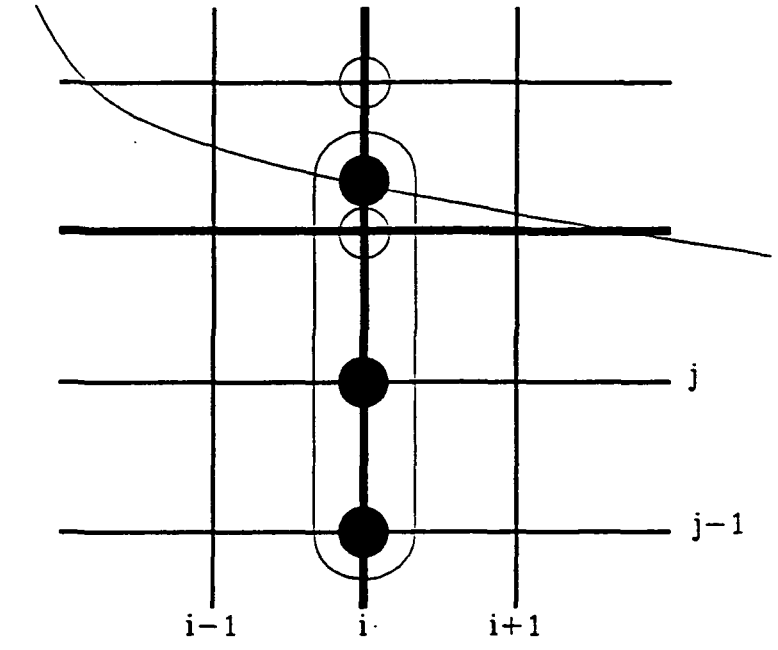

(a)

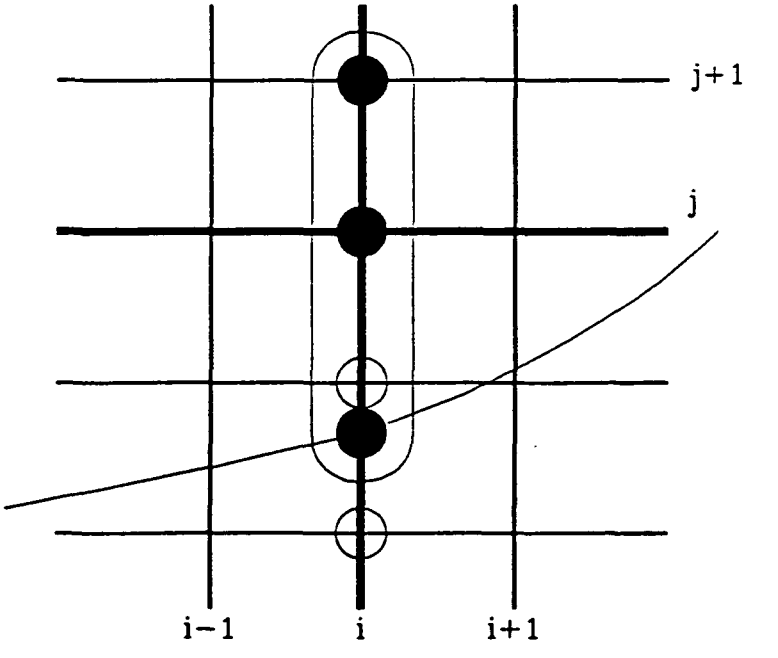

(b)

Figure 2.7 Nodal representation of the finite differencing for the semi-interface nodes. (a) Point lies inner radius side. (b) Point lies outer radius side.

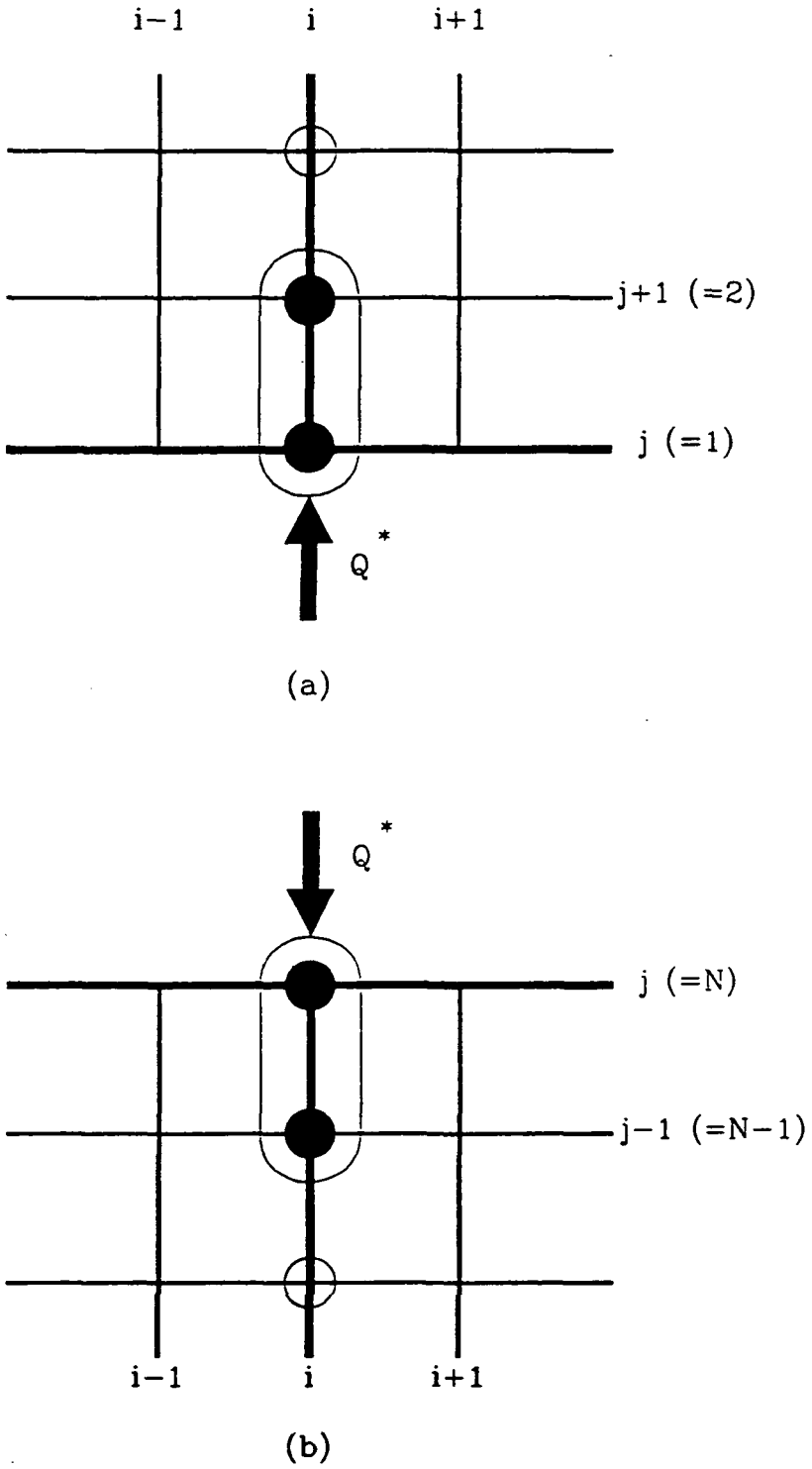

Figure 2.8 Nodal representation of the finite differencing for boundary region. (a) For radial derivatives. (b) For axial derivatives.

$$\frac{\partial^2 \Theta}{\partial R^2} \cong \frac{2}{\Delta R}\left[\frac{\Theta_{i,j\pm1} - \Theta_{i,j}}{\Delta R} + Q^*_{i,j}\frac{r_{in}}{r_{i,j}}\frac{k_f}{k}\right] \tag{2.20}$$

where Q^* is the dimentionless heat transfer defined as

$$Q^*_{i,j}(\tau) = \frac{Q_{i,j}(t)}{2\pi\, k_f\, \Delta z\, T_f} \tag{2.21}$$

If the interface separates the boundary point from the adjoining one, Equation 2.20 can not be applied, in which case the first term on the right-hand side of the equation has to be modified. At the inner and outer radial boundaries the second derivatives with respect to R are

$$\frac{\partial^2 \Theta}{\partial R^2} \cong \frac{2}{\Delta E_j}\left[-\frac{\Theta_{i,j}}{\Delta E_j} + Q^*_{i,j}\frac{r_{in}}{r_{i,j}}\frac{k_f}{k}\right] \tag{2.22}$$

Where ΔE_j is the radial distance between the interface and, the inner ($j = 1$) or radial ($j = N$) boundary

It should be noted that Equation 2.22 goes to infinity as the interface appoaches the inner or outer boundary. Therefore, their computation has to be started with the interface already advances enough distance from the boundary to avoid this possibility.

Similar equations are also used to calculate the first and second derivatives in the axial direction at the front and the end surfaces of the cylinder:

$$\frac{\partial \Theta}{\partial R} \cong -Q^*_{i,j}\frac{r_{in}}{r_{i,j}}\frac{k_f}{k}\frac{\Delta Z}{\Delta R} \tag{2.23}$$

$$\frac{\partial^2 \Theta}{\partial R^2} \cong \frac{2}{\Delta R}\left[\frac{\Theta_{i,j\pm1} - \Theta_{i,j}}{\Delta R} + Q^*_{i,j}\frac{r_{in}}{r_{i,j}}\frac{k_f}{k}\frac{\Delta Z}{\Delta R}\right] \tag{2.24}$$

and

$$\frac{\partial^2 \Theta}{\partial R^2} \cong \frac{2}{\Delta E_j} \left[-\frac{\Theta_{i,j}}{\Delta E_j} + Q^*_{i,j} \frac{r_{in}}{r_{i,j}} \frac{k_f}{k} \frac{\Delta Z}{\Delta R} \right] \tag{2.25}$$

for the situation when the interface separates the front or end boundary from the adjacent point.

To use the same temperature derivatives written in terms of the heat-flow rate Q^* for the convection boundary condition, Q^* is determined from the following relationship:

$$Q^*_{i,j} = U^*_{i,j} \frac{\Delta S}{\Delta Z} \frac{R_{i,j}}{r_{in}} \left(\Theta_{\infty\, i,j} - \Theta_{i,j} \right) \tag{2.26}$$

where the dimensionless overall heat transfer coefficient U^* is given by

$$U^*_{i,j} = \frac{U_{i,j}\, r_{in}}{k_f} \tag{2.27}$$

(d) Interface Motion

So far, The derivatives of the temperatures at the node point has been derived to transform the governing equation (Equation 2.2) into difference form. To transform The heat-balance equation (Equation 2.2.d), temperature derivatives at the interface have to be determined. At the interface, forward and backward interpolation give

$$\frac{\partial \Theta}{\partial R} \cong \frac{1}{\Delta R} \left[\Theta_{i,j-2} \left(\frac{1+r^*}{2+r^*} \right) - \Theta_{i,j-1} \left(\frac{2+r^*}{1+r^*} \right) \right] \Bigg|_{R=E} \tag{2.28}$$

and

$$\frac{\partial \Theta}{\partial R} \cong \frac{1}{\Delta R} \left[\Theta_{i,j+1} \left(\frac{2-r^*}{1-r^*} \right) - \Theta_{i,j+2} \left(\frac{1-r^*}{2-r^*} \right) \right] \Bigg|_{R=E} \tag{2.29}$$

Near the inner or outer radial boundary where only one node-temperature is available in any one phase-side (Figure 2.5), the above two equations are to be replaced by Equations 2.31 and 2.32.

At the interior mesh point the slope of the interface in Equation 2.9 is determined by the centered three-point interpolation

$$\frac{\partial E}{\partial Z} \cong \frac{E_{i+1} - E_{i-1}}{2\Delta Z} \tag{2.30}$$

At those boundaries where $i = 1$ and $i = M$ the expression for the slope is

$$\frac{\partial E}{\partial Z} \cong \frac{\pm E_{i+1} \mp E_i}{\Delta Z} \tag{2.31}$$

2.4 Results and Discussion

Since there is no analytical solution in two dimensional phase-change problem available, the present general method is applied to one dimensional problem and the results are compared with approximate analytic solutions. Also a parametric investigation was performed by using different number of radial nodes and/or numerical scheme in order to examine grid-dependency of the solution and trade-off between cpu time of the computer and solution accuracy.

Table II shows results of the explicit scheme for the ice formation problem of London and Seban. Tabulated values are the elapsed time for solid/liquid interface to reach the specified radial positions, namely, R=1.0, 1.25, 1.5, and 1.75 for the different number of nodes used (Table IIa). Also required CPU time for the solid/liquid interface to reach the outer boundary, r_o is tabulated in Table IIb. Figure 2.9 shows the water/ice interface location in freezing water obtained from explicit scheme with 4 radial nodes (solid line). The interface

location was calculated from the solutions given by London and Seban and was also plotted in Figure 2.9 (symbols). Similarly, the water/ice interface locations obtained from the explicit scheme with 6, 9, 12, 15 and 18 nodes are plotted in figures 2.10 to 2.14 along with analytic solution.

From Table II and Figures 2.9 to 2.14, the numerical results with more than 9 radial nodes are shown to be in good agreement with the analytical results of London and Seban. The result with 18 radial nodes (Figure 2.14) is not deviated far away from the result with 9 radial nodes (Figure 2.11) in Table IIa, while required CPU time using 18 nodes are about 8 times larger than the CPU time using 9 nodes.

Table III shows the results of the implicit scheme for the same problem discussed above for which the previous explicit scheme has been tested. In this table, the same parameters are tabulated as in Table II using the implicit scheme. Figure 2.15 shows the water/ice interface location in freezing water obtained from implicit scheme with 4 radial nodes (solid line). The interface location was also plotted from the solutions given by London and Seban (symbols). Again, the water/ice interface locations obtained from the implicit scheme with 6, 9, 12, 15 and 18 nodes are plotted in figures 2.16 to 2.20 along with analytic solution.

From Table III and Figures 2.15 to 2.20, it is observed that the implicit scheme is somewhat dissipative as the solid/liquid interface advances to outer radius for the results with 9 nodes or more. The above diviation can be attributed to the growing round off error as the number of the nodes increased due to a large number of dependent arithmatic operations. Since two dimentional nature of this scheme, the efficiency of the tridiagonal algorithm has been lost and the resulting system of algebraic equation had to be solved at each time step, one can see, in Table IIIb, considerablly larger CPU time has been required to complete the calculation. Figure 2.16 shows the result with 6 radial nodes

Table II. Comparison of explicit scheme results with analytical solution

(a) Calculated time for interface to reach the specified positions

Dimensionless interface position	1.0	1.25	1.5	1.75
Analytical	0.636	1.037	1.551	2.184
Explicit 4 nodes	0.501	0.932	1.534	2.472
6 nodes	0.668	1.084	1.630	2.293
9 nodes	0.658	1.074	1.604	2.257
12 nodes	0.657	1.069	1.598	2.249
15 nodes	0.655	1.068	1.596	2.246
18 nodes	0.655	1.067	1.595	2.245

(b) Elapsed CPU time

Explicit scheme	4 nodes	6 nodes	9 nodes	12 nodes	15 nodes	18 nodes
Elapsed CPU time, sec	0.33	1.35	4.07	9.73	19.35	33.7

is in good agreement with analytic result, however, since the results for other nodes show that the implicit scheme is in error, choice of using 6 node implicit scheme was not made due to uncertainty for other applications. Now comparing the results obtained using the two numerical schemes, explicit and implicit, the explicit scheme with 9 radial nodes has been selected to be used in analizing the behavior of the phase change material of the thermal energy storage system of the receiver. The results of TES analysis will be presented in Chapter IV and comparison has been also made with the case without phase change energy storage system.

Table III. Comparison of implicit scheme results with analytical solution

(a) Required time for interface to reach the specified positions

Dimensionless interface position	1.0	1.25	1.5	1.75
Analytical	0.636	1.037	1.551	2.184
Implicit 4 nodes	0.501	0.908	1.510	2.412
6 nodes	0.661	1.052	1.554	2.144
9 nodes	0.633	1.009	1.474	2.029
12 nodes	0.622	0.987	1.441	1.985
15 nodes	0.612	0.973	1.422	1.959
18 nodes	0.607	0.965	1.410	1.943

(b) Elapsed CPU time

Implicit scheme	4 nodes	6 nodes	9 nodes	12 nodes	15 nodes	18 nodes
Elapsed CPU time, sec	0.5	2.68	19.13	78.46	234.52	577.95

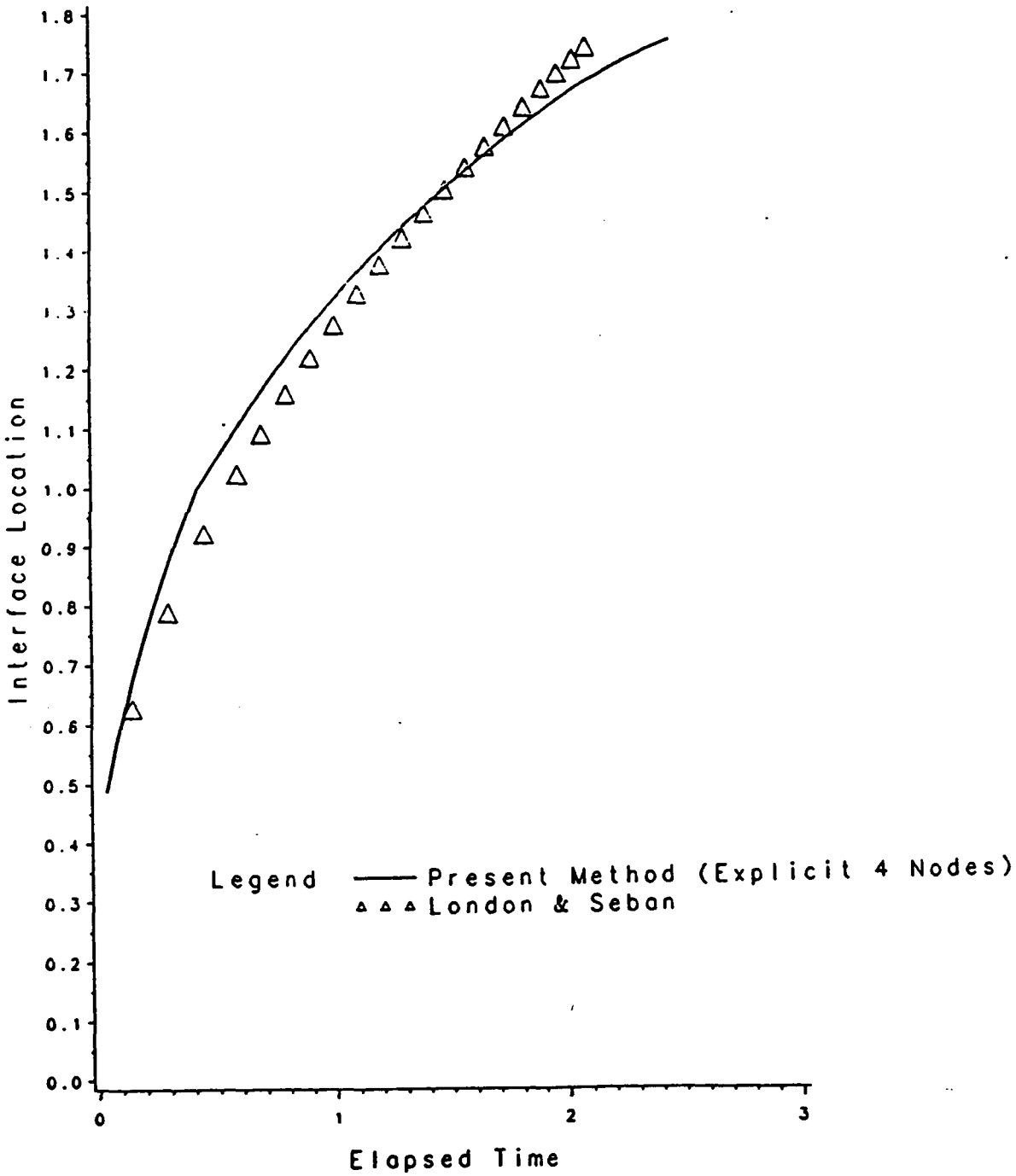

Figure 2.9 Comparison of the interface location with the analytic result subject to constant temperature: explicit scheme with 4 radial nodes.

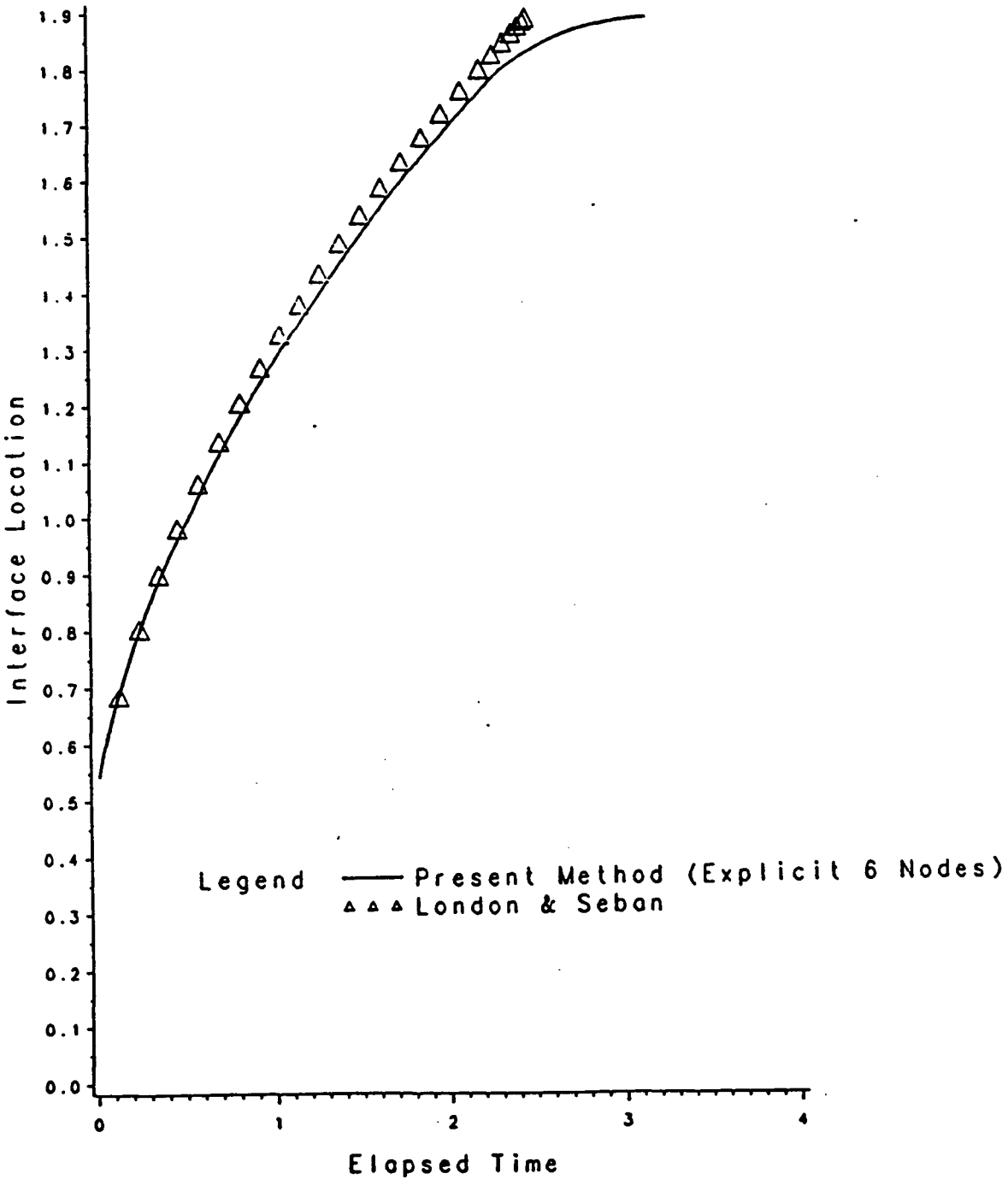

Figure 2.10 Comparison of the interface location with the analytic result subject to constant temperature: explicit scheme with 6 radial nodes.

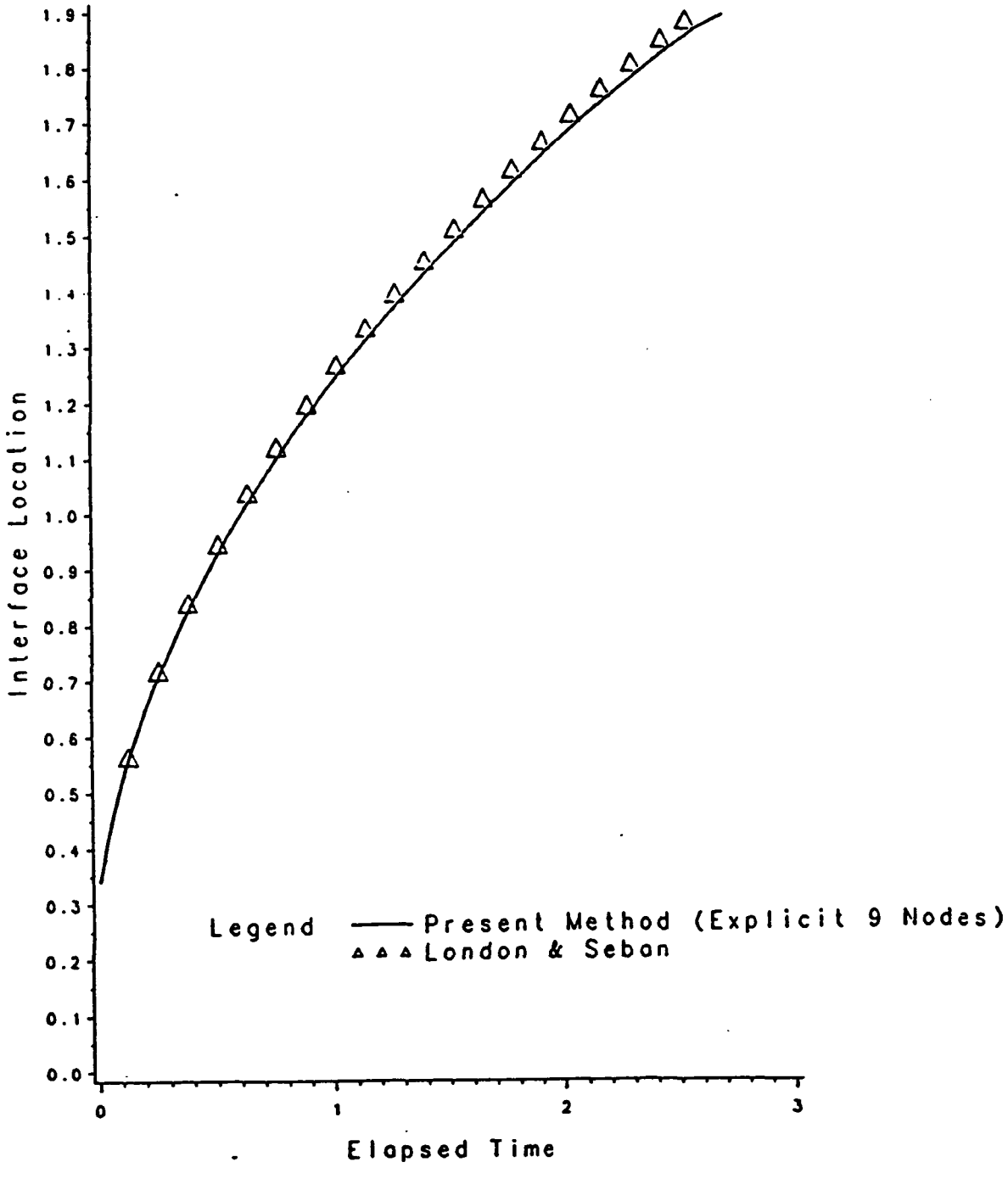

Figure 2.11 *Comparison of the interface location with the analytic result subject to constant temperature: explicit scheme with 9 radial nodes.*

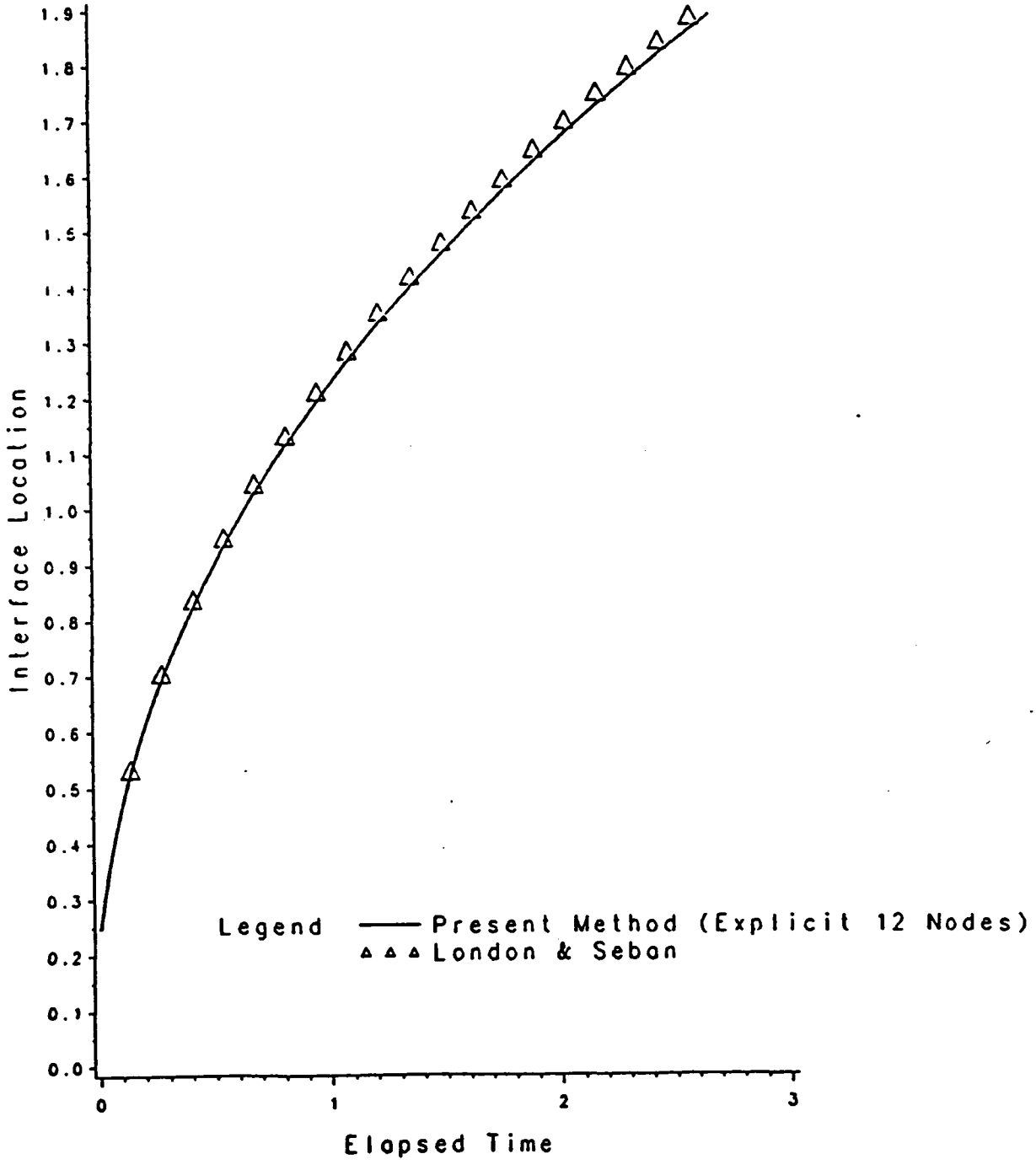

Figure 2.12 Comparison of the interface location with the analytic result subject to constant temperature: explicit scheme with 12 radial nodes.

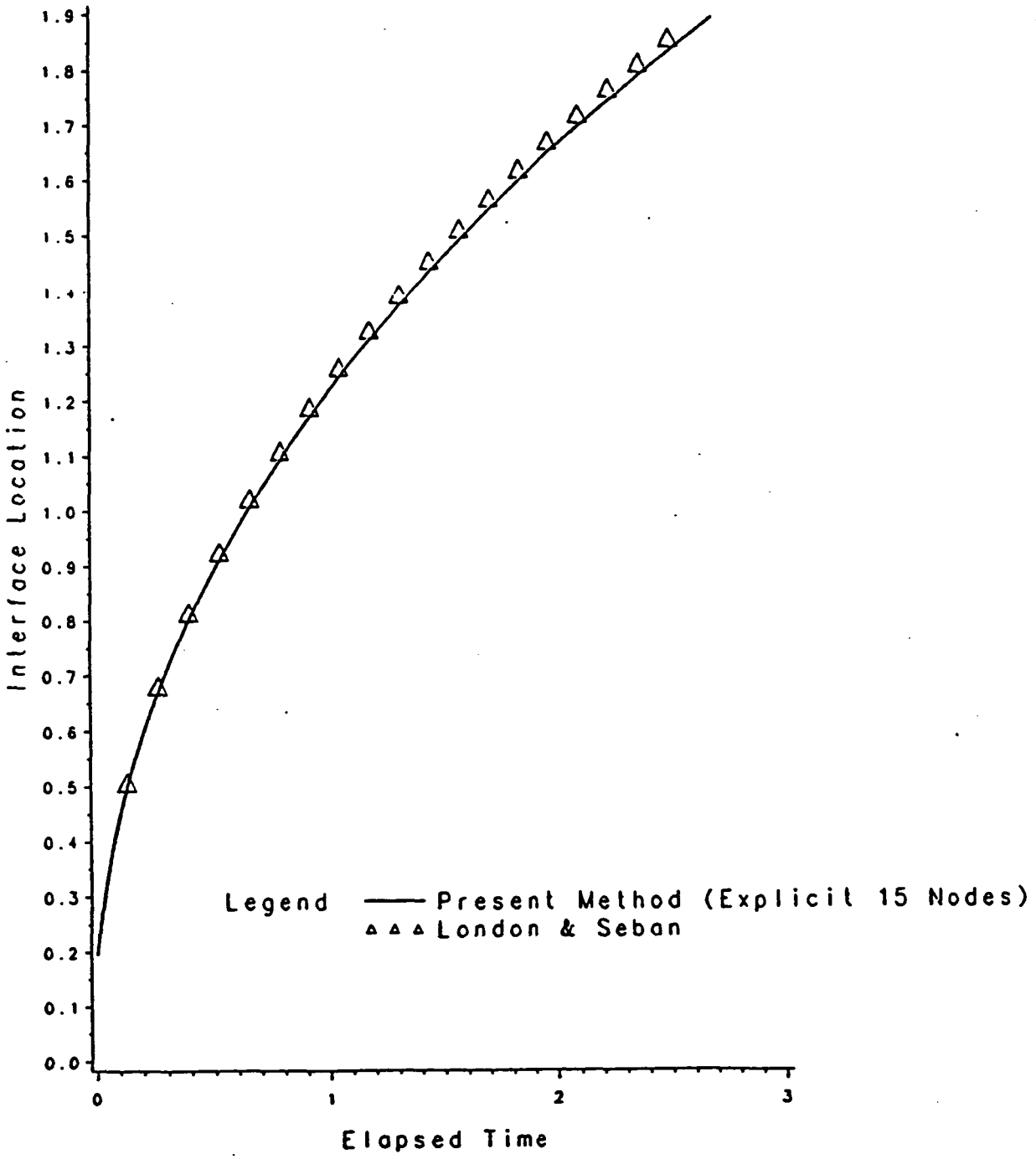

Figure 2.13 Comparison of the interface location with the analytic result subject to constant temperature: explicit scheme with 15 radial nodes.

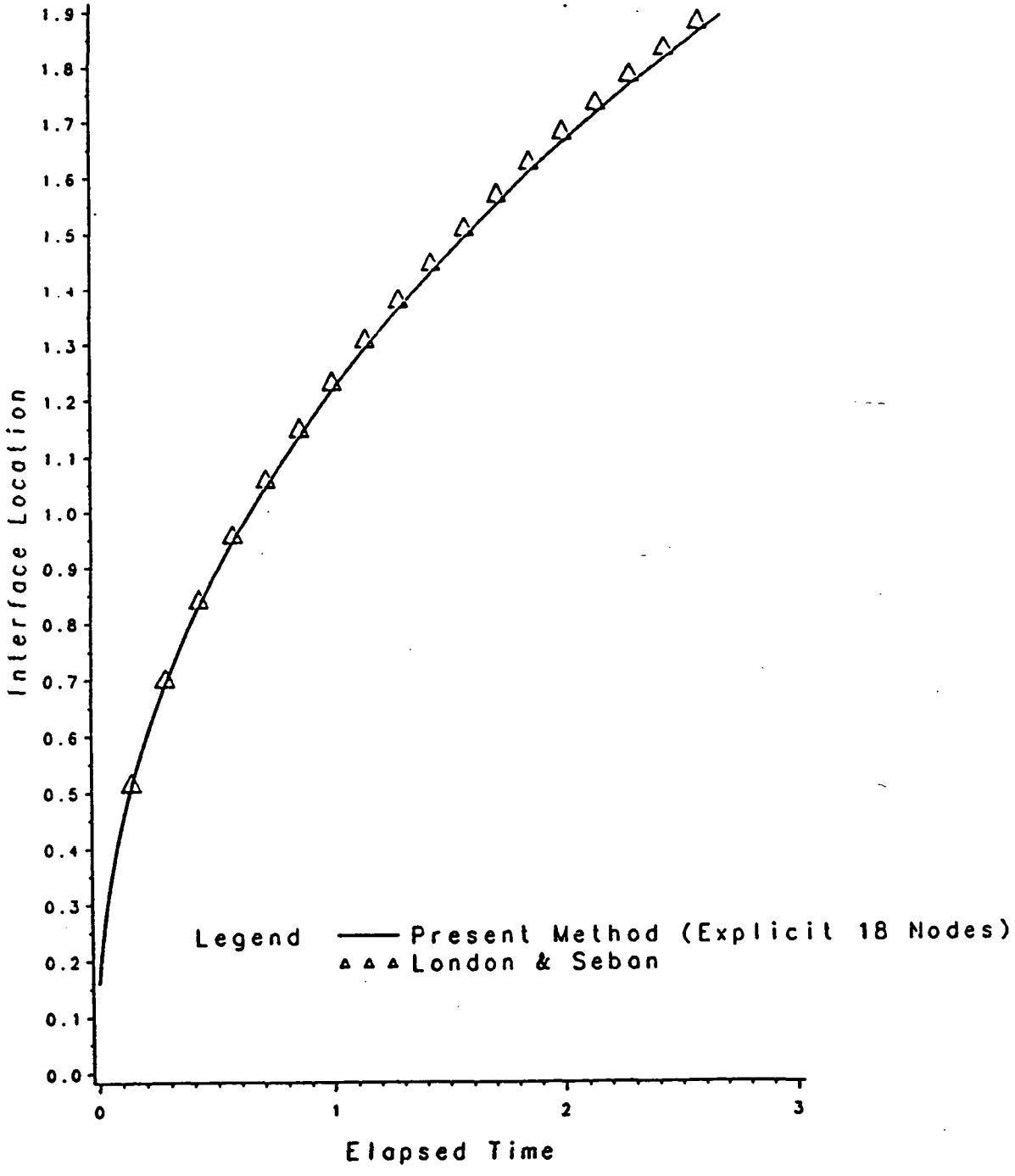

Figure 2.14 Comparison of the interface location with the analytic result subject to constant temperature: explicit scheme with 18 radial nodes.

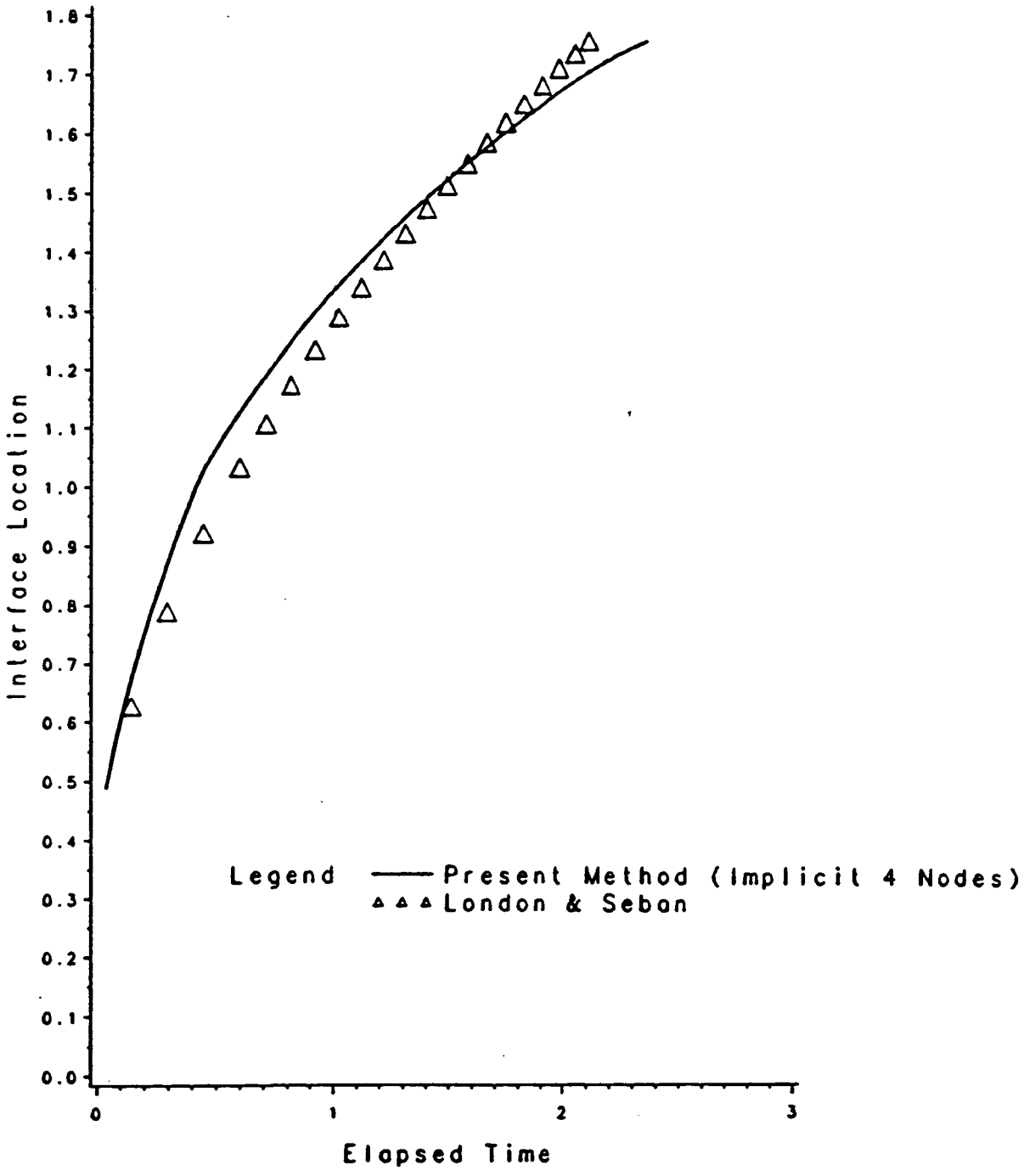

Figure 2.15 Comparison of the interface location with the analytic result subject to constant temperature: implicit scheme with 4 radial nodes.

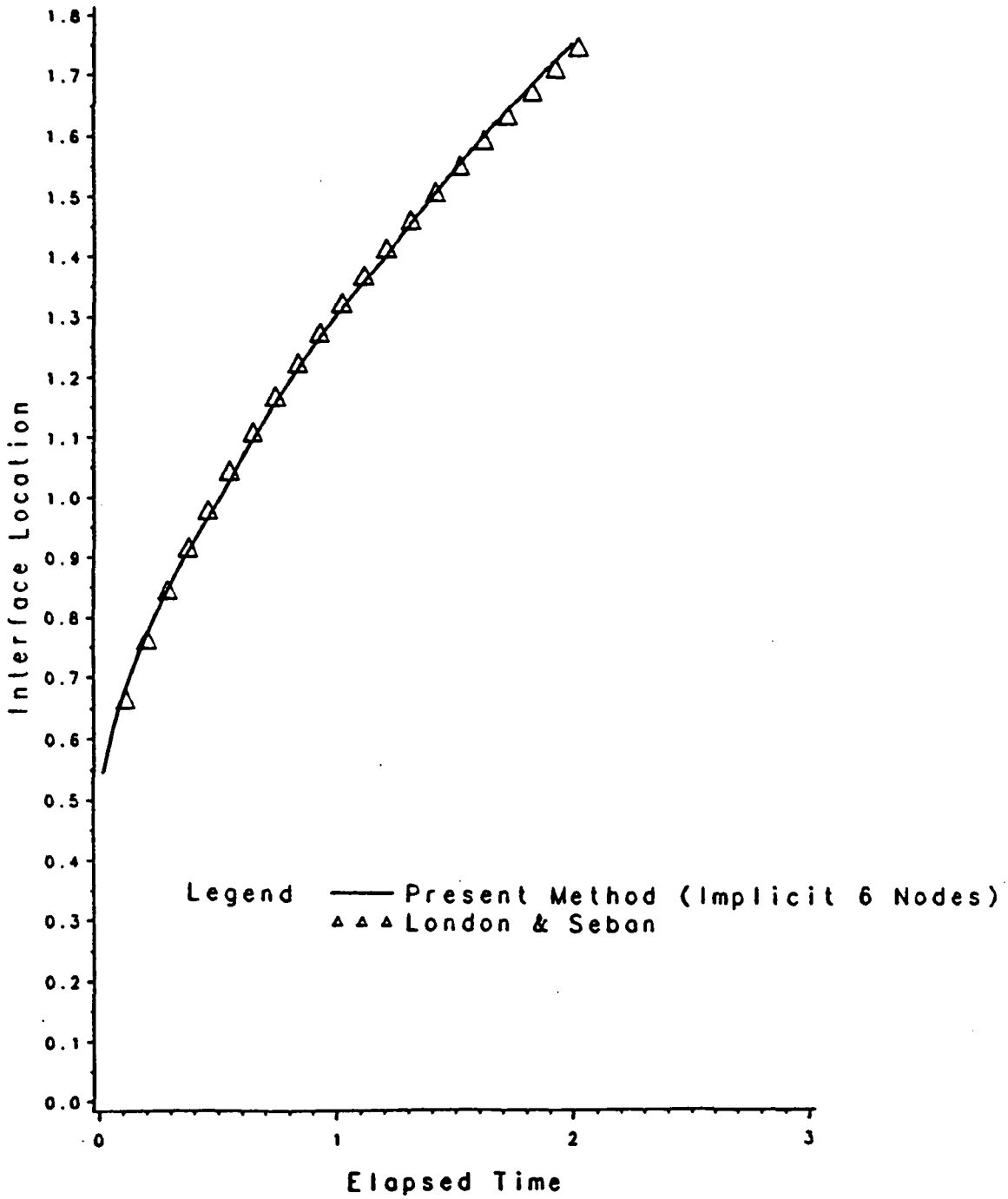

Figure 2.16 Comparison of the interface location with the analytic result subject to constant temperature: implicit scheme with 6 radial nodes.

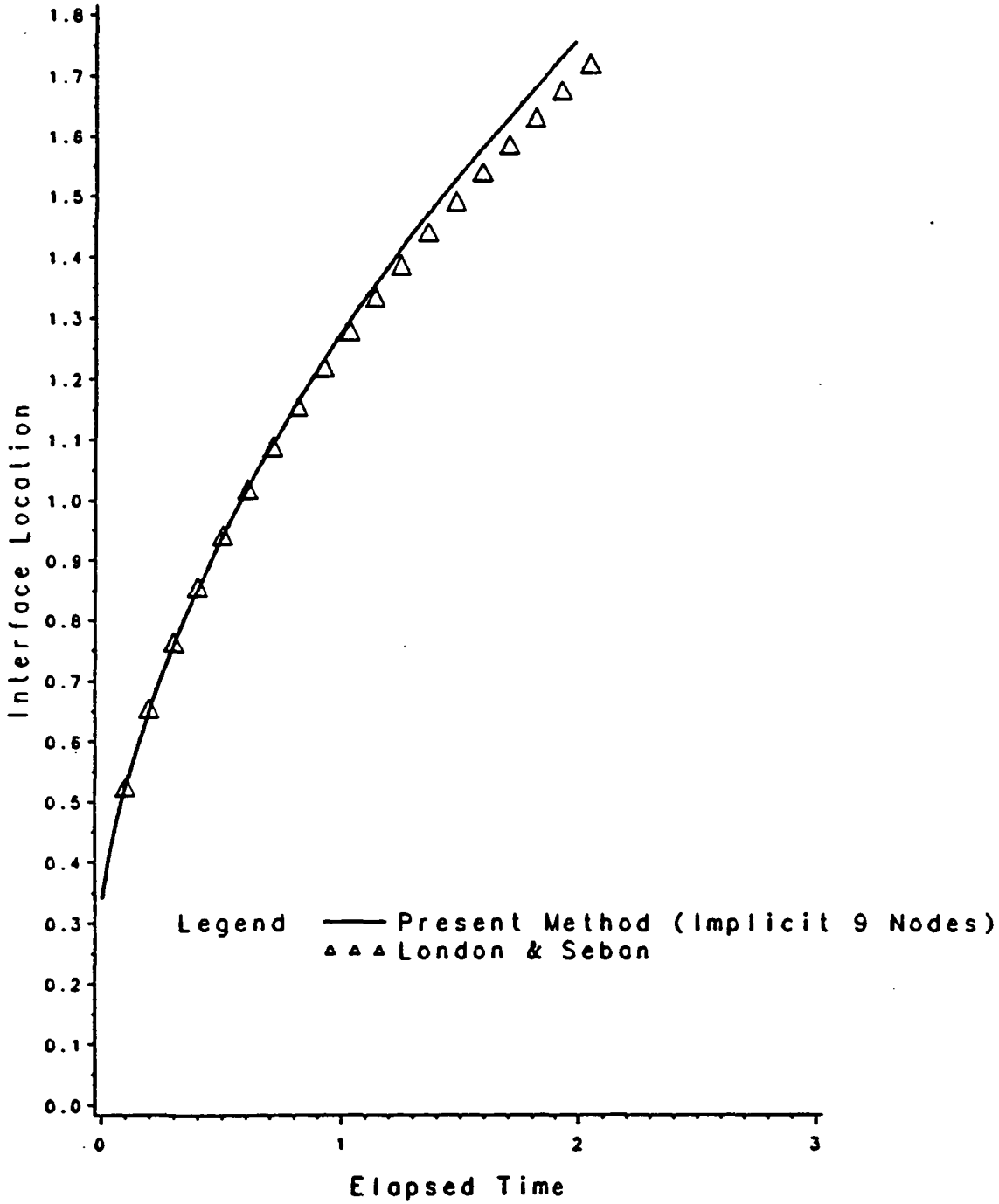

Figure 2.17 Comparison of the interface location with the analytic result subject to constant temperature: implicit scheme with 9 radial nodes.

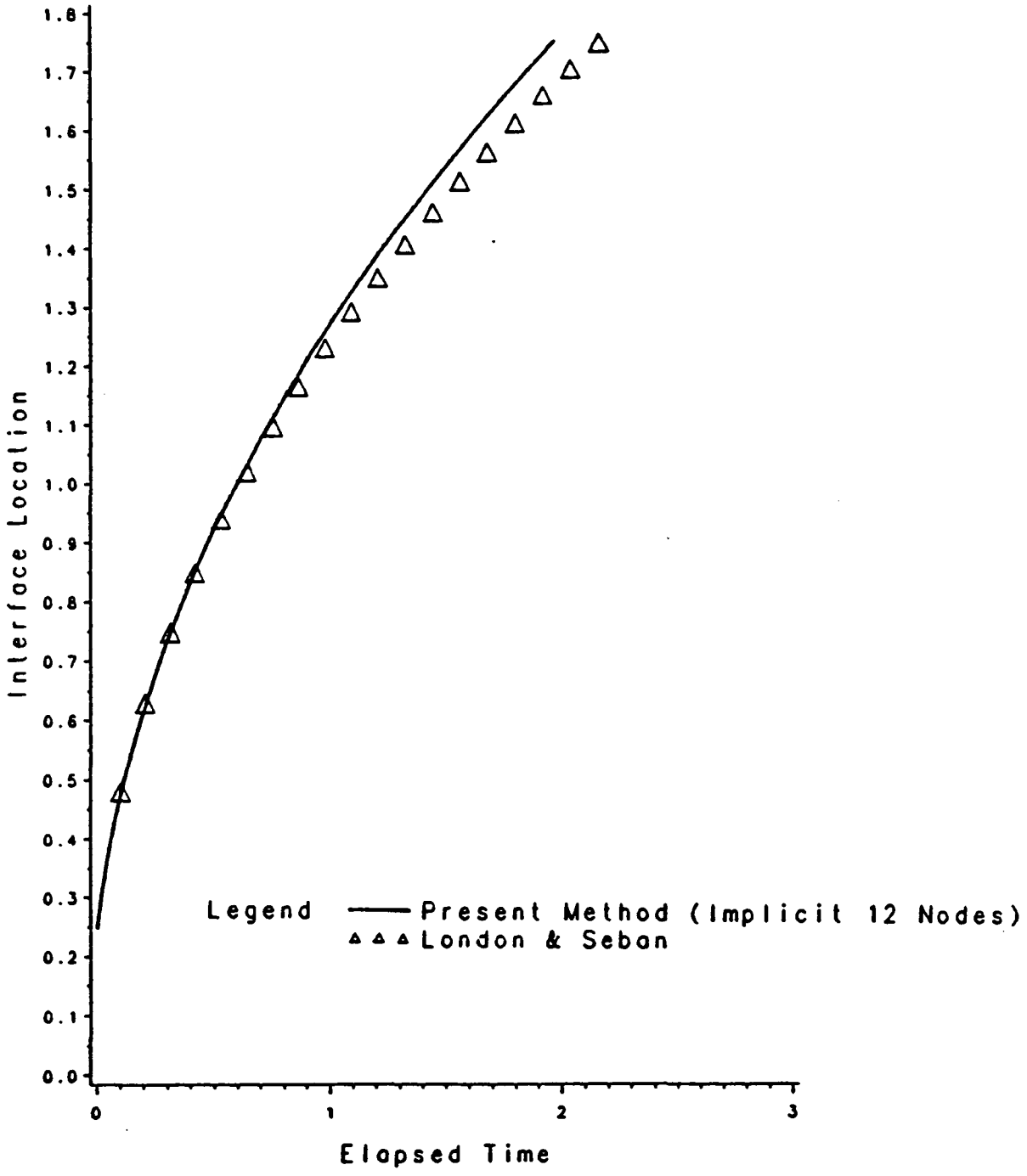

Figure 2.18 Comparison of the interface location with the analytic result subject to constant temperature: implicit scheme with 12 radial nodes.

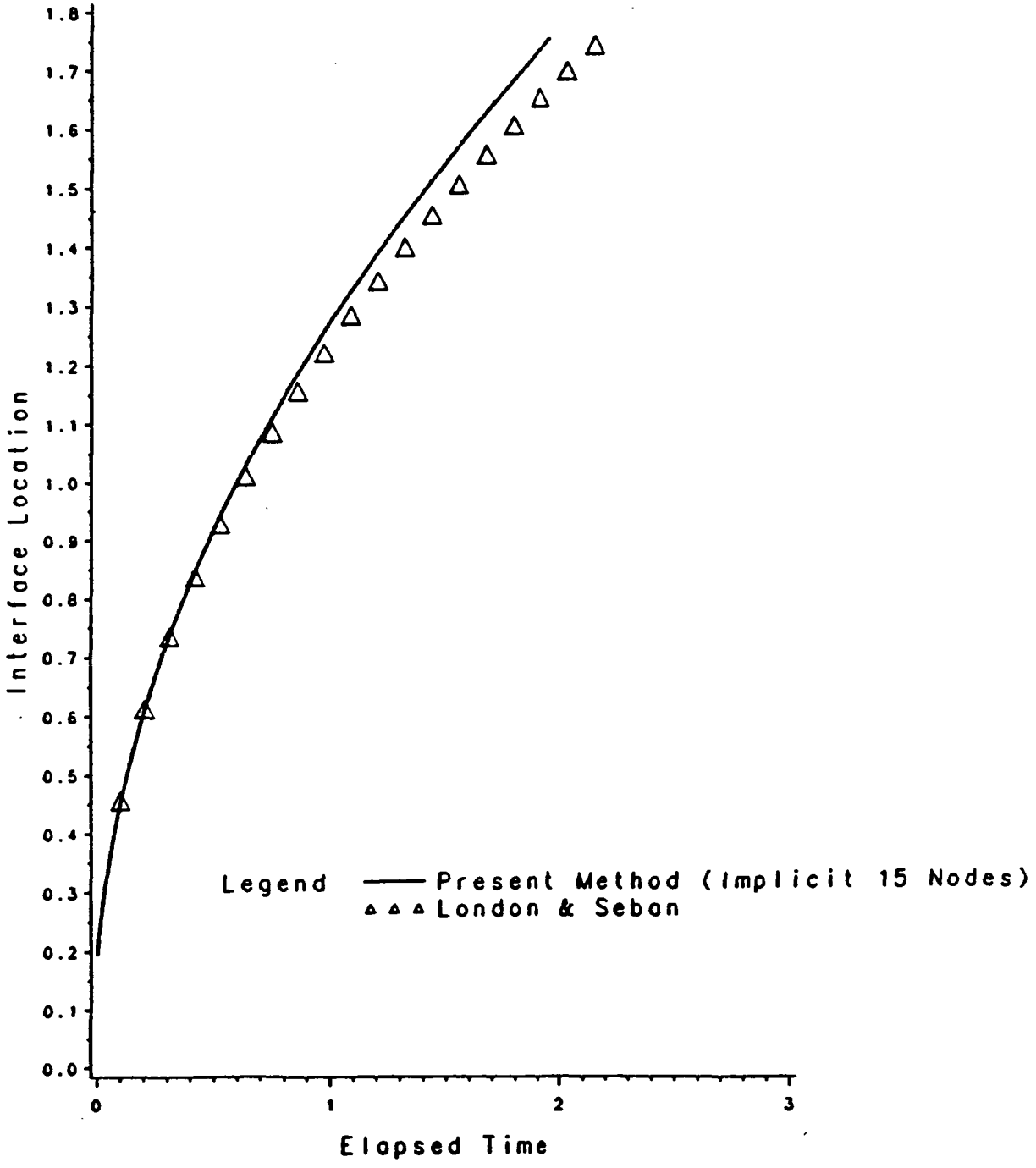

Figure 2.19 Comparison of the interface location with the analytic result subject to constant temperature: implicit scheme with 15 radial nodes.

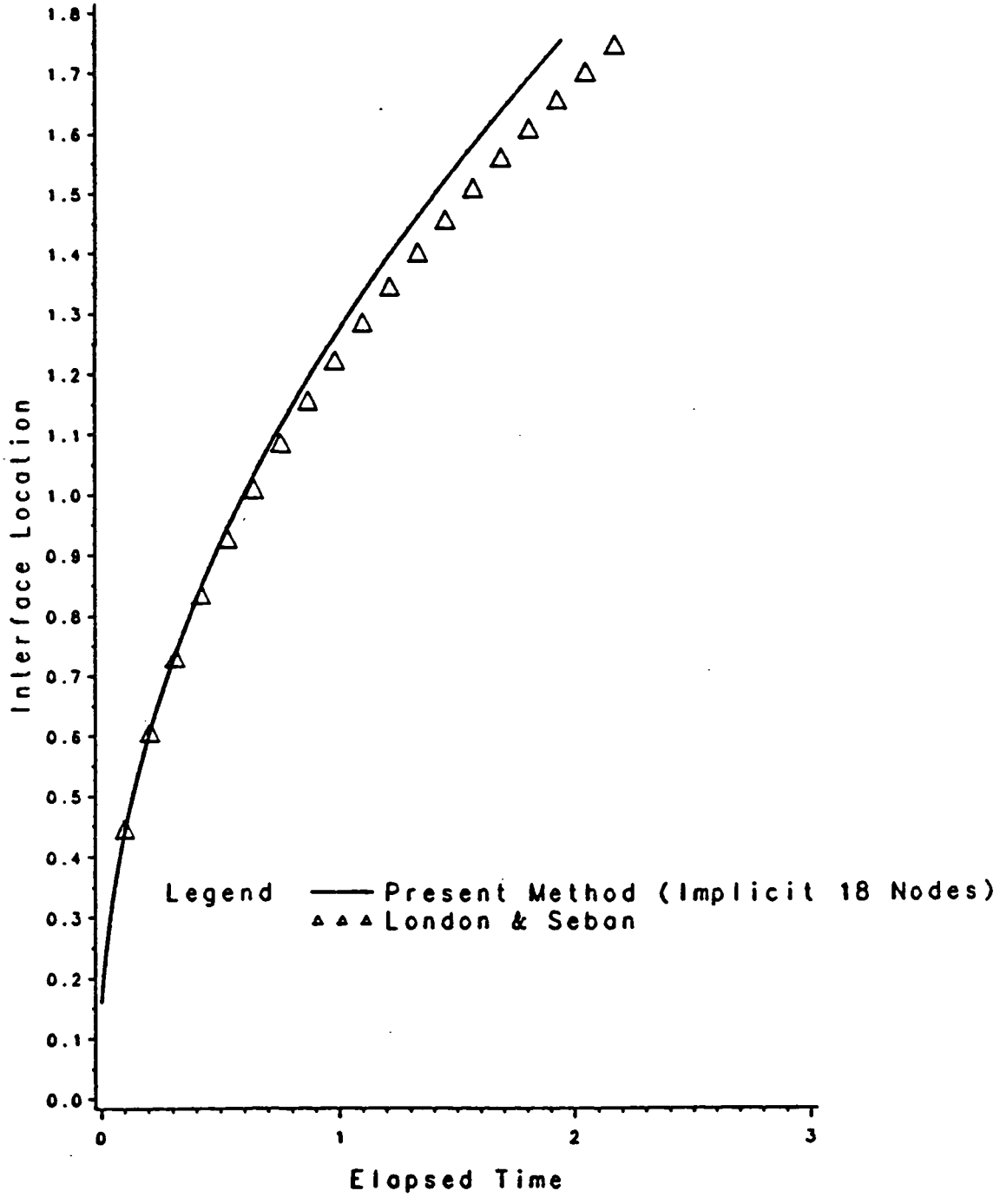

Figure 2.20 Comparison of the interface location with the analytic result subject to constant temperature: implicit scheme with 18 radial nodes.

CHAPTER III

NATURAL CONVECTION ANALYSIS IN ENCLOSURES

3.1 Introduction

Natural convection in open cavity has received growing attention because of its important role in solar thermal central receiver system as well as other engineering systems. Minimizing and predicting energy losses by natural convection are major design criteria in such solar systems. During the ground testing of the space solar dynamic system, convection heat transfer due to bouyancy force occurs inside the cavity receiver between the inner surface and the surrounding media i.e., air. Accurate calculation of convection loss through the aparture is need for proper prediction of the receiver heat transfer and further the overall performance of the system.

A review of literture concerned with central receivers has shown that very little sophistication is currently being used to analyze convective losses. Complexity of the problem has necessitated making simplifying assumptions in order to solve the problem. However, reviewing the results of these analysis with other thermal analyses, it was found that the assumptions are oversimplified. Therefore, more rigorous analytical modeling is necessary for the fluid motion and heat transfer and detailed understanding of thermal stratification is needed to

be developed. Comparison of the results for receiver convection loss, will be presented in Chapter 4. A mathematical model has been developed for predicting heat transfer by free convection in a closed container and the results are finally compared with available experimental and numerical data.

This chapter describes an effort to analize natural convection inside enclosures. Earlier methods applied to convective heating analyses are reviewed. Free convection analysis for vertical flat plate has been used in many internal flow analysis as a important extreme case. Schmidt and Beckmann (1930) performed the first experimental and theoretical work concerning the free-convection flow of air subject to the gravitational force about a vertical flat plate, which is considered as the most complete treatment of this subject. Eckert (1948) has further verified and extended the experimental results of Schmidt and Beckmann, and Schuh (1948) has extended the numerical calculations by computing the velocity and temperature distributions for several Prandtl numbers. Ostrach (1951) obtained the same results as Schmidt and Beckmann via more general approach that demonstrates the significance of all the important parameters and assumptions associated with the free-convection flow phenomenon and indicates the quantitative limitations of the theory. More information on the free-convection flow was obtained from Ostrach's work for Prandtl numbers corresponding to those of liquid metals, gases, liquids, and very viscous fluids. Further analysis has been performed by Sparrow (1955) for non-uniform boundary conditions and by Siegel for transient free-convection problem utilizing the Karman-Pohlhausen method.

Among some earlier work for flow inside a circular cylinder, Lighthill (1953) used analytical techniques in solving the problem of cooling turbine blades. He employed an integral-momentum, boundary layer analysis to predict the flow and heat transfer due to free convection in heated vertical tubes. Also in his work,

three different regimes for both laminar and turbulent flow were characterized, namely; boundary layer regime, similarity regime and non-similarity regime and equation for nusselt number has been derived for each of the flow regimes. For turbulent flow, he derive the following simple relation for the boundary layer regime by extrapolating previous experimental results.

$$Nu_\tau = 0.11\, Ra_\tau^{1/3} \tag{3.1}$$

Stratification in cryorgenic propellant storage tanks has stimulated a number of papers on the subject of convection in large enclosures where the boundary layer flow does not occupy a major portion of the enclosure volume. Clark (1965) suggested the subdivision of the flow field into three regions. In his model, a flat-plate, natural convection, boundary-layer flow is assumed along the heated wall. The flow is discharged into an upper stratified region, and the bulk temperature below this region is assumed constant. However he noted that one of the restrictions of this approach is that the assumption of a constant bulk temperature is not appropriate except during short start-up time. Later, Evans et al. (1968) presented an analytical model using similar divisions fot the flow field as suggested by Clark. Hess and Miller (1979) analyzed axisymmetric natural convection flows experimently using laser Doppler velocimeter and also developed a numerical model with the aid from their experimental data. They also noted that both Lighthill and Ostrach did not consider the interaction between the boundary layer and the core, which is necessary condition for a complete enclosure.

Schwind and Vliet (1964) studied the natural convection and stratification phenomenon of fluids in a vessel with heated sidewalls using the schlieren and shadowgraph techniques. They also confirmed the above deficiency noted by

Clark in using constant bulk temperature.Their finding was a result of studying analogy between pressure gradient in the forced convection and bulk temperature gradient in the natural convection. Tatom et al. (1963) performed experimental tests under various environmental conditions to study thermal stratification of liquid hydrogen in rocket propellant tanks. Hiddink et al. (1976) performed an experimental work to develop a better understanding of the mechanism of heat transfer within heated liquid in a closed container. This analysis was initiated from a special interest in heat sterilization of liquid food in cans or glass jars.

3.2 Numerical Modeling of Enclosure Flow

In this analysis, the following assumptions have been made:

1. The Boussinesq approximation is applicable.
2. The effect of the wall curvature is negligible.
3. Boundary layer approximations are applicable to the flow near the vertical walls.
4. The radial distributions of the vertical velocity and the temperature in the boundary layer can be approximated by functions containing four parameters (U_m, δ_0, T_w, and T_c). These parameters are function of vertical position and time.

Reviewing the previous work for the enclosure free convection analysis, it has been found that four regions can be identified, namely; 1) the wall, 2) boundary layer region, 3) mixing region, and 4) core region for the case of the side wall heating. Also another region (low-mixing region) can be added for the case of side and bottom heating in addition to the above four regions. In this chapter, only side-wall heating is considered.

3.2.1 *Wall of the Enclosure*

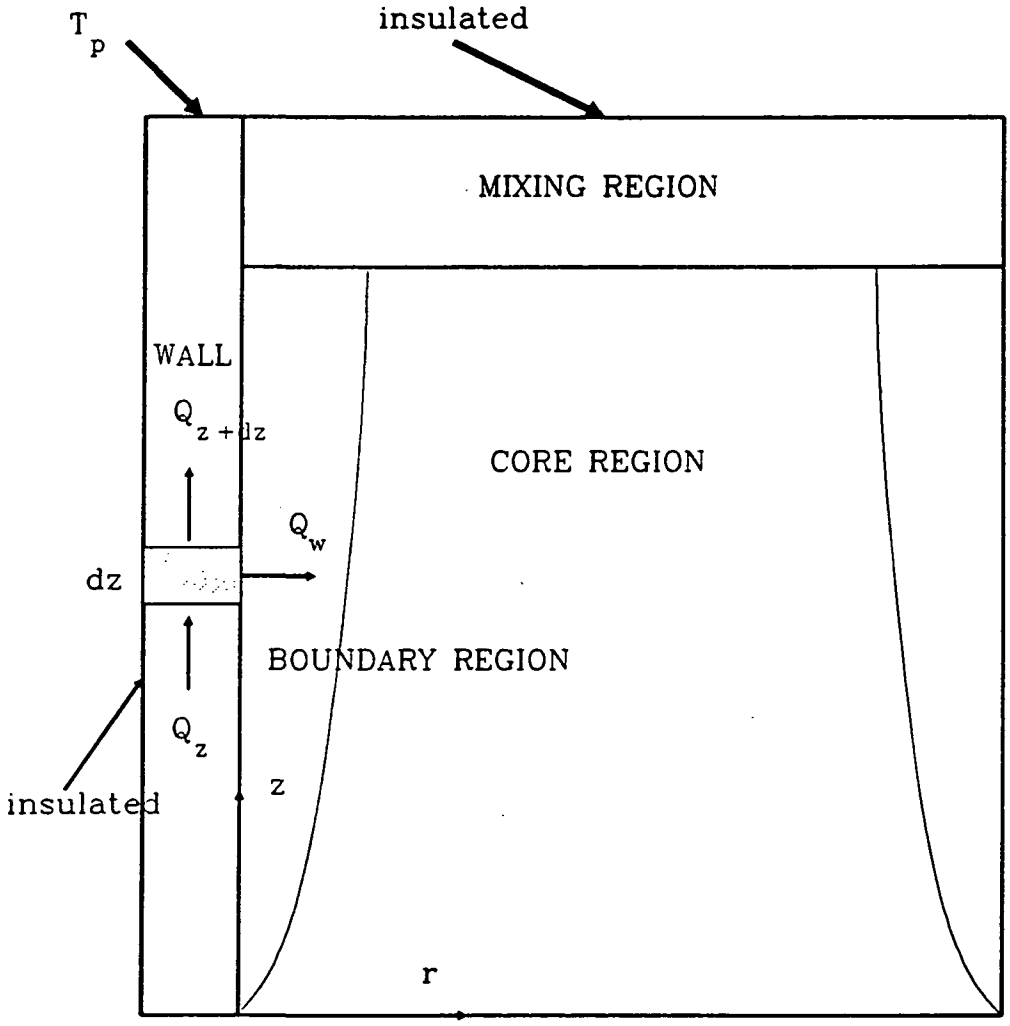

Figure 3.1 Schematic representation of various region in an enclosure for side-wall heating and energy balance for the wall node.

In most practical applications, the ratio of the length of the wall to the wall thickness (L/b) is very large, and the wall can be treated as a fin. The external side of the fin is insulated while the internal side discharges heat to the fluid at a rate determined by the local temperature difference between the wall and the core of the fluid. As energy balance shown in Figure 3.1 , part of the energy from the source is used to heat up the wall and the other part heats up the fluid. it is assumed that the characteristic time of heating the wall is much smaller than the characteristic time of heating the fluid.

The governing equation will then be:

$$\frac{\partial T_w}{\partial t} = \alpha_w \frac{\partial^2 T_w}{\partial z^2} - \frac{\alpha_w h}{k_w b}(T_w - T_c) \tag{3.2}$$

Equation 3.2 is non-dimensionalized using the following parameters:

$$t = \frac{r_T^2}{\alpha_f}\tau, \quad z = L\,Z$$

The final form of the energy equation in the wall is then obtained:

$$\frac{\partial T_w}{\partial \tau} = \frac{1}{A^2}\frac{\alpha_w}{\alpha_f}\frac{\partial^2 T_w}{\partial Z^2} - \mathcal{M}_\tau h(T_w - T_c) \tag{3.3}$$

where,

$$\mathcal{M}_\tau = \frac{\alpha_w r_T^2}{\alpha_f k_w b}$$

To solve Equation 3.3, the heat transfer coefficient must be known in advance. As will be shown in the next section, h can be expressed in terms of the boundary layer thickness δ_0. In the first time step it is assumed that $h = 0$. The solution to Equation 3.3 is obtained with Thomas algorithm implicit finite

difference scheme. The wall equation can then be expressed in finite difference form:

$$\frac{T_{w_i}^{n+1} - T_{w_i}^{n}}{\Delta\tau} = \frac{1}{A^2}\frac{\alpha_w}{\alpha_f}\frac{T_{w_{i+1}}^{n+1} - 2T_{w_i}^{n+1} + T_{w_{i-1}}^{n+1}}{(\Delta z^*)^2} - \mathcal{M}_r\, h^n (T_{w_i}^{n+1} - T_{c_i}^{n}) \tag{3.4}$$

The boundary conditions to Equation 3.4 are:

$$\frac{\partial T_w}{\partial Z} = 0 \qquad \text{at } Z = 0$$

$$T_w = T_p \qquad \text{at } Z = 1$$

While initial condition is:

$$T_w = T_I \qquad \text{at } \tau = 0$$

The Thomas algorithm is used to invert the tri-diagonal matrix that results from expressing Equation 3.4 at every node i.

3.2.2 *The Boundary Layer Region*

The new wall temperature is used to update the buoyant force, and we can now proceed to evaluate the boundary layer thickness, δ_0, and the distribution of maximum velocity, U_m. These governing equations are the integral form of the momentum and energy boundary layer equations. The governing equations can then be expressed as:

$$\frac{\partial}{\partial\tau}\int_0^{\delta_0} U\,dr + \frac{\partial}{\partial z}\int_0^{\delta_0} U^2\,dr = \int_0^{\delta_0} -\frac{1}{\rho_f}\frac{\partial P}{\partial z}\,dr + \nu_f \left.\frac{\partial U}{\partial R}\right|_{\delta_0} - \nu_f \left.\frac{\partial U}{\partial r}\right|_{r=0} + g\beta_f \int_0^{\delta_0} (T_f - T_c)\,dr \tag{3.5}$$

$$\frac{\partial}{\partial \tau}\int_0^{\delta_0}(T_f - T_c)\,dr + \delta_0\frac{\partial T_c}{\partial \tau} + \frac{\partial}{\partial z}\int_0^{\delta_0} U(T_f - T_c)\,dr + \frac{\partial T_c}{\partial z}\int_0^{\delta_0} U\,dr = -\alpha_f \frac{\partial T_f}{\partial r}|_r = 0 \tag{3.6}$$

where it has been assumed that $\delta_T = \delta_0$. The effect of the dynamic pressure will be neglected in the present analysis, although this effect can be very important near the top and bottom walls of the enclosure. It is through this dynamic pressure that the top and bottom influence the flow field, imposing a zero velocity at both ends.

In order to solve the set of coupled Equations 3.4 and 3.5, we must have suitable expressions for the radial variation of the temperature and axial velocity inside the boundary layer. These profiles constitute an a priori knowledge of the solution, which is obtained from experimental data and/or another solution. The unknown parameters then become: the boundary layer thickness (δ_0), the maximum velocity at any height (U_m), the wall temperature (T_w), and while temperature in the core (T_c).

The velocity profiles must satisfy the following boundary conditions:

(1) $U = 0$ at the wall

(2) $U = 0$ at δ_0

The temperature profiles must satisfy the following boundary conditions:

(1) $T = T_w$ at $r = 0$

(2) $T = T_c$ at $r = \delta_0$

In addition, these expression for the velocity and the temperature must closely follow the shape of the distributions obtained experimentally.

The velocity profile can be assumed as following form:

$$\frac{U}{U_m} = C_1\left(\frac{r}{\delta_0}\right) + C_2\left(\frac{r}{\delta_0}\right)^2 + C_3\left(\frac{r}{\delta_0}\right)^3 + C_4\left(\frac{r}{\delta_0}\right)^4 \tag{3.7}$$

and the temperature profile can be approximated by the following form:

$$\frac{T_f - T_c}{T_w - T_c} = \left(1 - \frac{r}{\delta_0}\right)^a \tag{3.8}$$

where a and C_i are usually determined from experiment.

To generalize the governing equations, we introduce the functions that represent the velocity and the temperature profile parameters:

$$f(r') = \frac{U(z,r,t)}{U_m(z,t)} \tag{3.9}$$

$$g(r') = \frac{T(z,r,t) - T_c(z,t)}{T_w(z,t) - T_c(z,t)} \tag{3.10}$$

where $r' = r/\delta_0$. Also following integrals and shear stress S are introduced:

$$\begin{aligned} I_1 &= \int_0^1 f(r')\,dr', \quad I_2 = \int_0^1 f^2(r')\,dr', \quad I_3 = \int_0^1 g(r')\,dr', \\ I_4 &= \int_0^1 f(r')g(r')dr', \quad S = \left.\frac{\partial f(r')}{\partial r'}\right|_{r'=1} - \left.\frac{\partial f(r')}{\partial r'}\right|_{r'=0} \end{aligned} \tag{3.11}$$

the Equations 3.5 and 3.6 are now non-dimensionalized using the following parameters:

$$\begin{aligned} t' &= \frac{\alpha_f\, t}{r_T^2}, \quad U' = \frac{r_T\, U}{\alpha_f}, \quad z' = \frac{z}{L}, \\ \theta &= \frac{T_w - T_c}{(T_p - T_I)}, \quad \eta = \frac{\delta_0}{r_T}, \quad A = \frac{L}{r_T} \end{aligned} \tag{3.12}$$

Resulting momentum and energy equations are given as

$$\begin{aligned} &I_1\eta^2\frac{\partial U'_m}{\partial \tau} + I_1 U'_m \eta \frac{\partial \eta}{\partial \tau} + \frac{I_2 U'^2_m \eta}{A}\frac{\partial \eta}{\partial z'} \\ &+ \frac{2I_2\eta^2 U'_m}{A}\frac{\partial U'_m}{\partial Z'} = S\,\mathrm{Pr}\,U'_m + \mathrm{Ra}_w \mathrm{Pr}\,\eta^2 I_3 \end{aligned} \tag{3.13}$$

and

$$I_3\eta^2\frac{\partial\theta}{\partial\tau}+I_3\eta\,\theta\frac{\partial\eta}{\partial\tau}+\frac{\eta^2}{\Delta T}\frac{\partial T_c}{\partial\tau}+\frac{I_4\eta}{A}\left(U'_m\theta\frac{\partial\eta}{\partial z'}+U'_m\eta\frac{\partial\theta}{\partial z'}\right.$$
$$\left.+\theta\,\eta\frac{\partial U'_m}{\partial z'}\right)+\frac{I_1\eta^2U'_m}{A\,\Delta T}\frac{\partial T_c}{\partial z'}=a\,\theta \qquad (3.14)$$

subject to the following boundary and initial condition:

$$U'_m=\eta=0 \qquad \text{at } z'=0$$

$$U'_m=\eta=0 \qquad \text{at } \tau=0$$

Equation 3.13 and 3.14 are a coupled set of hyperbolic equations for the unknowns U'_m and η as functions of z' and τ.

In Equation 3.14, the value of θ must be provided by the solution of the wall equation. This set of coupled, non-linear, partial differential equations are solved using Newton-Raphson iteration method.

3.2.3 *The Mixing Region*

The mixing region is a control volume in the uppermost part of the container, where the boundary layer discharges its energy. It is bounded by the boundary layers and has a depth H. The mixing region is considered to be important region through which the flow coming from the boundary region is entering into the core region, since unlike flat plate case, the velocity and the temperature of the boundary layer flow will affect those of the flow outside the boundary layer (core region) via mixing region in the enclosure problem like this. Therefore accurate prediction of the flow characteristics in that region would improve the solution for the whole heating process.

An energy balance in this control volume (Figure 3.1) provides the average mixing temperature T_m. This temperature serves as the boundary condition to

the core. It is assumed to be in the middle of the mixing region. The energy balance states that: the energy convected by the boundary layer at H plus the heat convected into the fluid between the top and H equals the energy stored in the mixing region plus the energy that leaves the mixing region at a velocity U_c. That is:

$$\begin{aligned}
&\int_0^{\delta_0} \rho_f U\, Cp_f\, T_f\, 2\pi(r_T - r)\, dr\Big|_{z=L-H} + 2\pi r_T \int_{L-H}^{L} q_w\, dz \\
&= \rho_f\, Cp_f\, \pi(r_T - \delta_0)^2 H \frac{dT_M}{dt} + \rho_f\, C_f\, 2\pi \frac{dH}{dt} \int_0^{r_T} (T_M - T_f)(r_T - r)\, dr \qquad (3.15) \\
&- \int_{\delta_0}^{r_T} \rho_f\, U_c\, Cp_f\, T_m\, 2\pi(r_T - r)\, dr\Big|_{z=L-H}
\end{aligned}$$

where the heat flux q_w is obtained by

$$q_w = \frac{k_f\, a}{\delta_0}(T_w - T_c)$$

The initial condition to Equation 3.9 is:

$$T_M = T_I \qquad \text{at } t = 0$$

The solution of Equation 3.9 provides T_M, which is assumed to be the temperature in the center of the mixing region ($z = L - H/2$). It is still not clear what is the best method of estimating the temperature profile above the middle of the mixing region. It is reported that parabolic temperature profile for this region under-estmates the temperatures near the top which results in a larger driving force than actual situation. Consequently, instead of parabolic profile, following power function has been used for the temperature profile with prescribed T_m at the mixing region.

$$y = a/(x^2 + b)$$

A special form of this curve is called 'Witch of Agnesi' when $a = b^{3/2}$, and these curves automatically satisfy the boundary condition at the top (insulated). In Figure 3.3, excellant agreement has been obtained with this profile for the same test case of Hess (1982).

3.2.4 *The Core Region*

The temperature of the core is assumed to be constant in the radial direction, which is close to the behavior shown by the numerical solution. It is allowed to vary with the axial coordinate and with time. The equation that defines the temperature in the core is:

$$\frac{\partial T_c}{\partial t} + U_c \frac{\partial T_c}{\partial z} = \alpha_f \frac{\partial^2 T_c}{\partial z^2} \tag{3.16}$$

where the velocity of the core can be closely expressed by:

$$U_c = \frac{-2}{(r_T - \delta_0)^2} \int_0^{\delta_0} U(r_T - r)\, dr \Big|_{z=L-H}$$

Neglecting the effect of curvature, the core velocity can be rewritten as:

$$U_c = -\frac{2}{R_o} \int_0^{\delta_0} U\, dr \Big|_{z=L-H}$$

and using the definitions in Equation 3.11 it can be expressed as:

$$U_c = -2 I_1 U_m \Big|_{\max} \eta_{\max} \tag{3.17}$$

Equations 3.17 and 3.18 are non-dimensionalized using Equation 3.12. The resulting expressions are:

$$\frac{\partial T_c}{\partial \tau} + \frac{U_c'}{A}\frac{\partial T_c}{\partial z'} = \frac{1}{A^2}\frac{\partial^2 T_c}{\partial z'^2} \tag{3.18}$$

and

$$U_c' = -2I_1 U_m'\Big|_{\max} \eta_{\max} \tag{3.19}$$

The boundary conditions to the energy equation are:

$$T_c = T_M \qquad \text{at } z' = 1 - \frac{H}{2L}$$

The solution to Equation 3.19 is obtained with an implicit finite difference scheme. The method proceeds by updating the wall temperature which, in combination with the core temperature of the previous time, provides the driving force, θ, necessary to solve the parameters of the boundary layer.

3.3 Results and discussion

The results obtained with the integral analysis with revised temperature distribution in the mixing region are varified by comparing with those from Hess (1982) and from Miller (1977) who solves the same problem using full Navier-Stokes equation. Comparison of the velocity profiles with the result of Hess for the sample cases are presented in Figures 3.2 to 3.5 for two different Rayleigh numbers. In the Figures, solid lines with symbols represent present results , and dashed lines and symbols represent the results from Miller and Hess respectively.

Figure 3.2a shows the variation of the velocities vs. enclosure height at three different times, namely, 60, 180 and 360 seconds for Ra=3.73×10^8. Also, Figure 3.2b shows similar results for Ra=7.46×10^8. From these figures, it is noted that the present results compare fairly well with the numerical solution and matchs to the Miller's numerical results better than Hess's integral results particularly for later time (t=360 sec.).

Figure 3.3a shows the variation of the core temperatures vs. enclosure height at the three different times mentioned above for Ra=3.73×10^8. Also, Figure 3.3b shows similar results for Ra=7.46×10^8. From these figures, it is noted that, with the use of power function for temperature profile in the mixing region, excellent agreement has been obtained with the Miller's results at all three times.

Again, Figure 3.4b shows the variation of the wall temperature vs. enclosure height at the three different times mentioned above for Ra=3.73×10^8. While Figure 3.4b shows similar results for Ra=7.46×10^8. The present integral results compare well with the Miller's solution except in the early time. That can be attributed to the fact pointed by earlier investigators that the boundary layer assumption is not valid at early times. Accordingly, this analysis can be appropriate for the solar receiver analysis which involves cylic behavior which requires substantial period of time to achieve steady results.

In Figure 3.5a , the variation of the local Nusselt number vs. enclosure height at four different times (60, 120, 300, 420 sec.) are plotted for Ra=3.73×10^8. Also, similar results is shown in Figure 3.5b for Ra=7.46×10^8. The present solution is compared with the numerical results and very good agreement was obtained. The following can be noticed from this figure:

1.) There is very little variation of local Nusselt number with time.

2.) The variation is almost linear which implies that h is almost a constant.

From the previous figures, it verifies the current analysis compares fairly well with the earlier numerical results and suitable for the receiver analysis which deals with cyclic variation of the parameters. Application of this analysis to the free convection analysis inside a receiver cavity will be presented in Chapter IV along with results obtained.

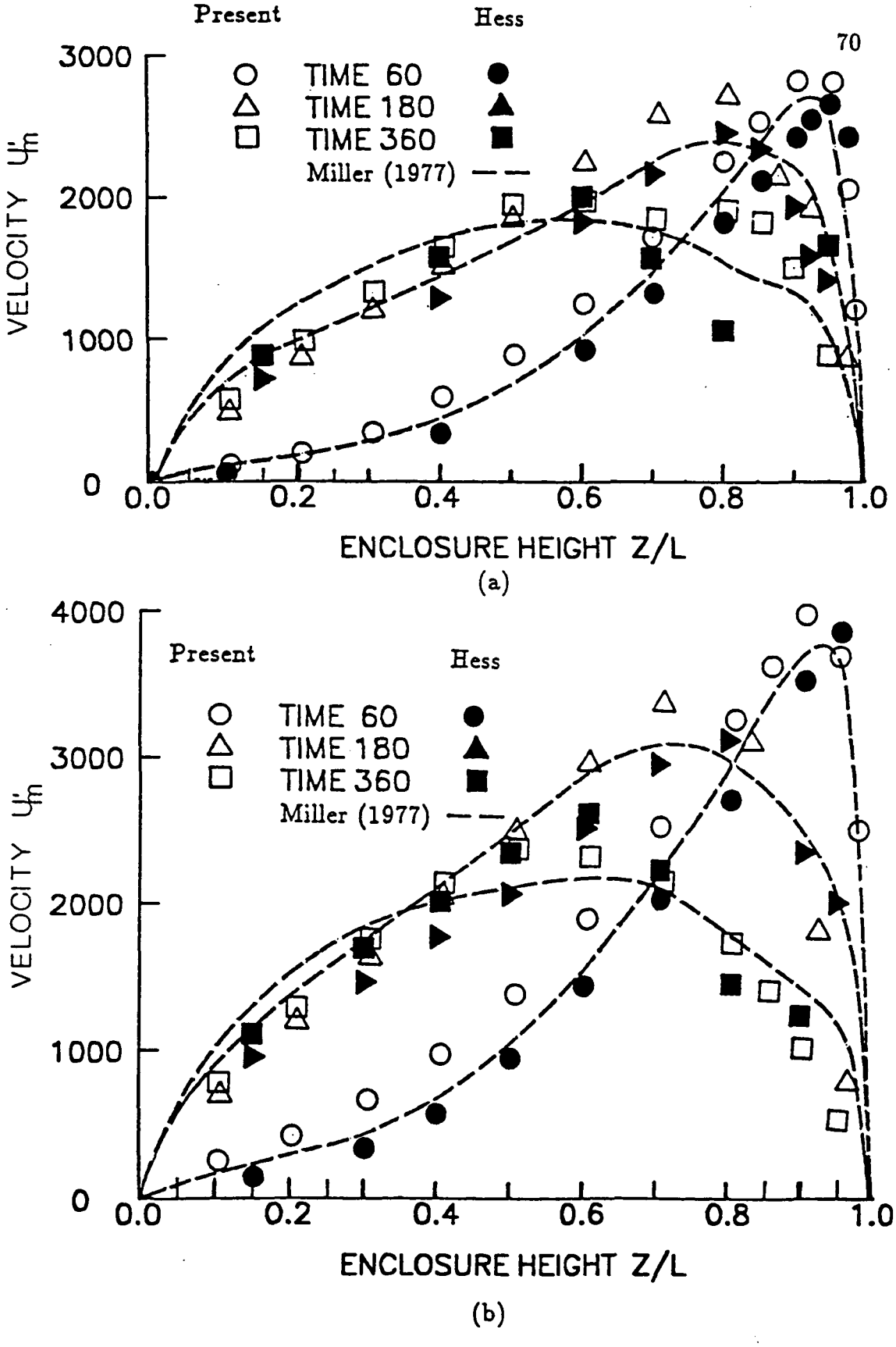

Figure 3.2 Variation of the velocities vs. enclosure height at three different times. (a) For Ra = 3.73×10^8. (b) For Ra = 7.46×10^8.

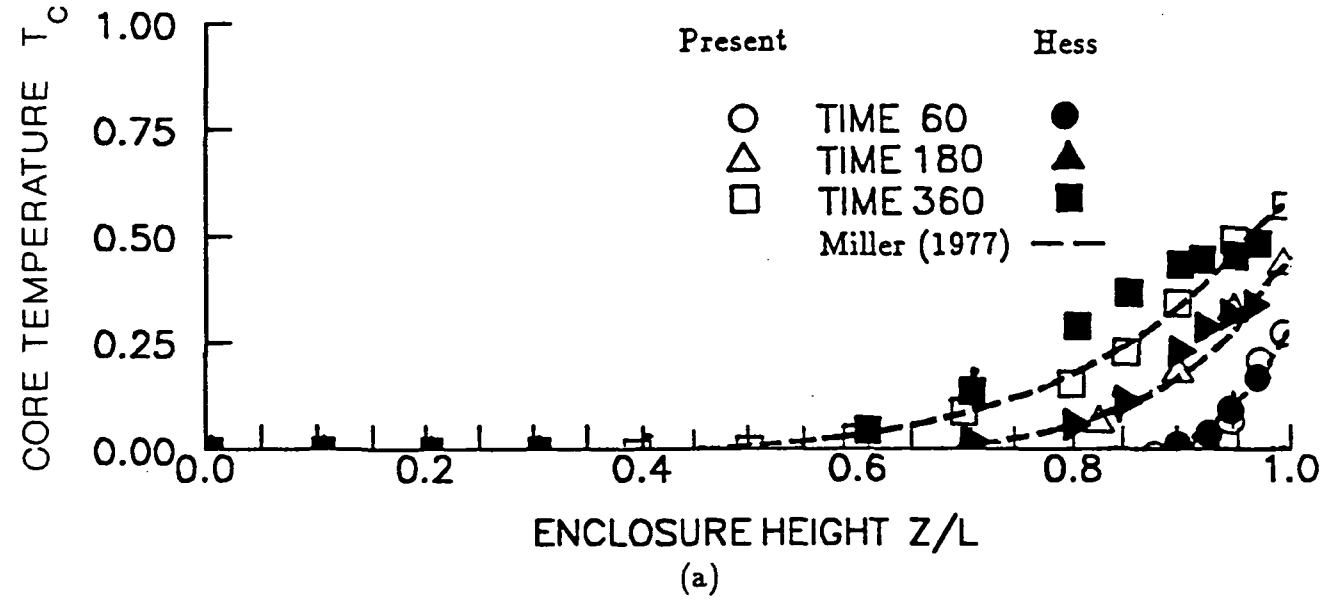

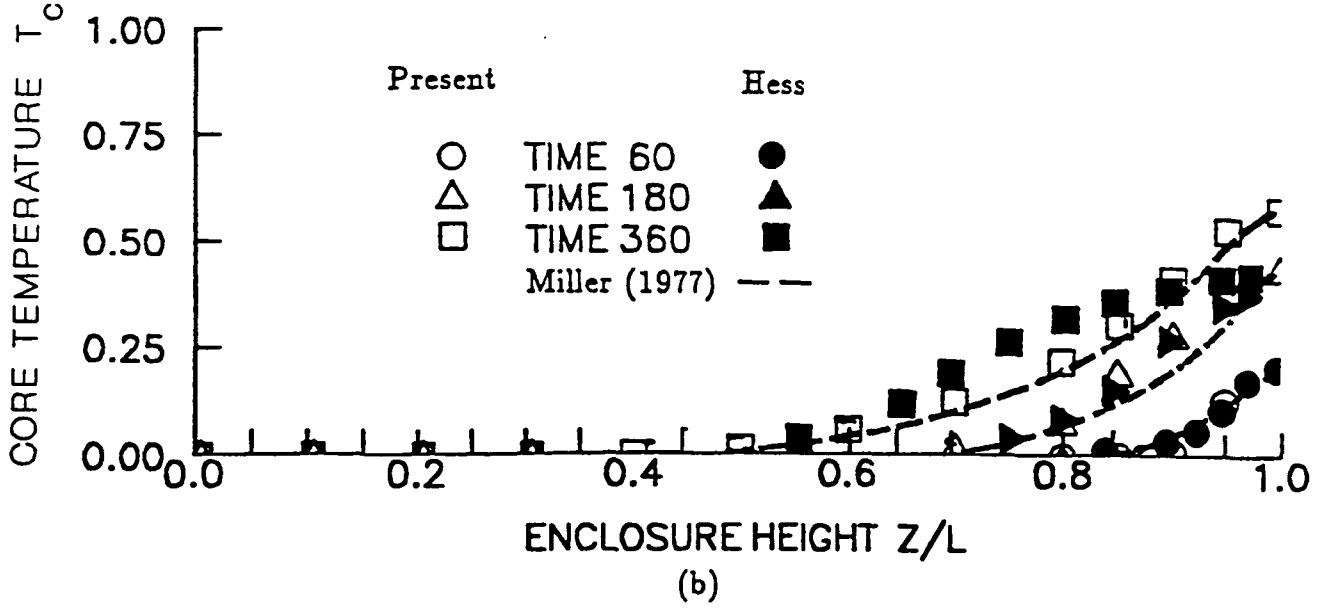

Figure 3.3 Variation of the core temperatures vs. enclosure height at three different times. (a) For Ra = 3.73×10^8. (b) For Ra = 7.46×10^8.

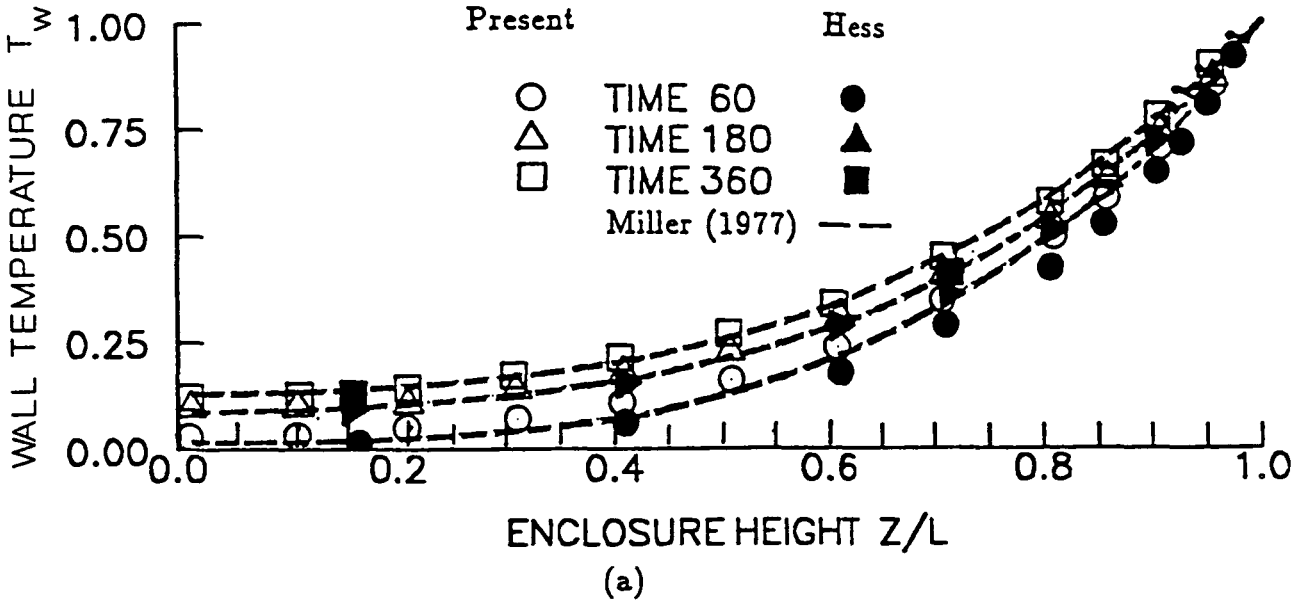

(a)

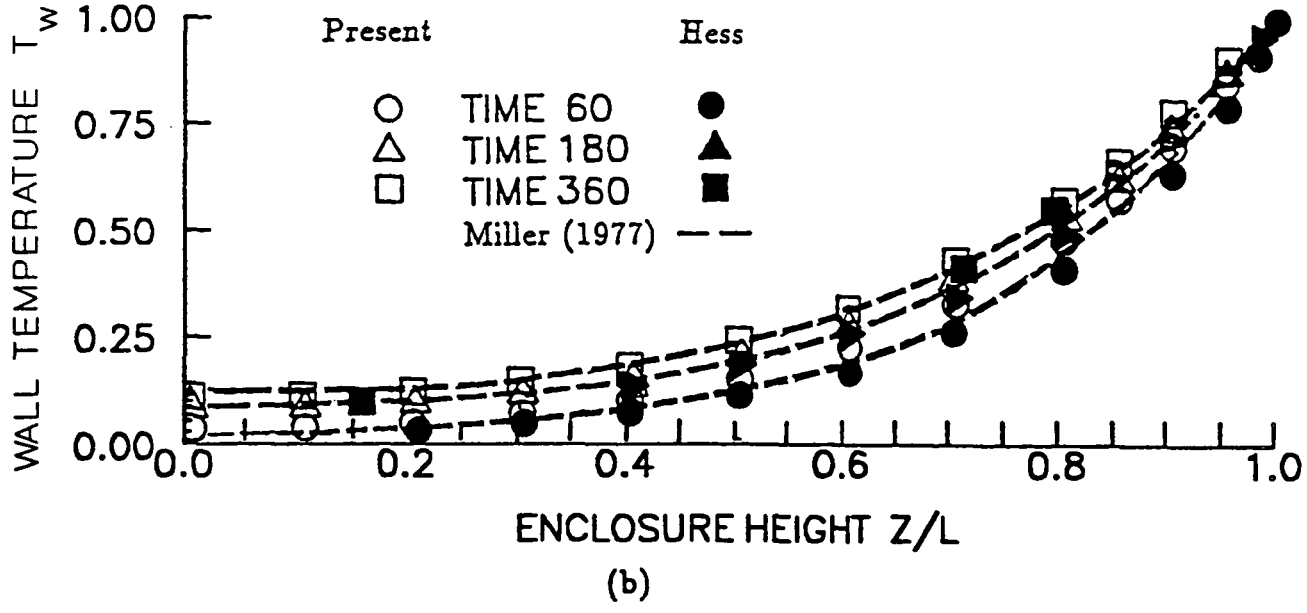

(b)

Figure 3.4 Variation of the wall temperature vs. enclosure height at three different times. (a) For Ra = 3.73×10^8. (b) For Ra = 7.46×10^8.

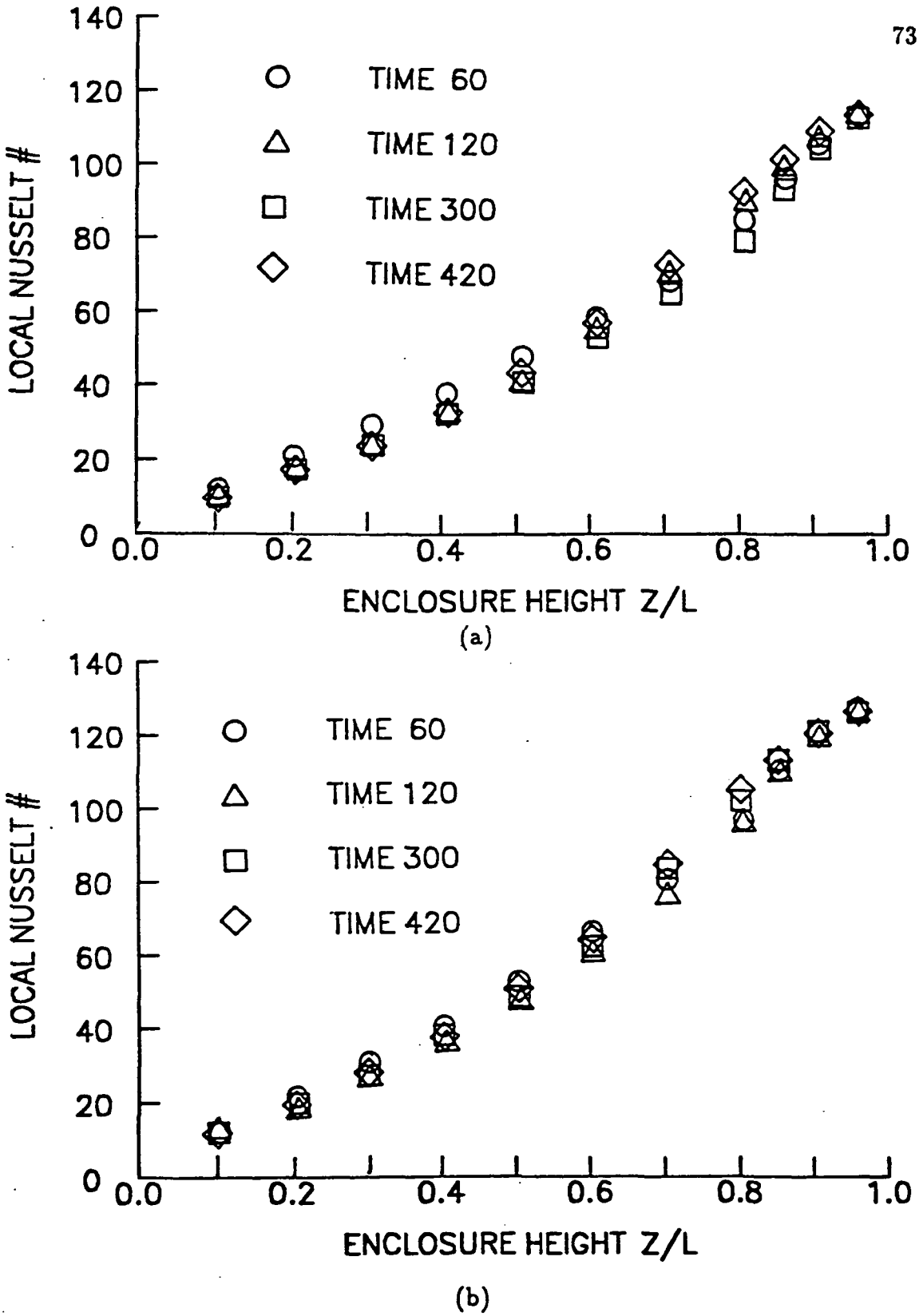

Figure 3.5 Variation of the local Nusselt number vs. enclosure height at four different times. (a) For Ra = 3.73×10^8. (b) For Ra = 7.46×10^8.

CHAPTER IV

APPLICATION TO SOLAR DYNAMIC RECEIVER ANALYSIS

4.1 Introduction

Numerical technique presented in Chapter II and III has been applied to the receiver analyser computer program, HEAP, which was discussed in Chapter I. In this chapter, more detailed description of the receiver heat transfer calculations of the HEAP code is made followed by the sample simulations of a solar receiver under the different operating conditions, namely, one on the orbit and the other on the ground.

4.2 Finite-Difference Receiver Program Methodology

4.2.1 *General Layout*

The receiver under consideration is discretized in space by nodes as shown in Figure 4.1. In this figure, each component of the receiver is represented by the finite element nodes as follows:

- Nodes 1 to 10: Working gas of the Brayton cycle,
- Nodes 11 to 20: Working gas tubing,
- Nodes 21 to 30: Phase change material of the thermal energy storage device,

- Nodes 31 to 40: Thermal energy storage containment,
- Nodes 41 and 42: Aperture plate,
- Nodes 43 to 45: Back plate,
- Node 46: Working gas inlet,
- Node 47: Aperture opening.

Heat exchange between any two arbitrary nodes (i) and (j) is illustrated in Figure 4.2. The heat transfer rate equations are written with all modes of heat transfer included. The net energy stored in each node is calculated using the first law of thermodynamics, including the energy exchange to and from each node as a result of neighboring nodes.

For the transient solution, explicit numerical technique is used. By this technique, the new temperature at time ($\tau + \Delta\tau$) is determinded using the old temperature vector at time (τ) and all other parameters evaluated at time (τ). to ensure stable computations towards convergence a special formula is used for the critical time step ($\Delta\tau$) based on the methodology stated in reference by Razelos (1973).

4.2.2 *Basic Assumptions*

The following assumptions and idealizations were made in the heat transfer calculations:

(1) The physical system under study is treated as a collection of a number of isothermal nodes with uniform optical and physical properties throughout each node. Nodes are assumed to be of axisymmetric geometry accordingly one can make use of the special radiation view factor subroutine. The axis of symmetry must coincide with the receiver axis.

(2) The nodal specific heat, thermal conductivity, and density are assumed independent of operating temperature. The properties may be taken at

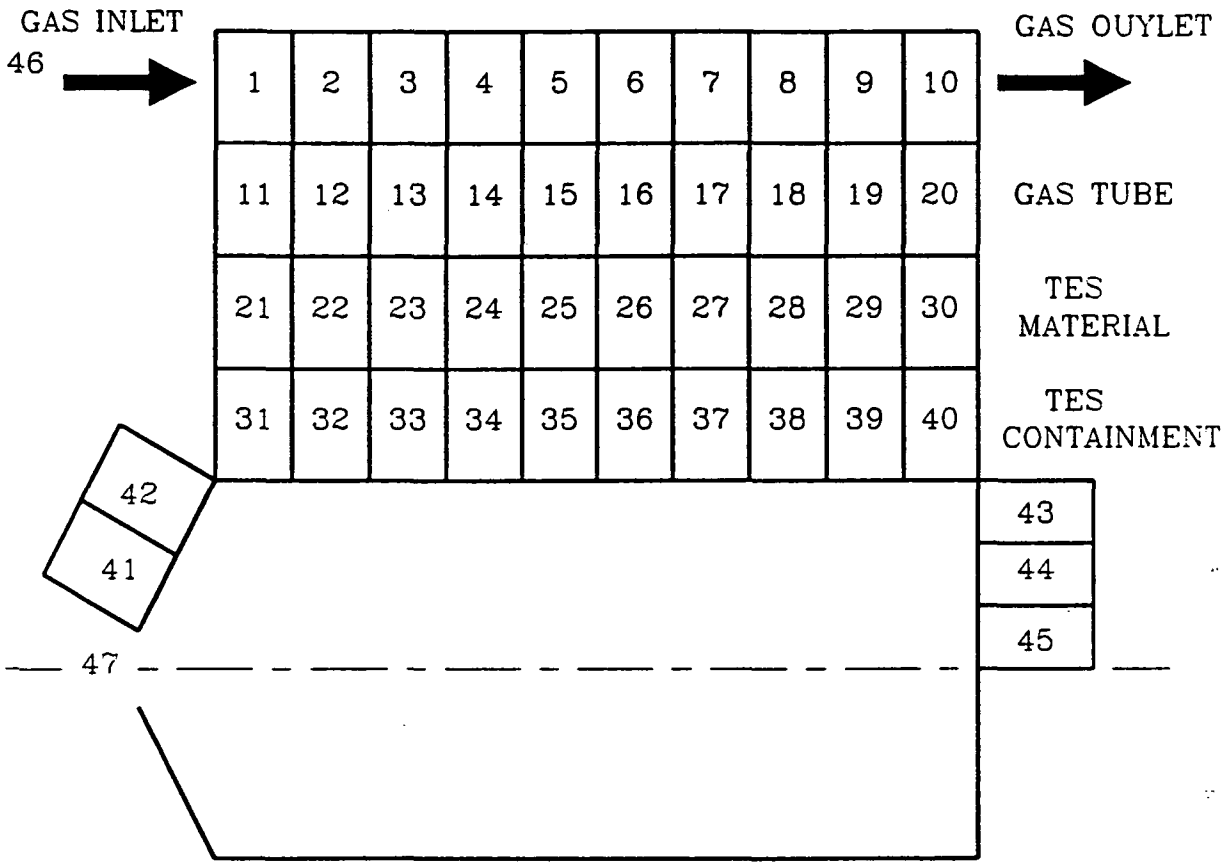

Figure 4.1 Receiver Discretization into Nodes.

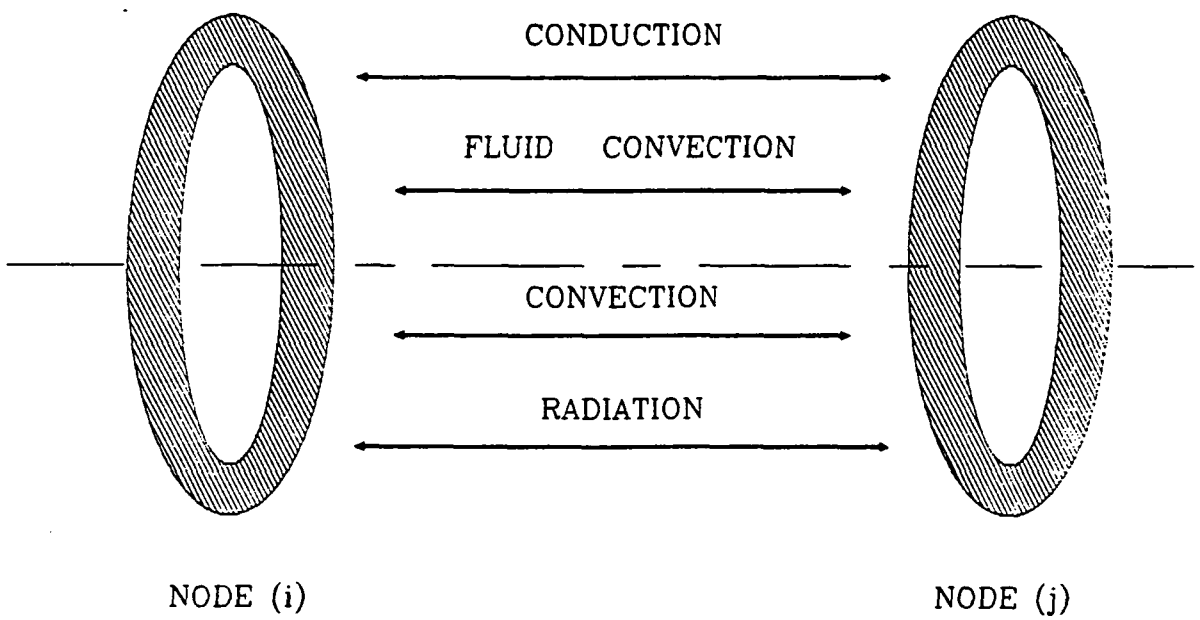

Figure 4.2 Heat exchange between node (i) and (j).

an estimated average working temperature as an approximation. However, upon consideration of the natural convection in the receiver cavity, density of the air is taken function of the temperature according to the ideal gas equation. Also, nodal infrared and solar emittances are assumed independent of both directivity and operating temperature.

(3) The radiation emitted by a node surface is assumed to be diffuse. In general, the radiation reflected from a node surface can be diffuse, specular or a combination of diffuse and specular parts. In the present model, only diffuse reflection was assumed, with a zero specular component.

(4) The optical properties of a node surface are assumed to be divided into two bands in the eletromagnetic spectrum. This "semi gray" assumption allows separate calculations of radiation energy exchange in the short wave (solar) band and the long wave (infrared) band. Consequently, the radiation energy in the program is allowed to be absorbed, reflected or emitted in the long wave region, and only absorbed or reflected in the short wave region.

(5) The nodal internal energy generation or dissipation by eletrical, chemical or nuclear effects is assumed uniform over the node surface and independent of the temperature.

Based on the above assumptions and idealizations, the heat transfer rate equations are written and analyzed as described in the following sections.

4.2.3 *Nodal Energy Balance*

For a particular receiver node (i), the energy is exchanged with the neighboring nodes by many modes of heat transfer such as:

1) Conduction, $\dot{Q}_{cond}$;

2) Thermal convection, $\dot{Q}_{conv}$;

3) Fluid convection, $\dot{Q}_f$;

4) Long wave (infrared) radiation, $\dot{Q}_{IR}$;

5) Short wave (solar) radiation, $\dot{Q}_s$;

6) Internal heat generation (or dissipation) by electrical, chemical or nuclear effects, $\dot{Q}(i)_p$.

The first law of thermodynamics applied to the 'i'th node gives:

$$DEN(i) \cdot V(i) \cdot CP(i) \frac{\Delta T(i)}{\Delta \tau} = RES(i) = \dot{Q}(i)_{IR} + \dot{Q}(i)_{cond} + \dot{Q}(i)_{conv} + \dot{Q}(i)_f + \dot{Q}(i)_s + \dot{Q}(i)_p \tag{4.1}$$

where $RES(i)$, $DEN(i)$, $V(i)$ are the net energy stored, density and volume of the 'i'th node, respectively, and $\Delta\tau$ is the elapsed time increment.

In the following sections, detailed description will be given for the different terms in Equation 4.1.

4.2.4 *Conduction Heat Transfer*

In this section, the conduction heat transfer analysis will be discussed. For two neighboring nodes (i) and (j), exchange heat by conduction across the interface area $A(i,j)$, the heat transfer $\dot{Q}(i)_{cond}$ is given by

$$\dot{Q}(i)_{cond} = \sum_j C(i,j)_{cond} \cdot [T(j) - T(i)] \tag{4.2}$$

where

$$C(i,j)_{cond} = \left(\frac{A(i,j)}{\frac{s(i)}{K(i)} + \frac{s(j)}{K(j)}} \right) \tag{4.3}$$

K is the thermal conductivity, and s is the 'conduction distance between the center of each node and the surface separating the two nodes, i and j' (see Figure 4.3a).

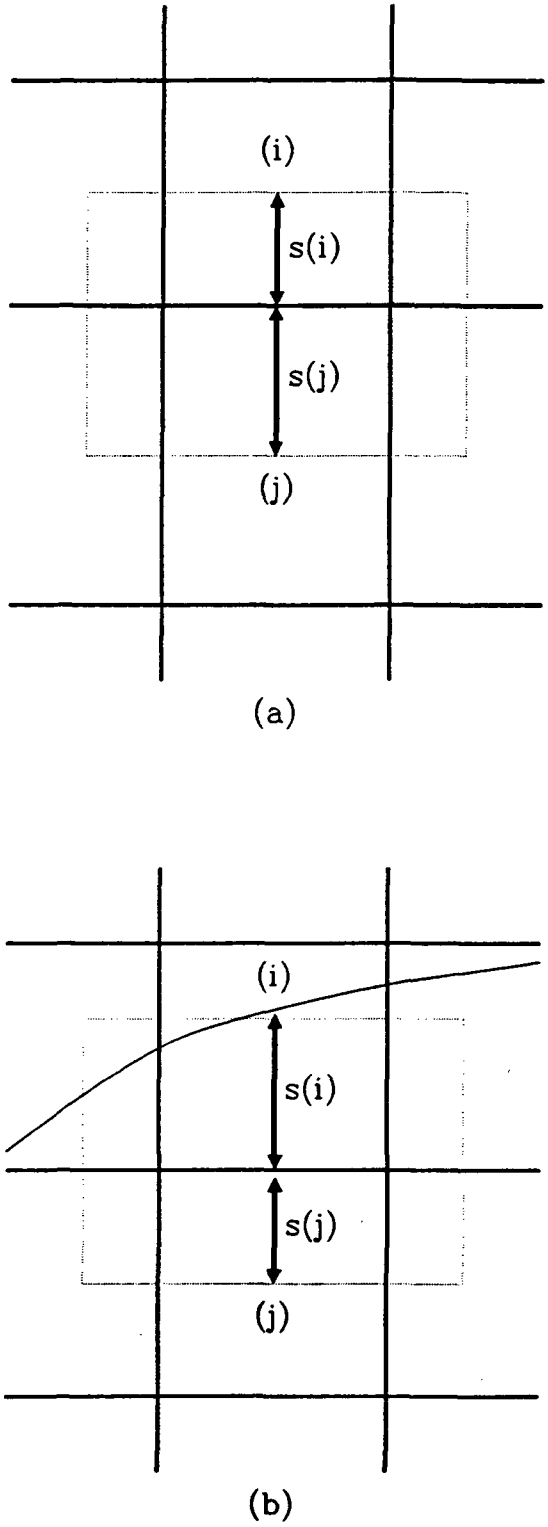

Figure 4.3 (a) Definition of conduction distance, *s* for non-phase-change nodes. (b) Definition of conduction distance, *s* for phase change TES nodes.

Since conduction heat transfer inside the thermal energy storage (TES) material has been identified to be involved in complex phenomena as discussed in Chapter II, the Equation 4.2 simply can not be used between two TES nodes. Hereby, conduction heat transfer inside the TES material is treated seperately in the TES subroutine and the energy balance described in the previous section, is not performed for the TES nodes instead temperature has been set to the fusion temperature of the phase change material. However, conduction heat transfer in the radial direction need to be calculated between phase change material node and either thermal energy storage containment node or gas tube node in order to determine the temperatures of the latter nodes (i.e., TES containment nodes or gas tube nodes) using Equation 4.1 (see Figure 4.4). It should be noted that the distance s used in Equation 4.3 is no longer measured from the center of the node for the TES nodes. Thus, for TES nodes, s is defined as the 'conduction distance between the solid-liquid interface (or fusion front) and the surface seperating the two nodes, i and j' (see Figure 4.3b).

The value of $C(i,j)$ could be a fuction of time and/or temperature or any other variable. However, the conductance $C(i,j)$ is assumed constant and uniform throughout the node.

4.2.5 *Convection Heat Transfer*

The convection heat transfer across the boundary layer of solid-fluid interfaces (working gas tubing), can be put in the following form between two neighboring nodes (i) and (j) of different phase:

$$\dot{Q}(i)_{conv} = \sum_{j} C(i,j)_{conv} \cdot [T(j) - T(i)] \tag{4.4}$$

where the conductance $C(i,j)_{conv}$ is given by:

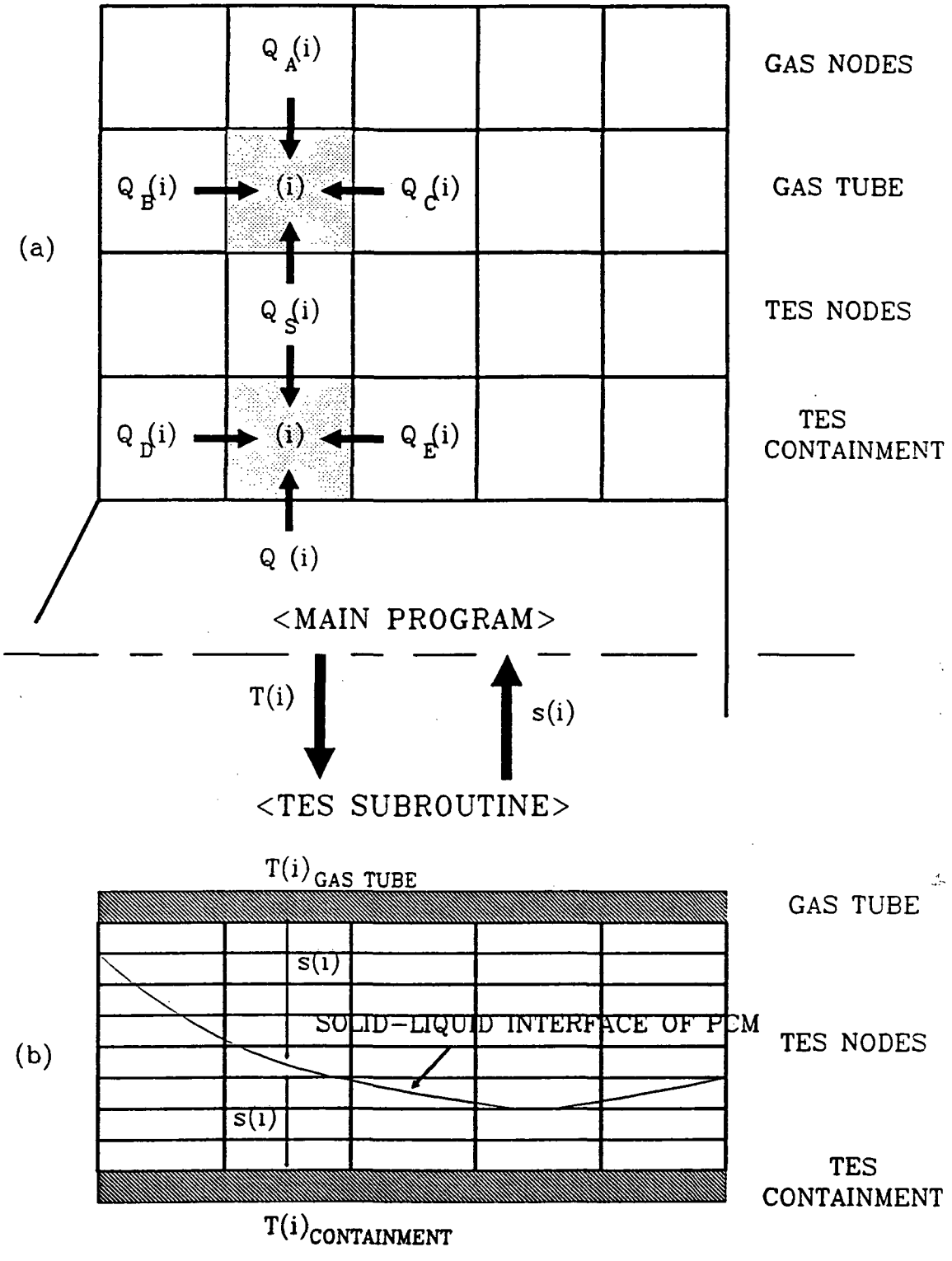

Figure 4.4 Connection of the heat transfer calculation between TES material and Receiver. (a) Energy balance for receiver nodes adjacent to thermal energy storage node. (b) Finite difference nodes for TES calculation.

$$C(i,j)_{conv} = h(i,j) \cdot A(i,j) \tag{4.5}$$

and where $h(i,j)$ is the convective heat transfer coefficient.

$C(i,j)_{conv}$ is treated in a manner that allows its value to be changed with time. This is made simply because the convection coefficient $h(i,j)$ is a dominant function of the fluid mass flow rate which may not be constant during the receiver operation.

4.2.6 *Fluid Convection*

Consider a node (i) surrounded by two adjacent nodes (s) and (k) with a fluid flowing at a rate $\dot{m}_f$ from (s) to (i) to (k) as shown in Figure 4.5. An energy balance on node (i) taking into account the energy entering at $T(s)$ and leaving at $T(i)$ would yield

$$\dot{Q}(i)_f = \dot{m}_f(i) \cdot Cp_f(i) \cdot \left[T(s) - T(i)\right] \tag{4.6}$$

which will be written as

$$\dot{Q}(i)_f = C(i,s)_f \cdot \left[T(s) - T(i)\right] \tag{4.7}$$

or

$$\dot{Q}(i)_f = \sum_j C(i,j)_f \cdot \left[T(j) - T(i)\right] \tag{4.8}$$

where $T(j)$ is the temperature of all neighboring nodes in direct contact with node (i). For a single fluid stream crossing node (i), there will be only two surrounding nodes, one upstream and the other downstream. The flow conductance

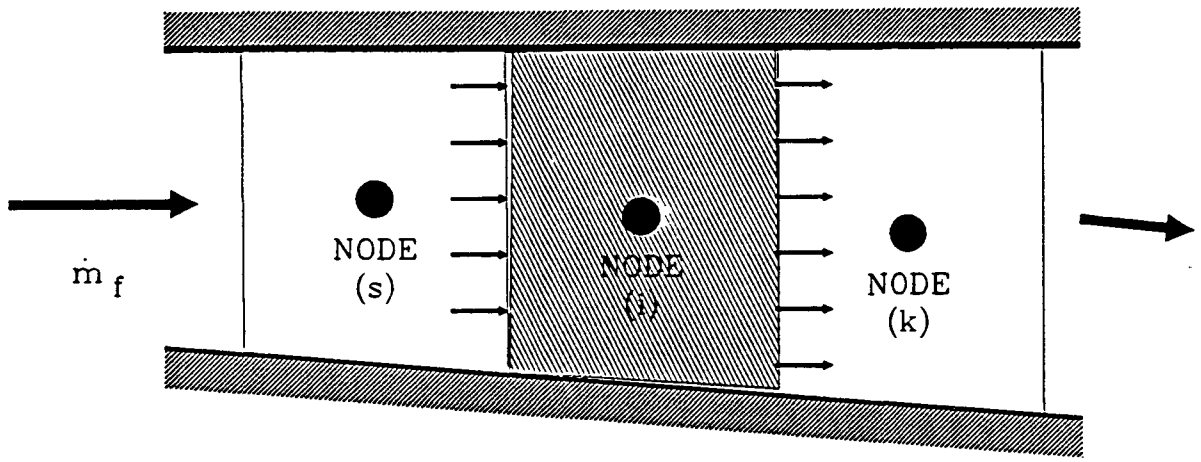

Figure 4.5 Fluid Flow Across Node (i).

$C(i,j)$ will then be taken as $[\dot{m}_f(i)\,Cp_f(i)]$ if the flow goes from (j) to (i), and zero if the frow goes from (i) to (j). The matrix $C(i,j)_f$ will then be asymmetric such that $C(i,j) \neq C(j,i)$ and all elements are needed as input data. For boundary nodes that present the inlet fluid zone or outlet fluid zone as shown in Figure 4.1 the next neighboring node in the closed loop should always be considered.

4.2.7 *Infrared (IR) and Solar Radiation*

The analysids of heat transfer by radiation is divided into two wavelength regions: a) an infrared (or long wavelength) region in which infrared properties apply; and b) solar (or short wavelength) region in which solar radiation properties apply.

The net long wave (infrared) radiation received by the 'i'th node from all neighboring nodes is given by

$$\dot{Q}(i)_{IR} = \sum_j C(i,j)_{IR}\ \left[T^4(j) - T^4(i)\right] \tag{4.9}$$

where T is the absolute temperature and $C(i,j)_{IR}$ is the IR radiation conductance between nodes (i) and (j). From IR radiation analysis, $C(i,j)$ can be written as

$$C(i,j)_{IR} = A(i) \cdot \sigma \cdot \epsilon(i) \cdot \hat{F}(i,j) \cdot \epsilon(k)$$

where σ is the Stefan-Boltzman radiation constant, ϵ is the gray emissivity of the 'i'th node, and $\hat{F}(i,j)$ is sometimes called total view factor since it does include not only the the nodes i and j but also all the neiboughboring nodes. effect of the neiboring nodes as well.

Reflectivity and emmissivity have been refered to as ρ^* and ϵ^* respectively in the solar band as ρ and ϵ respectively in the IR band. Thus the net solar energy exchange on node (i) from all neighboring nodes is given by

$$\dot{Q}(i)_S = \left(\sum_j \epsilon^*(i) \cdot \hat{F}^*(i,j) \cdot \rho(j)^* \cdot Flux(j) + \epsilon^*(i) \cdot Flux(i) \right) \cdot A(i) \quad (4.10)$$

where $Flux(i)$ is the incident solar flux on node (i).

Detailed analysis for the radiation conductance calculation can be found in Lansing (1979).

4.2.8 *Transient Temperature Calculation*

After the elapse of a small time interval $\Delta\tau$, Equation 4.1 gives the slope of temperature array T for each node as an approximation of the temperature derivative using finite difference. The explicit scheme is used and the new nodal temperature $T(i)$ at $(\tau + \Delta\tau)$ is calculated using the old temperature $t(i)$ and all other properties at the old time (τ), i.e.,

$$T(i)^{\tau+\Delta\tau} = T(i)^{\tau} + \frac{\Delta\tau}{M(i)\,Cp(i)} \cdot RES(i)^{\tau} \quad (4.11)$$

where $M(i)$, $Cp(i)$ and $RES(i)$ are the mass, specific heat and energy residue at the ith node.

4.2.9 *Matrix Formats*

To facilitate the manipulation process, Equations 4.2, 4.4, 4.8, and 4.9 are put in matrix or vector forms. Generally,

$$\dot{Q}(i) = \sum_j C(i,j) \left[T^n(j) - T^n(i) \right] \quad (4.12)$$

where n is an exponent that can be either 1 or 4, and $C(i,j)$ is a general form for conductance matrix. Equation 4.12 can be written in the expanded form

$$\dot{Q}(i) = C(i,1)\left[T^n(1) - T^n(i)\right] + C(i,2)\left[T^n(2) - T^n(i)\right] + \cdots$$

or

$$\dot{Q}(i) = C(i,1)T^n(1) + C(i,2)T^n(2) + \cdots - \left[C(i,1) + C(i,2) + c(i,3) + \cdots\right]T^n(i)$$

In the matrix form, Equation 4.12 may also be expressed as

$$\dot{Q}(i) = \begin{pmatrix} C(i,1) & C(i,2) & \ldots & -[C(i,1) + C(i,2) + \cdots] & \ldots \end{pmatrix} \begin{pmatrix} T^n(1) \\ T^n(2) \\ \vdots \\ T^n(i) \\ \vdots \end{pmatrix} \tag{4.13}$$

or

$$\dot{Q}(i) = \sum_j \bar{C}(i,k) \cdot T^n(k)$$

where $[\bar{C}]$ is a modified conductance matrix developed from the original $[C]$ matrix with diagonal elements equal to the negative sum of the corresponding row. Therefore, for all of the receiver nodes (for i = 1, 2, 3, ...), $\dot{Q}(i)$ can be written as the following matrix form:

$$[\dot{Q}] = [\bar{C}] \cdot [T^n]$$

where $[\bar{C}]$ is equal to

$$\begin{bmatrix} -[C(1,2)+C(1,3)+\cdots] & C(1,2) & C(1,3) & \cdots & C(1,i) & \cdots \\ C(2,1) & -[C(2,1)+C(2,3)+\cdots] & C(2,3) & \cdots & C(2,i) & \cdots \\ C(3,1) & C(3,2) & -[C(3,1)+C(3,2)+\cdots] & \cdots & C(3,i) & \cdots \\ \vdots & \vdots & \vdots & \ddots & \vdots & \ddots \\ C(i,1) & C(i,2) & C(i,3) & \cdots & -[C(i,1)+C(i,2)+\cdots] & \cdots \\ \vdots & \vdots & \vdots & \ddots & \vdots & \ddots \end{bmatrix}$$

Based on the above discussion, Equations 4.2, 4.4, 4.8, and 4.9 can be written in terms of the modified conductance matrices as

$$\left.\begin{aligned} \dot{Q}(i)_{IR} &= \sum_j \bar{C}(i,j)_{IR} \cdot T^4(j) \\ \dot{Q}(i)_{cond} &= \sum_j \bar{C}(i,j)_{cond} \cdot T(j) \\ \dot{Q}(i)_{conv} &= \sum_j \bar{C}(i,j)_{conv} \cdot T(j) \\ \dot{Q}(i)_f &= \sum_j \bar{C}(i,j)_f \cdot T(j) \end{aligned}\right\} \tag{4.14}$$

and the nodal energy balance, Equation 4.1 is written as:

$$\begin{aligned} RES(i) = &\sum_j \bar{C}(i,j)_{IR} \cdot T^4(j) \\ &+ \sum_j \left[\bar{C}(i,j)_{cond} + \bar{C}(i,j)_{conv} + \bar{C}(i,j)_f\right] \cdot T(j) \\ &+ \dot{Q}(i)_s + \dot{Q}(i)_p \end{aligned} \tag{4.15}$$

4.3 Receiver Orbital Simulation with Thermal Energy Storage

4.3.1 *Incorporation of TES Analysis into the HEAP Program*

Phase change thermal energy storage analysis of the Chapter II has been incorporated into the HEAP program as a subroutine. In Figure 4.4.a, energy

balance for a particular receiver node is depicted in accordance with Equation 4.1 and for the calculation of the receiver node temperature in main HEAP program, the radial TES nodes from $j = 1$ to N in each column of Figure 4.4b is represented by one node whose temperature is set to the fusion temperature.

Connection of the heat transfer calculation between TES material and Receiver is made by the following algorithm for node (i) (see Figure 4.4):

- Step 1.) With the initial or previous interface location, thermal conductance between the nodes (i) and (j) is determined from Equation 4.2 and further $Q_{t,cond}$ is determined. (in HEAP program)
- Step 2.) With the $Q_{t,cond}$ and othe modes of heat transfer to node i, energy residue is calculated from the Equation 4.1 and further new temperature for the receiver node (i) is obtained. (in HEAP program)
- Step 3.) After evaluating new temperatures of all the receiver nodes, phase change problem is solved for TES nodes (Figure 4.4.b) using new receiver temperature as boundary condition. (in TES subroutine)
- Step 4.) After evaluating new locations of the interface for all nodes, repeat step 1 to 3 for next time step.
- Step 5.) At the completion of the whole cycle (sun + shade time) steps 1 to 4 are repeated until steady cyclic operation take place. (About 4 cycles are needed to reach this conditions)

4.3.2 *Results of Orbital Simulation*

Execution has been performed with the practical environmental conditions which simulates the actual orbital condition. Using a computer program called CAV, incident solar flux distribution in an axisymmetrical cavity from a paraboloid concentrator is determined for a given solar intensity. In order to estimate the effects of the thermal energy storage on the temperature of the

various receiver parts, the results with TES and without TES are compared in Figures 4.6 to 4.11.

Figure 4.6 shows the working fluid temperature distribution vs. time at different axial nodes representing inlet, middle and outlet section of the working gas with phase change material (PCM) included. In order to estimate the effect of PCM on the working fluid temperature, similar results to the above is shown in Figure 4.7 with no PCM. Comparing Figures 4.6 and 4.7, the following can be noticed:

1.) The inlet temperatures are almost same
2.) The minimum temperature of the working gas is about 930 °F without PCM and is increased about 10 °F in the presence of PCM.
3.) The maximum temperature of the working gas is about 1300 °F without PCM and is reduced to 1260 °F (40 °F decrease) in the presence of PCM.
4.) The temperature fluctuation during a cycle can be as high as 170 °F without PCM and is reduced to 60 °F due to PCM.

Also, Figure 4.8 shows the temperature distribution of the working gas heat exchanger tubing vs. time at different axial nodes representing the inlet, middle and outlet section of the working gas tube with PCM included. The effect of PCM on the gas tubing temperature can be observed by comparing this figure with Figure 4.9 which shows similar results with no PCM included. Comparing Figures 4.8 and 4.9, the following can be noticed:

1.) The maximum temperature of the gas tubing is about 1380 °F without PCM and is reduced to 1350 °F (30 °F decrease) in the presence of PCM.
2.) The minimum temperature of the gas tubing is about 1050 °F without PCM and is increased to 1150 °F (100 °F increase) due to PCM.
3.) The temperature range can be as high as 230 °F without PCM and is reduced to 95 °F with PCM included.

4.) The maximum temperature range of the gas tubing occurs at gas inlet section as opposed to gas temperature for which maximum temperature occurs at gas outlet section.

Figure 4.10 shows the temperature distribution of the thermal energy storage (TES) containment vs. time at different axial nodes located at the inlet, middle and outlet section of the working gas tube with PCM included. Again, the effect of PCM on the TES containment temperature can be observed by comparing with Figure 4.11 which shows similar results with no PCM included. Comparing Figures 4.10 and 4.11, the following can be noticed:

1.) The maximum temperature of the surface temperature is about 1480 °F without PCM and is increased to 1750 °F (270 °F increase) in the presence of PCM.

2.) The minimum temperature of the gas tubing is about 1080 °F without PCM and is increased to 1409 °F (329 °F increase) due to PCM.

3.) The temperature ranges in the two results are almost same.

4.) The minimum temperature of TES containment has been droped to its limiting temperature which is set purposely equal to fusion temperature of the PCM in order to prevent another solidification near the TES containment.

Solid-liquid interface location vs. time is plotted in Figure 4.12 at four different axial locations, and percent of PCM melted at the middle section of the gas tube is shown in Figure 4.13. From the Figures 4.12 and 4.13, the following can be noticed:

1.) Steady cyclic variation was obtained after first cycle.

2.) At the end of shade time most PCM solidifies, however, only about 60 % melts at the end of sun time.

If change of gas mass flow rate is allowed in overall power system design

requirements, decreasing the working gas mass flow rate during the sun time is suggested in order to increase percent of PCM melted.

Also, two dimensional motion of the interface vs. axial location is shown in Figures 4.14 and 4.15 during sun period and shade period repectively. From these figures, the following can be identified:

1.) The axial distribution of solid/liquid interface resembles that of incident solar flux during the sun time.

2.) The PCM solidifies more rapidly during the shade time than it melts during the sun time.

3.) At the end of shade time, most PCM solidifies completely except the region located at the outlet section of gas tube.

Figure 4.16 shows energy transfered in the receiver vs. time over the cycles. The square symbols represents the accumulated solar energy in and circular and triangular symbols represents the accumulated and dispersed energy extracted by the working gas respectively. The following can be noticed in this figure:

1.) During the sun time constant solar energy is coming in and no energy is coming in during the shade time.

2.) Almost same amount of energy is extracted during sun and shade time.

In Figure 4.17, variation of receiver efficiency vs. time over the cycles is plotted. The receiver efficiency is defined as follows.

$$\eta_{Receiver} = \frac{\text{Accumulated Energy Extracted by Working Gas}}{\text{Accumulated Solar Energy In}} \qquad (4.16)$$

From this figure receiver efficiency is approaching about 90 %, and it is increasing during the shade time since no energy is coming in and energy is still extracted by gas from thermal energy storage.

Table IV shows a summary of temperature variations of the receiver components shown in Figures 4.6 to 4.11 in order to elucidate the comparison between the TES receiver results and the one without TES. The results without TES was obtained by replacing the thermal properties of the PCM nodes by the properties of TES containment to maintain the same area of heat transfer toward the working gas tubing. Therefore one can consider the case without TES as the case with sensible heat storage where storage material has the same thermal properties as TES containment.

Since the design objective for the thermal energy storage is to minimize time variation in working fluid outlet temperature by providing continuous heat into the working gas during the shade time, gas outlet temperature was reviewed first. It has been obserbed that using phase change material as a thermal energy storage reduces cyclic variation of the working gas outlet temperature down to 60 °F which is about 65 % reduction from the result obtained in the case without TES (170 °F). Consequently, the adventage of latent heat storage system over sensible heat storage system discussed in Chapter I can be verified by obtaining less temperature variation of the working fluid. However it is observed that almost same time averaged temperature was obtained in both cases.

Similarly, the maximum temperature variation of the TES working gas heat exchanger tubing has been reduced about 95 °F which is 50 % reduction from the result obtained in the case without TES (230 °F). Maximum temperatures of the gas and gas tubing is higher when no TES are used. On the contrary, for the TES containment, one can observe reversed behavior. The overall temperature of the cavity surface temperature for the phase change TES case is higher than that without TES case. This is due to the large heat capacity and higher thermal resistance of the phase change material. While due to the relatively small heat capacity and thermal resistance, heat transfer rate is higher in the case without

Table IV. Comparison of the TES receiver simulation results with the receiver results without TES.

	Gas tube section	Result with phase change thermal energy storage			Result without phase change thermal energy storage		
		min	max	range	min	max	range
Working gas, F	Inlet	940	963	23	930	970	40
	Middle	1080	1135	55	1030	1195	165
	Outlet	1200	1260	60	1130	1300	170
Working gas tube, F	Inlet	1150	1245	95	1050	1280	230
	Middle	1240	1320	80	1160	1390	230
	Outlet	1305	1350	45	1225	1380	155
Cavity surface, F	Inlet	1409	1750	341	1080	1430	350
	Middle	1409	1670	261	1190	1480	290
	Outlet	1409	1570	161	1260	1425	165

TES, resulting lower cavity surface temperature.

4.4 Receiver Terrestrial Simulation with Natural Convection

4.4.1 *Results of Preliminary Natural Convection Analysis*

As mensioned earlier in Chapter III, preliminary NC analysis has been conducted using constant convective heat transfer coefficient from the following formula (Equation 3.1):

$$\mathrm{Nu}_r = \frac{h\,z}{k_f} = 0.11\,\mathrm{Ra}_r^{1/3} \tag{4.17}$$

One of the results for closed Brayton cycle (CBC) solar receiver simulations is presented in this section. Plotted values in Figures 4.18 and 4.19 are the results of steady-state calculation of the sun period.

Figure 4.18 shows temperature distribution of the cavity surface vs. axial nodes. The solid line represents the results with natural convection and dashed line represents the results without natural convection included. These results are obtained by steady-state calulation during the sun period, therefore no transient behavior for shade period has been shown. Due to natural convection lowest TES containment temperature has been dropped about 14 % and highest TES containment temperature has been dropped about 7 %.

Similarly Figure 4.19 shows temperature distribution of the working fluid vs. the axial nodes. The working gas temperature has been dropped about 9 % due to natural convection heat loss to the ambient air and as a result, receiver efficiency has been dropped about 22 %.

Input values for the evaluation of the h value from Equation 4.16 and comparison of the two outputs are tabulated in Table V. It shows the results

of the preliminary study of the free convection effects on the receiver using the convective heat transfer coeffcient value from the Lighthill's emperical formula, Equation 3.1. The values of parameters in Equation 3.1 which is listed in Table Va, are evaluated at the mean temperature of the ambient air and average cavity wall temperature. Resulting output of the receiver simulation are shown in Table Vb, and calculations were made only for steady-state during the sun time. From Table Vb, due to natural convection, gas outlet temperature drops 81 Deg. C, which is about 16 kW of heat is lost through the air constantly during the sun time. Consequently overall cavity surface temperature and receiver efficiency have been droped also as shown in Table Vb.

In the following section detailed description on the application of the enclosure natural convection problem will be presented along with the results.

Table V. Preliminary results of the natural convection analysis.

(a) Input values for the evaluation of h

Parameter	Value
cavity radius (m)	0.546
ambient air temperature (C)	25
average cavity wall temperature (C)	1183
Thermal diffusivity of the air, at 804 K (m^2/s)	137×10^{-6}
kinemetic viscosity of the air, at 804 K (m^2/s)	98.3×10^{-6}
thermal conductivity of the air, at 804 K (W/m k)	60.8×10^{-3}

(b)Comparison of the output with natural convection and the output without natural convection

	With natural convection	Without natural convection
gas outlet temperature (C)	773	854
lowest cavity surface temperature (C)	979	1140
highest cavity surface temperature (C)	1130	1220
receiver efficiency (%)	69	88

4.4.2 *Incorporation of Natural Convection Analysis into the HEAP Program*

In the previous preliminary study, it is identified that certainly natural convection affects the receiver thermal behavior, however, convective heat transfer coefficient used in this analysis is from the analysis of vertical tube without closed upper plate, whereas receiver cavity has the closed upper plate. Therefore different flow analysis is necessary for the receiver cavity geometry in order to obtain more practical results.

It was found that air outside the receiver aperture has little influence on the air flow inside the cavity. Based on that assumption, the receiver cavity can be assumed to be a complete cylindrical enclosure and then the analysis discussed in Chapter III can be applied to the receiver free convection analysis. Utilizing this analysis, following can be achieved:

1.) h will vary with axial direction;

2.) h will be time-dependent throughout the cycle;

3.) h will be calculated from the analysis that properly characterizes the fluid flow inside an enclosure.

Internal natural convection analysis of the Chapter III has been incorporated into the HEAP program as a subroutine. In Figure 4.20, vertically placed receiver is shown and cavity is divided into three regions: boundary layer, mixing and core region as was done in Chapter III. However, some modification has been made to the analysis for receiver application as follows:

(1) The wall region has been removed from the analysis since heat transfer analysis of the cavity wall is taken care by the HEAP program;

(2) The mixing region has been confined to the upper 10 % of the receiver in accordance with the analysis of Clark (1964) and Evans (1968) for constant heat flux boundary condition;

(3) Exponent of the temperature profile in Equation 3.8 has been changed to 2 in accordance with the temperature profile of Karman-Pohlhausen method used by Siegel (1958) in his vertical flat plate free convection analysis.

Connection of the heat transfer calculation between the air inside receiver cavity and the cavity wall is made by the following algorithm for node (i) (Figure 4.20):

- Step 1.) With the initial or previous local convective heat transfer coefficient, thermal conductance between the node (i) and (j) is determined from Equation 4.3 and further $Q_{a,conv}$ is determined. (in HEAP program)
- Step 2.) With the $Q_{a,conv}$ and othe modes of heat transfer to node i, energy residue is calculated from the Equation 4.10 and further new temperature for the Receiver node (i) is obtained. (in HEAP program)
- Step 3.) After evaluating new temperatures of all the receiver nodes, natural convection (NC) analysis is performed for the air nodes using new receiver temperature as boundary condition. (in NC subroutine)
- Step 4.) After evaluating new local convective heat transfer coefficients, repeat step 1 to 3 for next time step.
- Step 5.) At the completion of the whole cycle (sun + shade time) steps 1 to 4 are repeated until steady cyclic operation take place. (About 6 cycles are needed to reach this conditions)

4.3.2 *Results of Terrestrial Simulation*

The temperature variations of the air inside receiver core and mixing region during the cycles are plotted in Figures 4.21 to 4.26 with the wall temperature. Figures 4.21 to 4.25 shows the core temperature distribution of the air vs. time at various axial locations, namely, z/L=.1, .4, .7, .9 and .95. The calaulation starts with air temperature inside the cavity equals to the ambient air outside

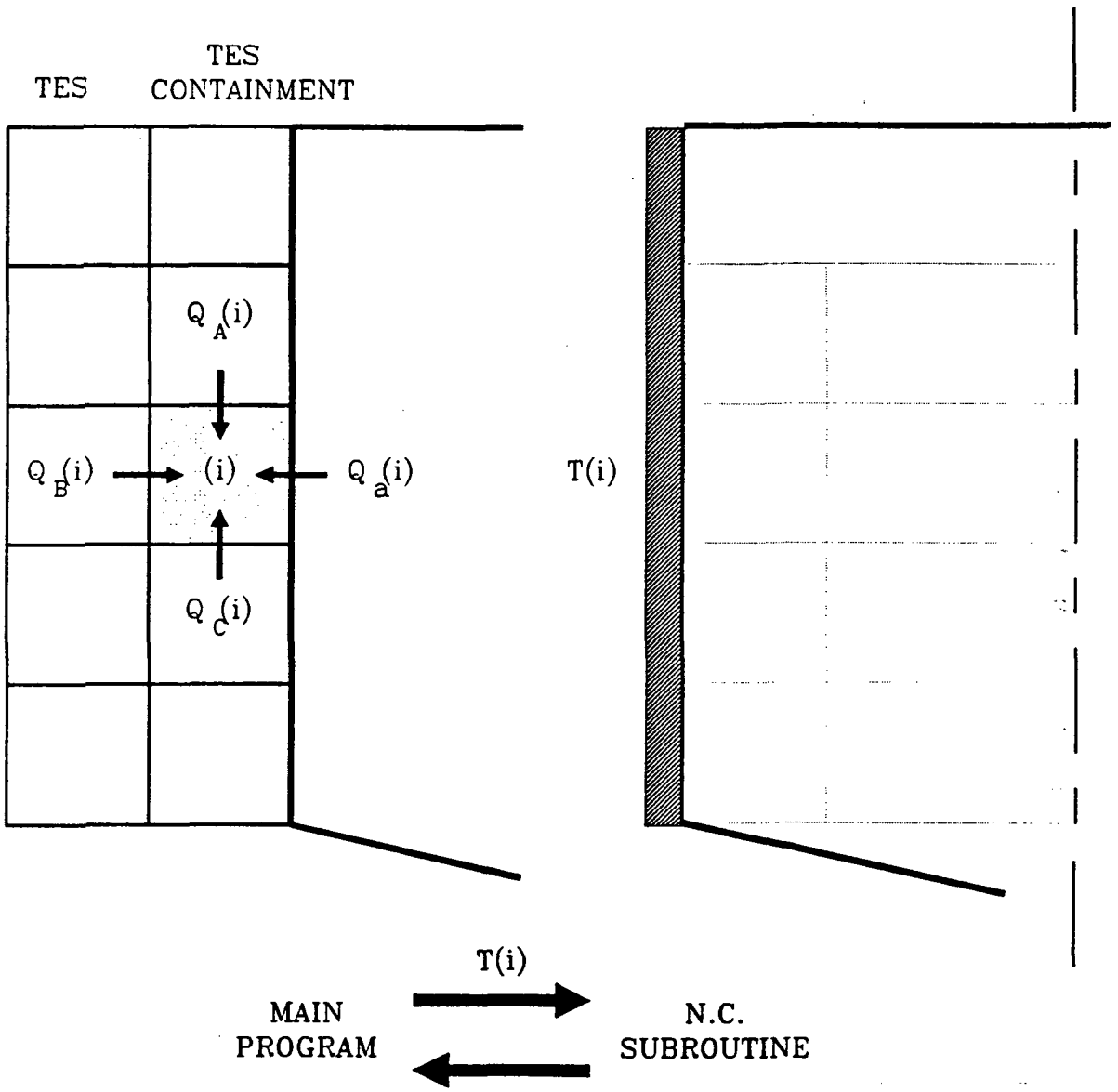

Figure 4.20 Connection of the heat transfer calculation between the air and cavity wall. (a) Energy balance for receiver nodes adjacent to the air node. (b) Finite difference nodes for free convection calculation.

the receiver aperture. Therefore, this is cold start-up simulation of the receiver for the air. From these figures, the following are shown to be noticed:

1.) The core temperature increases rapidly during first and second cycles and shows rather steady variation after fifth cycle.

2.) It is shown that during the shade time the temperature of the core is higher than the average side wall temperature which indicates that the core of the air is not as sensitive to the solar heat flux input as the side wall.

3.) The mixing temperature is almost identical to the average wall temperature.

Figures 4.21 to 4.25 plotted in one graph in Figure 4.26 in order to view the temperature distributions over the entire axial length. From this figure, it is noticed that, as we approach to the bottom of the cavity where aperture is located, maximum temperature over one cycle is dropped and occurs later time, i.e., There is phase lag for the maximum core temperature and is increasing as z decreases, however, the amplitude of the maximum temperature is decreasing.

Also axial variations of the air temperature are shown in Figures 4.27 to 4.29. Figure 4.27 shows the axial variation of the air temperatures during sun time, the solid line represents the temperature distribution at the biginning of the sun time and the following dashed lines are the temperature distributions at 7 minutes after the previous plot time. From this figure, the follow can be noticed:

1.) During the beginning period of sun time, temperatures of upper-half portion of the core increase rapidly but temperatures are still decreasing in lower-core region.

2.) Temperature range between maximum and minimum is much higher in the upper-core than in the lower-core region during the sun time.

3.) Maximum temperature at each time step occurs at the top of the core, and minimum temperature occurs at the bottom of the core except at the beginning of the sun time.

Similarly, Figure 4.28 shows the axial variation of the air temperatures during shade time, the solid line represents the temperature distribution at the biginning of the shade time and the following dashed lines are the temperature distributions at 7 minutes after the previous plot time. From this figure, the follow can be noticed:

the following can be identified from the Figure 4.28:

1.) During the beginning period of shade time, temperature of the upper-core is decreasing, but temperature of the lower-core is still increasing.

2.) Temperature range between maximum and minimum is much higher in the upper-core than in the lower-core region during the shade time.

3.) As opposed to the previous plot during the sun time, maximum temperature at each time step occurs at the middle or the bottom of the core, and minimum temperature occurs at the top.

Figures 4.27 and 4.28 are plotted in one graph in Figure 4.29. In this figure, one can see the sudden temperature drop and sudden temperature rise of the top portion of the core at the beginning of the shade and sun time respectively denoting the sensitivity of the core of the air to the boundary side wall temperature at different axial locations.

Figure 4.30 shows the axial distribution of the local convective heat transfer coefficient vs. axial distance from the receiver aperture during the sun time. The solid line represents the h_z at the beginning of the sun time and the dashed line denotes the h_z at the end of the sun time. The following can be noticed from this figure:

1.) At the beginning of the sun time minimum h_z value is obtained at the middle of the core, however, at the end of the sun time the minimum value is obtained at the bottom of the core.

2.) Range of the h_z values are much higher in the lower portion of the core.

3.) h_z is decreasing during the sun time at all axial locations.

Also, Figure 4.31 shows cyclic variation of the h for three different axial locations, namely, at z/L=.1, .5 and .95. Also, Figure 4.31 shows cyclic variation of the h for different axial locations. In the present study, It was experienced that, during the shade time, $h_z \rightarrow \infty$ due to the very small value of calculated boundary layer thickness. To avoid numerical difficulty, minimum boundary layer thickness has been set to a certain value which results in $h \approx 70$ Btu/hr ft °F which is constant during most shade period.

Similarly, local Nusselt number ditribution is plotted in Figures 4.32 and 4.33. In Figure 4.32 the axial distribution of the Nu_z vs. axial distance from the receiver aperture is shown during the sun time. The solid line represents the Nu_z at the beginning of the sun time and the dashed line denotes the Nu_z at the end of the sun time. The following can be noticed from this figure:

1.) It is shown that almost identical shape is maintained at the beginning of the sun time and at the end of the sun time.

2.) Nu_z increases sharply near the mixing region indicating that more convective heat transfer is occuring at the surface near the top, i.e., the outlet section of the receiver.

Also, Figure 4.33 shows cyclic variation of the Nu for the three different axial locations mentioned in Figure 4.31. Due to the same limitation on the boundary layer thickness, constant limitting values are shown in this plot during most shade period.

In order to estimate the effects of the free convection heat transfer on the temperature of the receiver, the results with natural convection (NC) and without NC are compared in Figures 4.34 to 4.45.

Figure 4.34 shows the temperature variation of the receiver components located at the inlet section of the working gas vs. time with natural convection included. In order to estimate the effect of natural convection on the receiver temperatures at the above locations, similar results to the Figure 4.34 is shown in Figure 4.35 with no natural convection included. Comparing Figures 4.34 and 4.35, the following can be noticed:

1.) During the initial transient start-up cycles, temperatures of the receiver components have been reduced due to convection loss to air inside the cavity.

2.) The temperature of the working gas at this section remained nearly same as the gas temperature obtained from the case without natural convection.

3.) The maximum temperature of TES containment during the last cycle has dropped noticeably due to natural convection heat loss during sun time. Also, the average temperature of the TES containment at this section during the last cycle has dropped due to convection loss during sun time.

4.) During the last cycle, the temperature range of TES containment in this section has dropped about 50 °F due to the presence of the natural convection.

Similarly, Figure 4.36 shows the temperature variation of the receiver components at the middle section of the working gas vs. time with natural convection involved. The effect of natural convection on this section of receiver temperatures can be observed by comparing this figure with Figure 4.37 which shows similar results with no natural convection included. Comparing Figures 4.36 and 4.37, the following can be noticed:

1.) Again, during the initial transient start-up cycles, temperatures of the receiver components have been reduced due to convection loss to air inside the cavity.

2.) The maximum temperatures of the TES containment during the last cycle has dropped due to convection heat loss during the sun time. However, the minimum temperature of TES containment has increased due to heat supply from the air during the shade time.

3.) The average temperatures of the TES containment at this section during the last cycle has increased mainly due to heat supply during the shade time. (The heat supply during the shade time had more effect than the heat loss during the sun time.) While the average temperatures for the other receiver components remained nearly unchanged.

4.) The temperature ranges of these receiver components have been reduced about 27% due to natural convection.

Similarly, Figure 4.38 shows the temperature variation of the receiver components at the outlet section of the working gas vs. time with natural convection included. Again, the effect of natural convection can be observed by comparing this figure with Figure 4.39 which shows similar results with no natural convection included. Comparing Figures 4.38 and 4.39, the following can be noticed:

1.) Again, during the initial transient start-up cycles, temperatures of the receiver components have been reduced due to convection loss to air inside the cavity.

2.) Unlike the other sections, i.e., inlet and middle sections, the maximum temperature of the TES containment during the last cycle at the outlet section remained nearly unchanged. Also, the minimum temperature of TES containment has been increased noticeably due to natural convection.

3.) The average temperature of the TES containment has increased mainly because of the heat supply from the air during the sun time. Due to relatively low maximum temperature of the TES containment, heat supply occurs during more than half of the sun time.

4.) The temperature ranges has been dropped to about 30% due to natural convection.

Solid-liquid interface location vs. time is plotted in Figure 4.40 at three different axial nodes located at the inlet, middle and outlet section of the working gas tube with natural convection. Again, the effect of natural convection on the TES containment temperature can be observed by comparing this figure with Figure 4.41 which shows similar results with no natural convection included. From the Figures 4.40 and 4.41, the following can be noticed:

1.) Due to natural convection, more PCM is in liquid state in the middle and outlet section of the gas tube at the end of shade time.

2.) Due to natural convection, during the sun time, more PCM is melted at the fluid outlet section than the PCM at the middle section.

Also, two dimensional motion of the interface vs. axial distance is shown in Figures 4.42 and 4.43 during sun period and shade period repectively. The effect of natural convection can be observed by comparing these figures with Figure 4.44 and 4.45 which show similar results with no natural convection included. Comparing Figures 4.42 and 4.43 with FIgures 4.44 and 4.45, the following can be noticed:

1.) At the inlet section, less PCM melts, however, more PCM melts at the outlet section of the gas tubing due to natural convection.

2.) The PCM solidifies more rapidly during the shade time than it melts during the sun time.

3.) At the end of shade time, most PCM is still in liquid state except the the fluid inlet section with natural convection included.

Also comparison has been made between the result with natural convection (NC) analysis and without NC analysis and the temperatures of the important receiver components are tabulated in Table VI.

The plots of figures 4.34 to 4.45 are summarized in Table VI to give more elucidatory comparison between the terrestrial and orbital results. Effect of thermal stratification has been detected from this enclosure natural convection analysis even though negative temperature gradient has occured during the shade time. As a result of the effect, the temperature of receiver components at the outlet section of gas tube has been increased rapidly and is maintaining higher average temperature through the cycle than the results obtained from the orbital test which has no natural convection effect (Table VIa).

The most noticeable outcome from this comparison is that the time averaged temperatures of the receiver components during terrestrial test are almost equal to those obtained from orbital test, instead of giving reduced temperature as in the previous preliminary results. From the results obtained, it is found that the existance of the air and resulting free convection does not have considerable effects on the receiver temperature with the receiver in vertical position with aperature pointing downwards.

This is explained as follows by comparing with the preliminary results discussed in previous section. In the preliminary study, the temperature of the core region inside a cavity was considered as ambient temperature or reservoir temperature which is constant all the time, and no variation in core temperature was assumed. As a result, substantial amount of the convective heat is lost continuously and this heat loss causes the overall decrease in in receiver temperature. On the contrary, the core temperature in the detailed study discussed in this

section, was calculated neither same as the ambient temperature nor constant all the time during a cycle. Also, with shade time included, the heat loss during the sun time is balanced with the heat supply from the air during the shade time due to sudden change of the wall temperature which is below the air temperature (see Figure 4.26).

As discussed in Chapter III, the heated fluid near the wall moves upward and mixed together in the upper portion of the cavity and comes down through the core and then the fluid is entrained into the boundary layer again. Since the flow is circulating inside a cavity and has little interaction with the ambient temperature based on the assumption made previously for the aperture opening, incoming solar energy is conserved inside a receiver cavity without any heat loss to the ambient air outside the aperture. Accordingly no continuous convective heat loss is shown from terrestrial free convection results except during warm-up time of the air.

It is worth noting that the range between the minimum temperature and the maximum temperature during a cycle is reduced due to natural convection, and one can see the thermal behavior of the air inside a cavity is very similar to that of energy storage material, i.e., cooling the receiver during sun time (storing the energy) and heating the receiver during shade time (liberating the energy). Therefore one should expect the receiver thermal performance would be worse in the orbit than the terrestrial results with free convection effects which predicts less temperature variation and lower maximum temperature of each component of the receiver which might ignore the material failure due to larger thermal expansion and/or higher maximum temperature than expected during the orbit operation.

Table VI. Comparison of the terrestrial TES receiver simulation *results with the orbital TES receiver simulation results*

(a) Temperatures at three sections during a cycle

	Gas tube section	Terrestrial with natural convection effects				Orbital without natural convection effects			
		min	max	(ave*)	range	min	max	(ave*)	range
Working gas, F	Inlet	950	966	(957)	16	950	969	(959)	19
	Middle	1100	1160	(1132)	50	1100	1170	(1133)	70
	Outlet	1230	1280	(1256)	50	1220	1290	(1253)	70
Working gas tube, F	Inlet	1130	1200	(1160)	70	1130	1210	(1167)	80
	Middle	1240	1300	(1269)	60	1230	1310	(1269)	80
	Outlet	1320	1360	(1338)	40	1310	1360	(1331)	50
TES containment, F	Inlet	1420	1680	(1541)	260	1410	1720	(1553)	310
	Middle	1440	1620	(1521)	180	1410	1660	(1515)	250
	Outlet	1450	1560	(1500)	110	1410	1570	(1473)	160

(b) Percent of the PCM melted at three sections during a cycle

Gas tube section	Terrestrial with natural convection effects				Orbital without natural convection effects			
	min	max	(ave*)	range	min	max	(ave*)	range
Inlet	6.1	43	(24)	36.9	6.1	48	(26)	41.8
Middle	12	53	(34)	40.7	6.1	59	(34)	53.4
Outlet	23	54	(40)	30.7	12	52	(31)	40.2

* Averaged values through the cycle

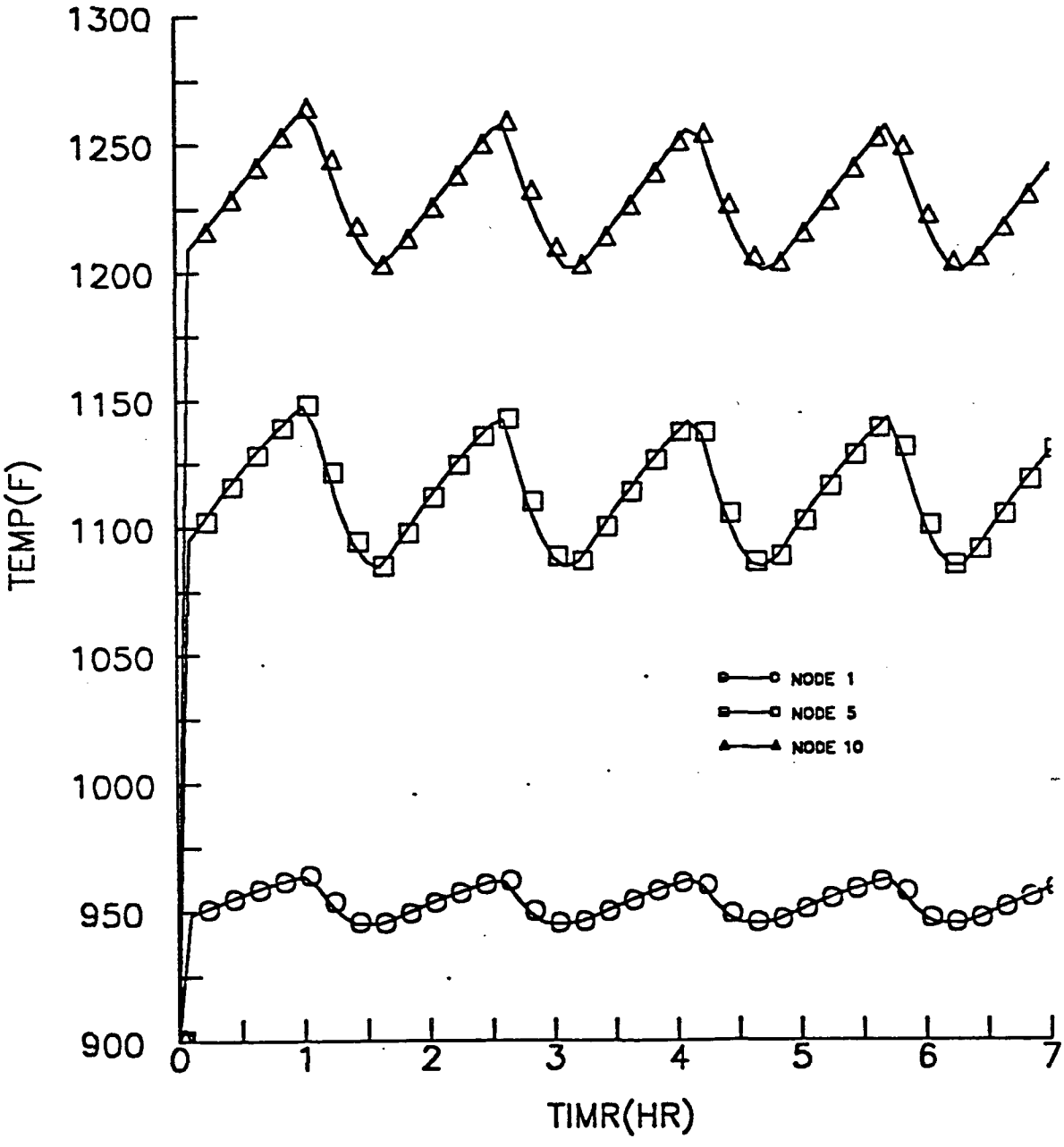

Figure 4.6 Working fluid temperature variation with time at different axial location. (with thermal energy storage)

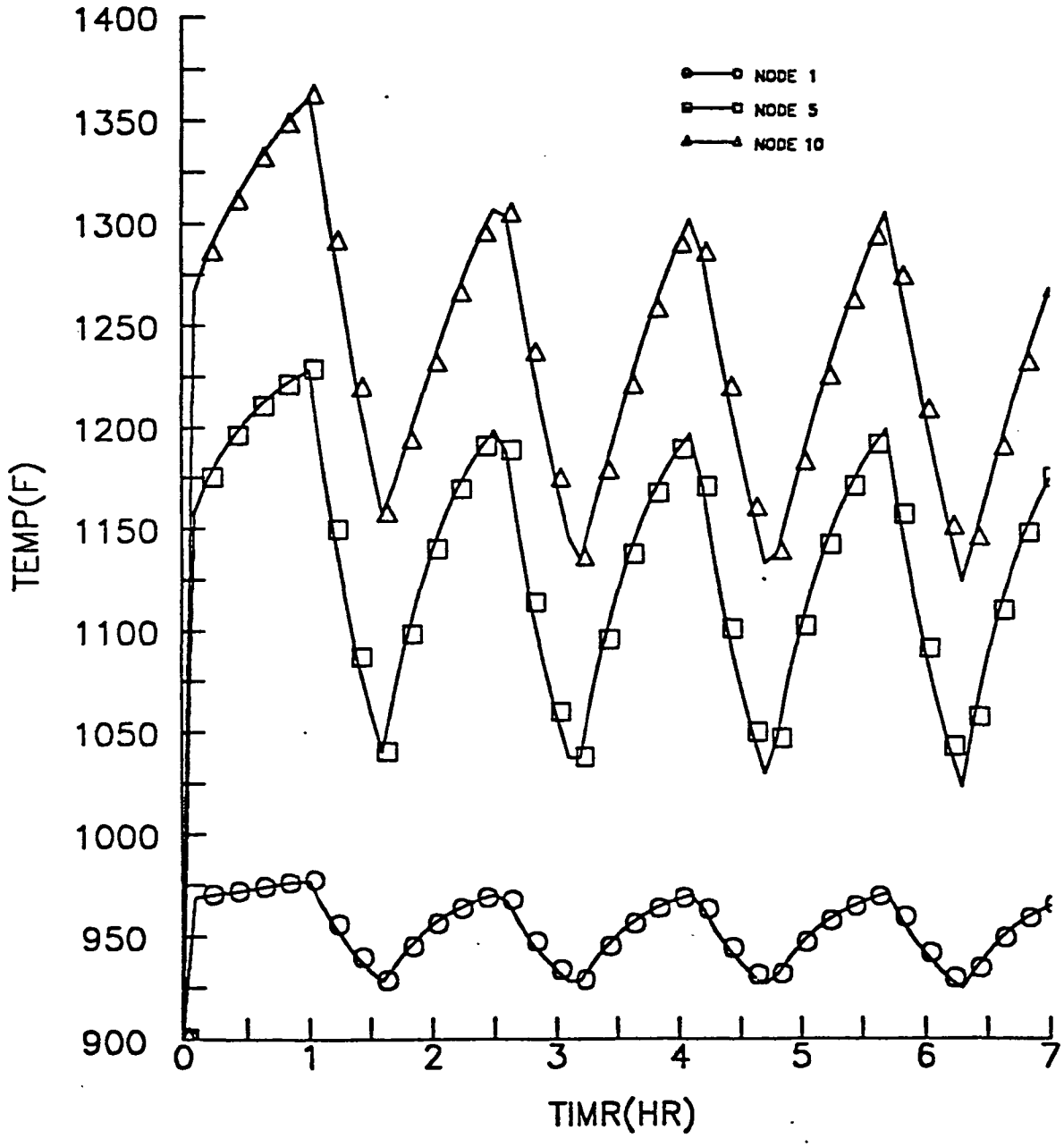

Figure 4.7 Working fluid temperature variation with time at different axial location. (without thermal energy storage)

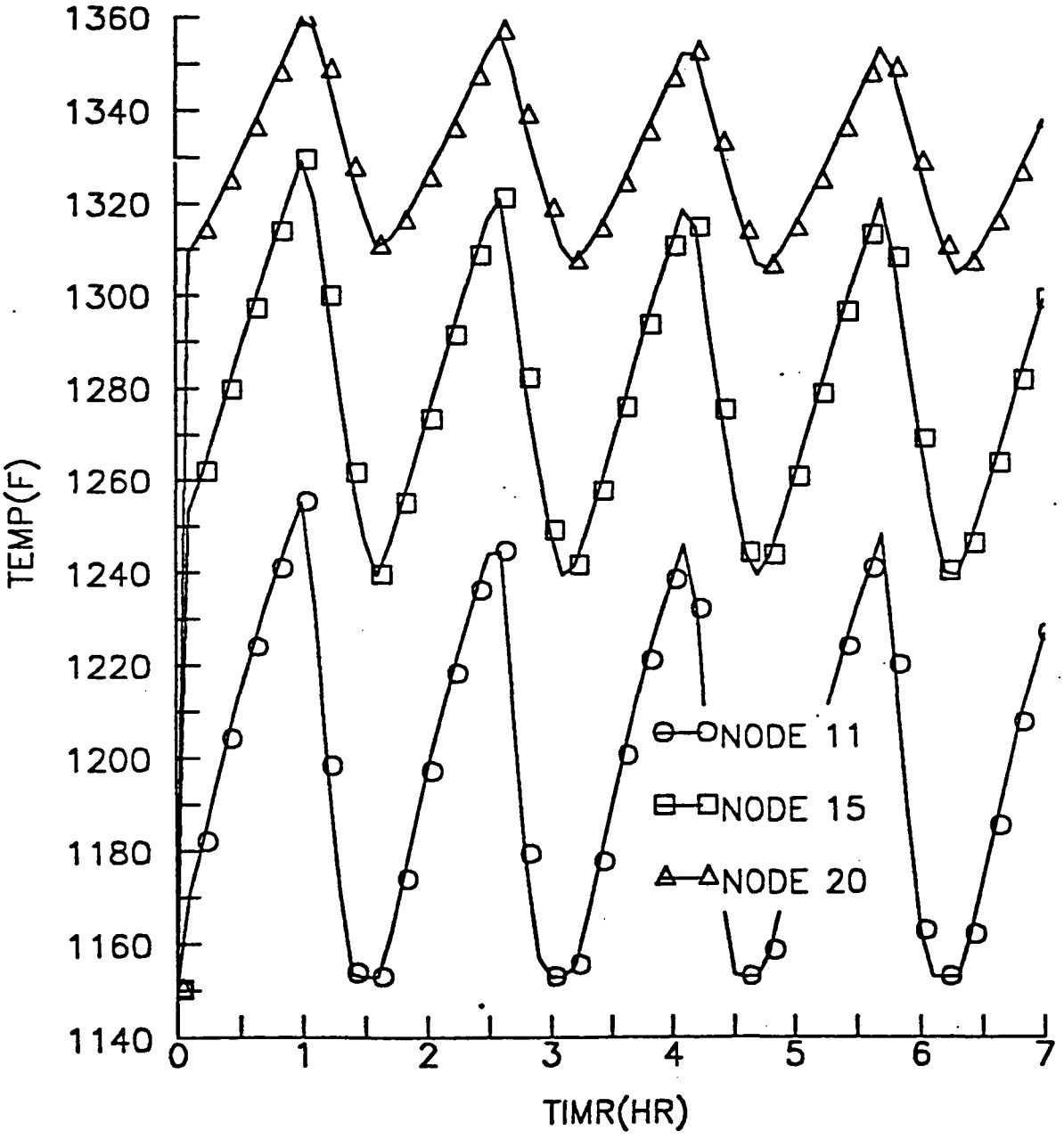

Figure 4.8 The temperature variation of heat exchanger tubing with time at different axial location. (with thermal energy storage)

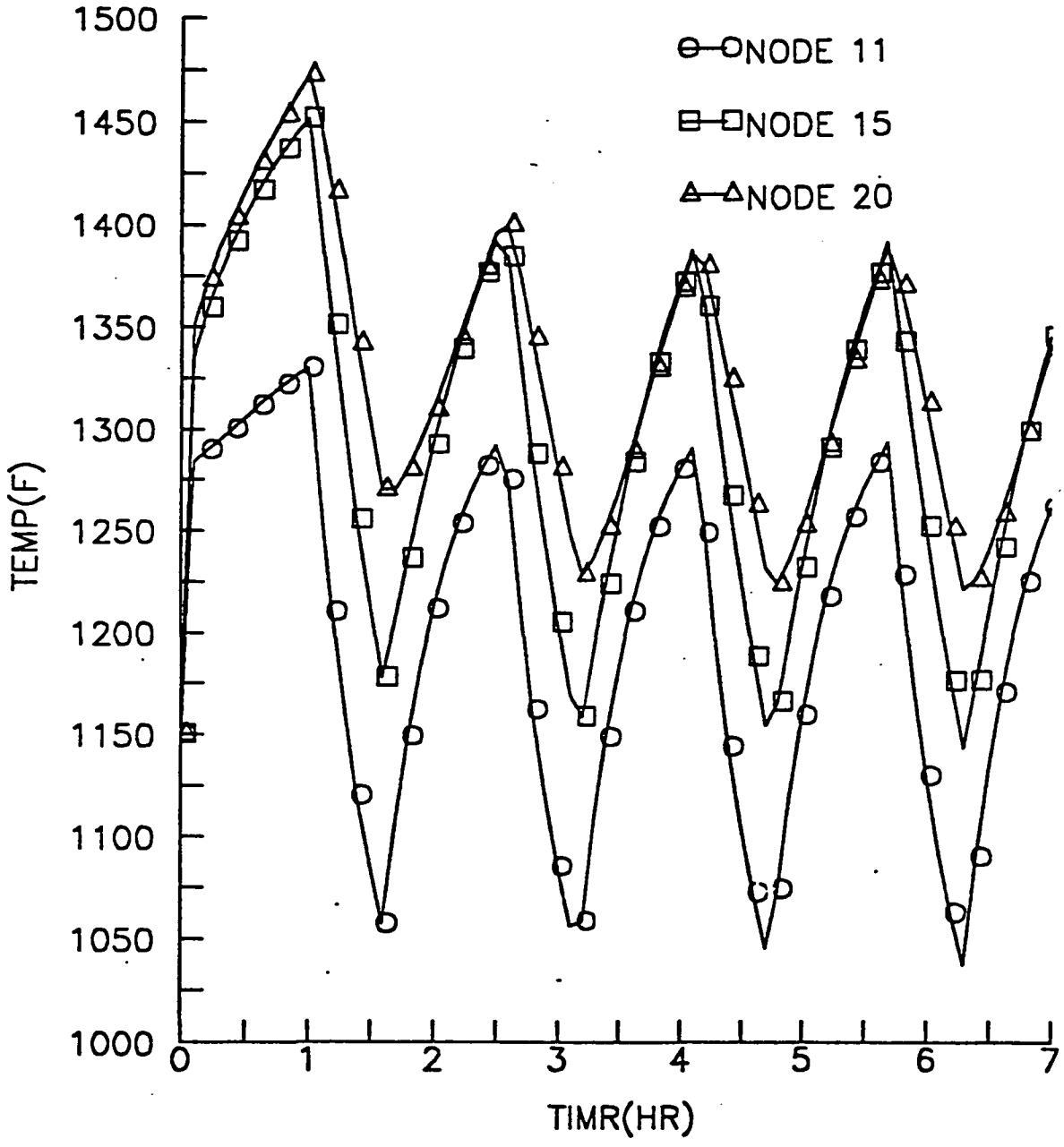

Figure 4.9 The temperature variation of heat exchanger tubing with time at different axial location. (without thermal energy storage)

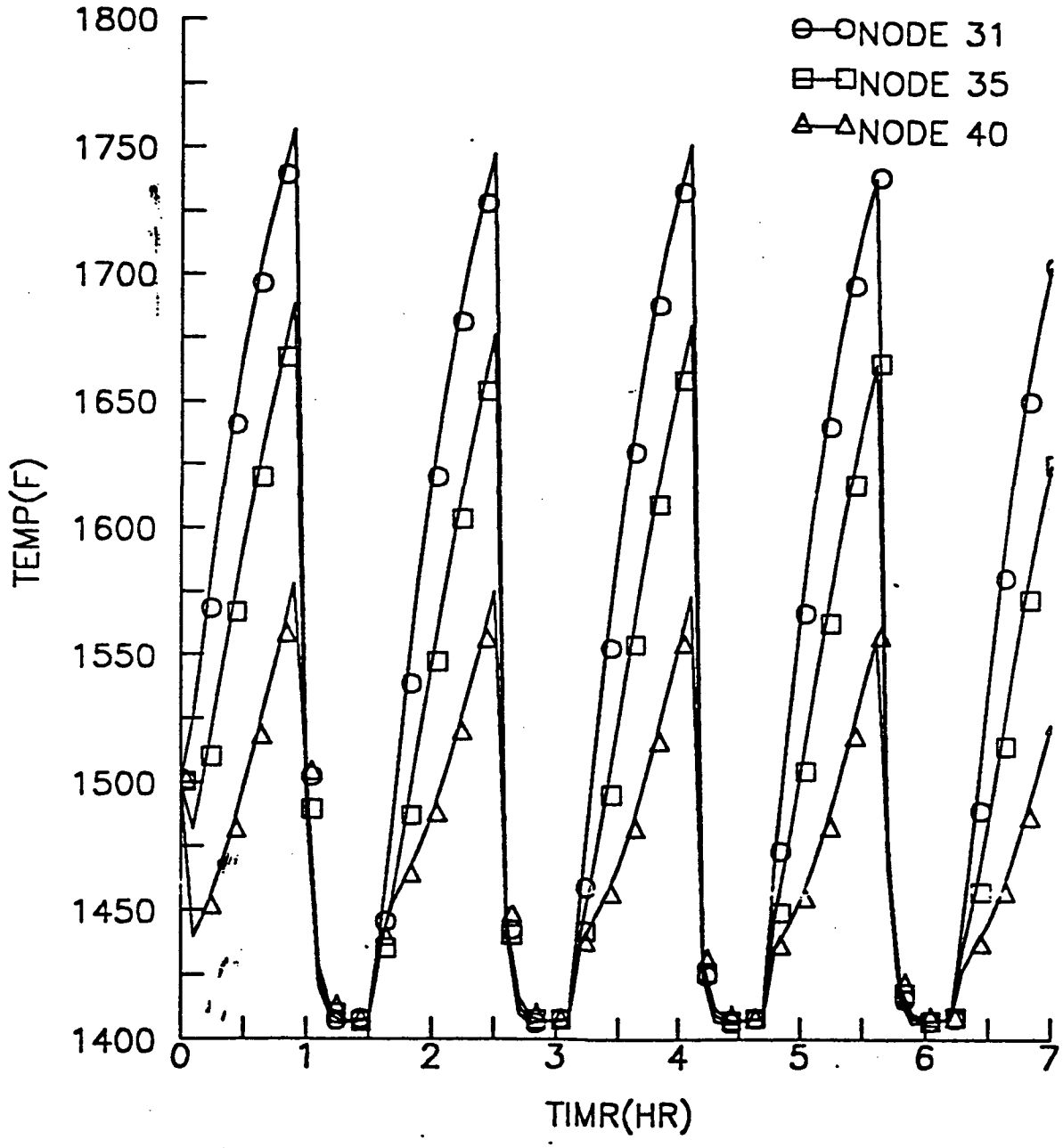

Figure 4.10 The temperature variation of the TES containment with time at different axial location. (with thermal energy storage)

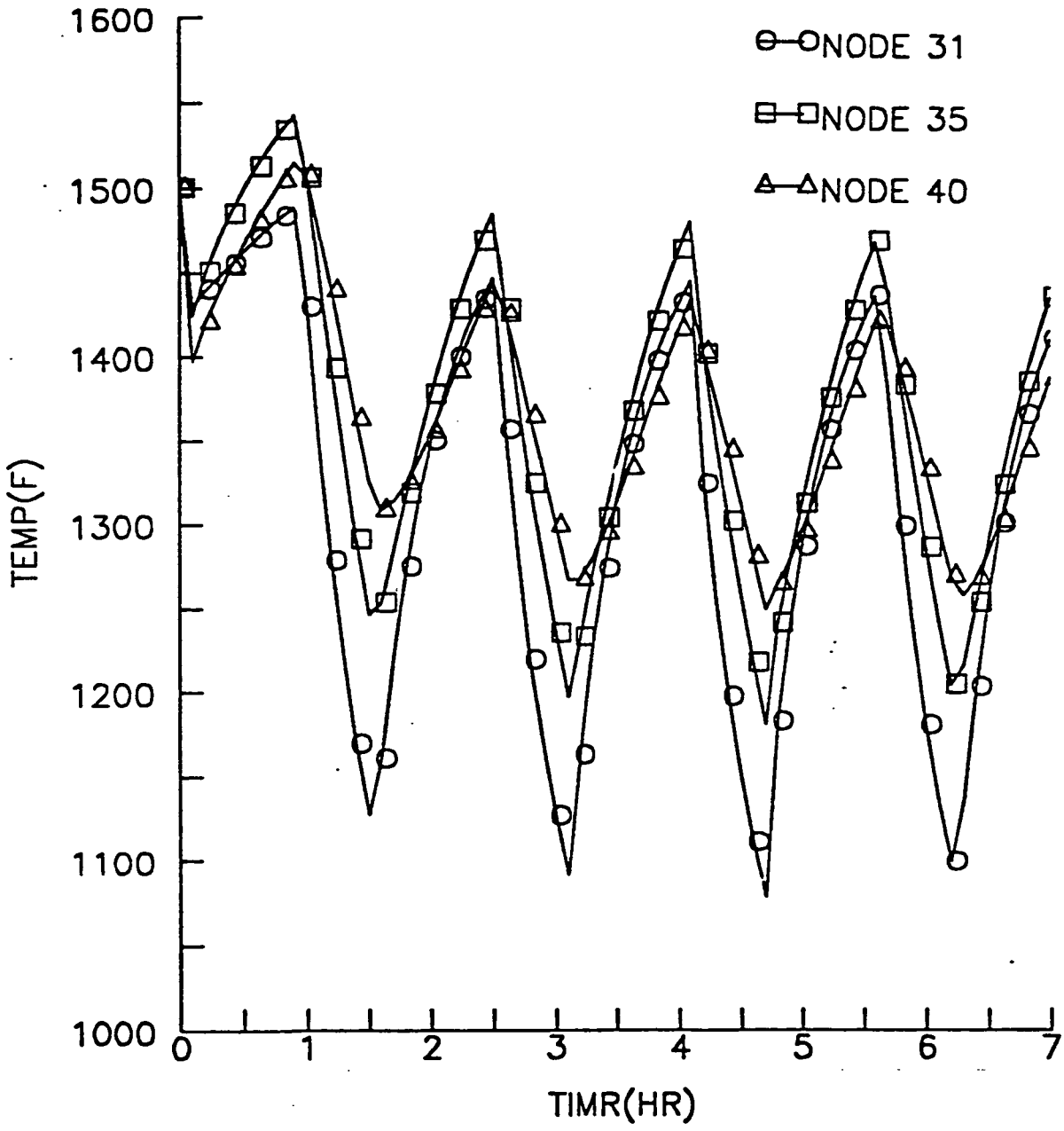

Figure 4.11 The temperature variation of the inside receiver surface with time at different axial location. (without thermal energy storage)

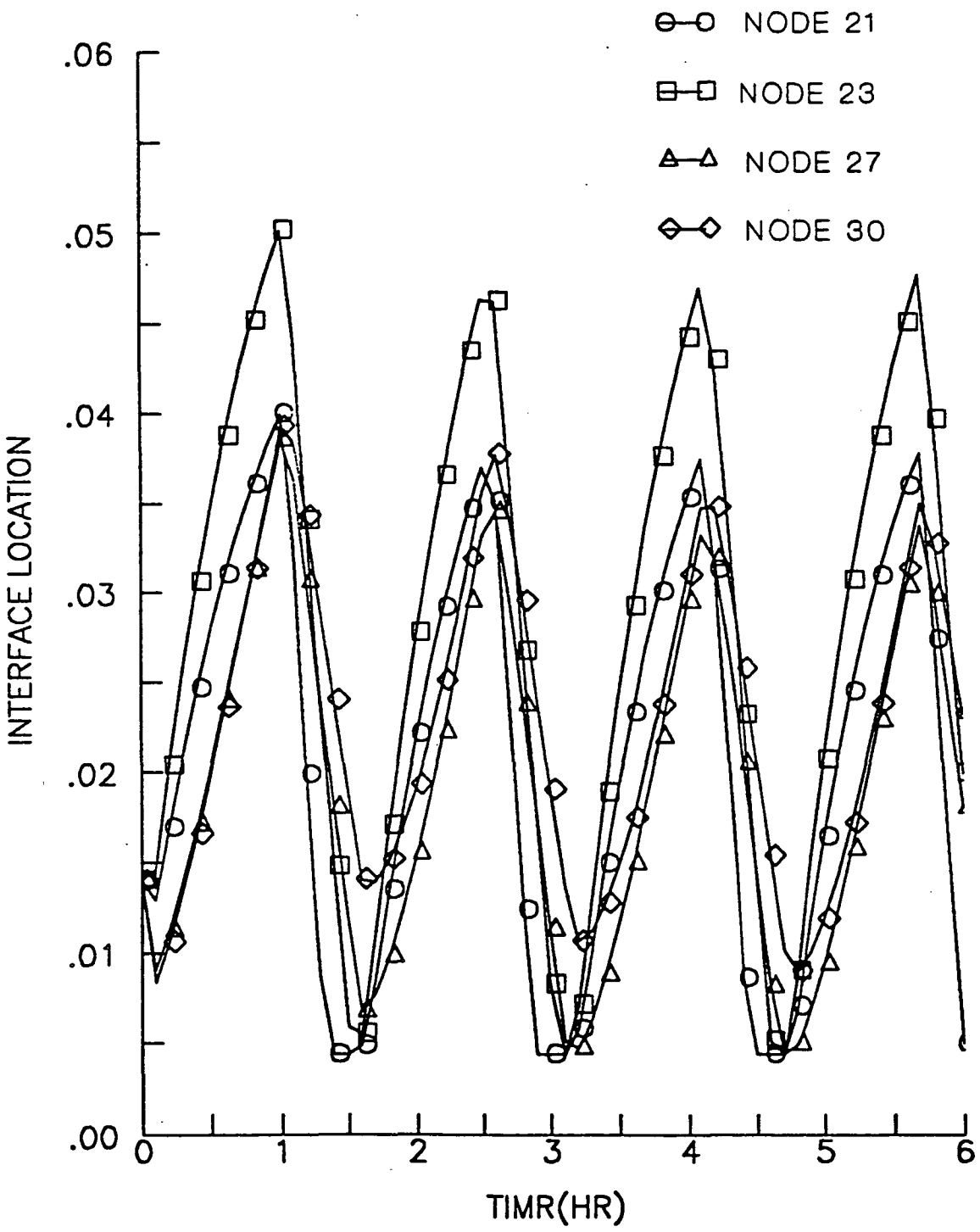

Figure 4.12 Dimensionless interface location as function of time at different axial location.

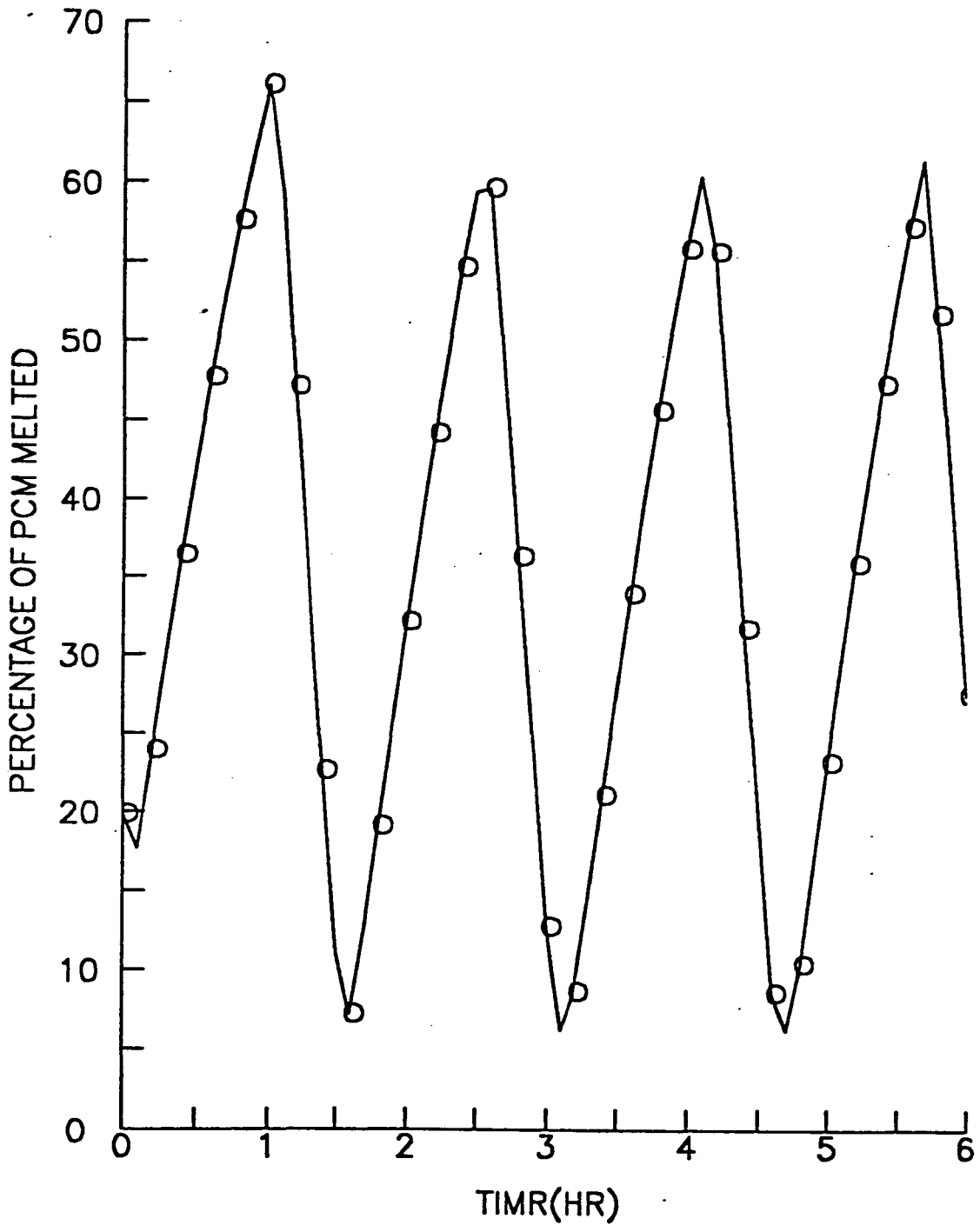

Figure 4.13 The variation of liquid percentage of the thermal energy storage material with time.

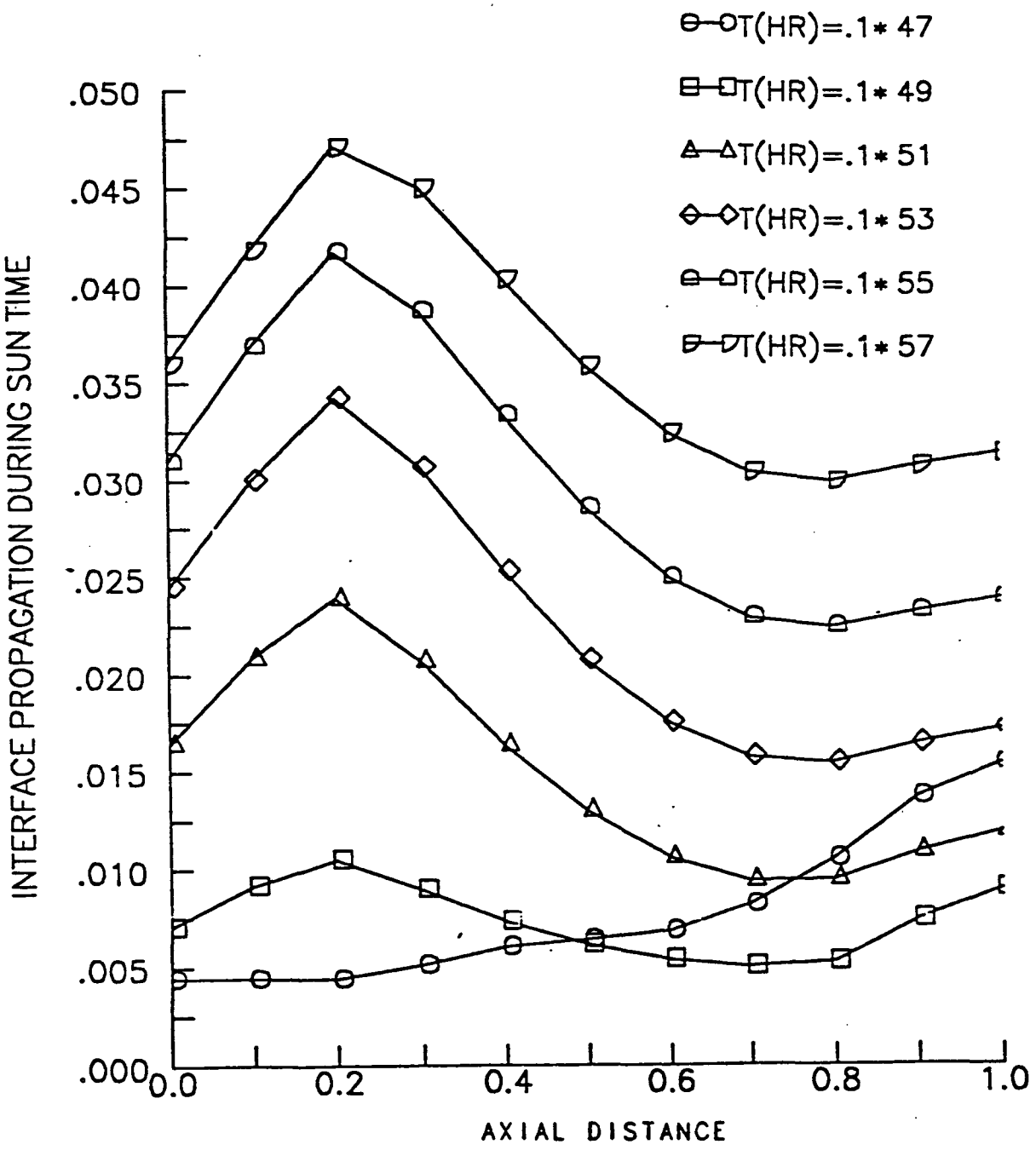

Figure 4.14 Two-dimensional interface motion during sun time for different times.

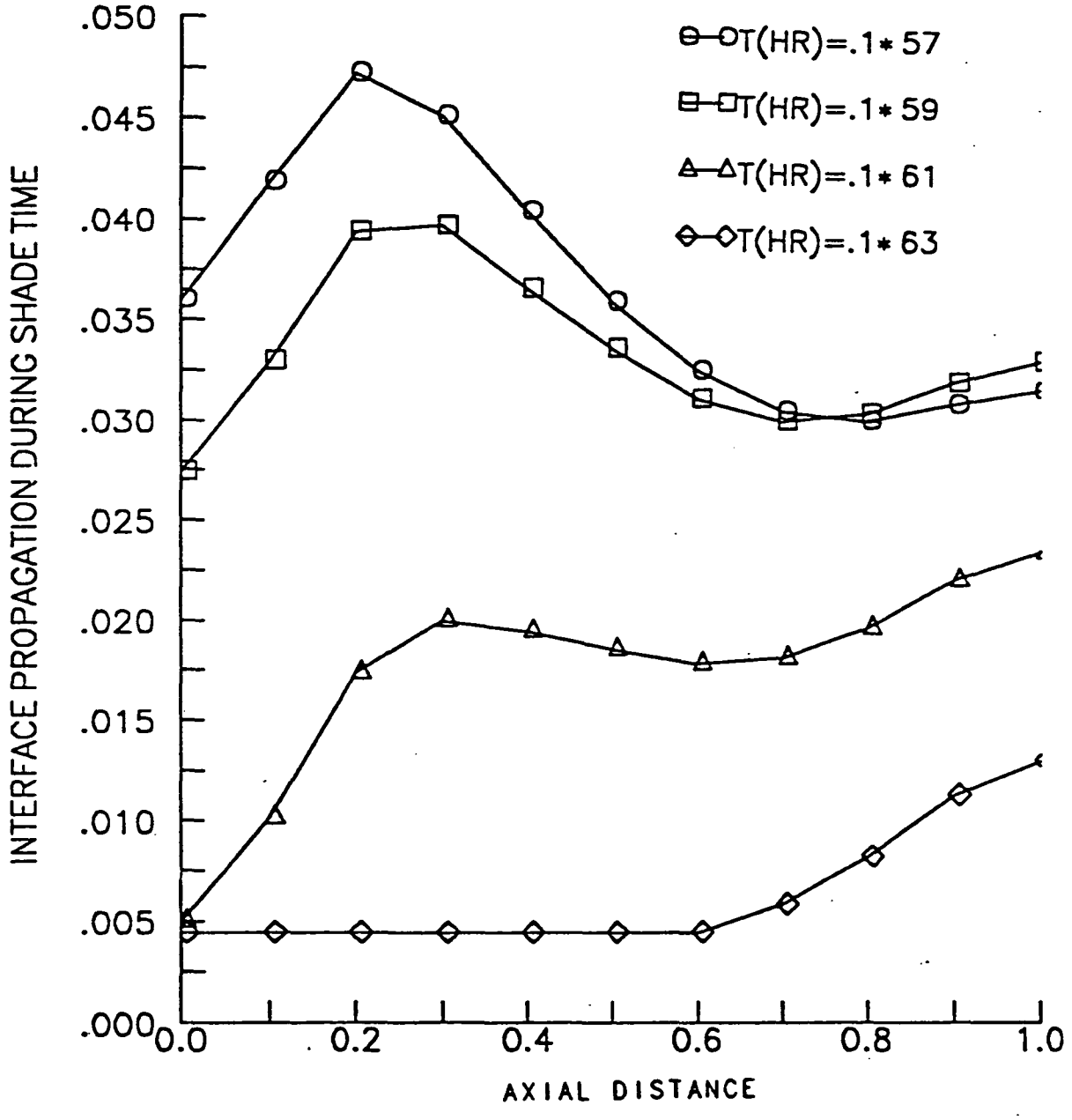

Figure 4.15 Two-dimensional interface motion during shade time for different times.

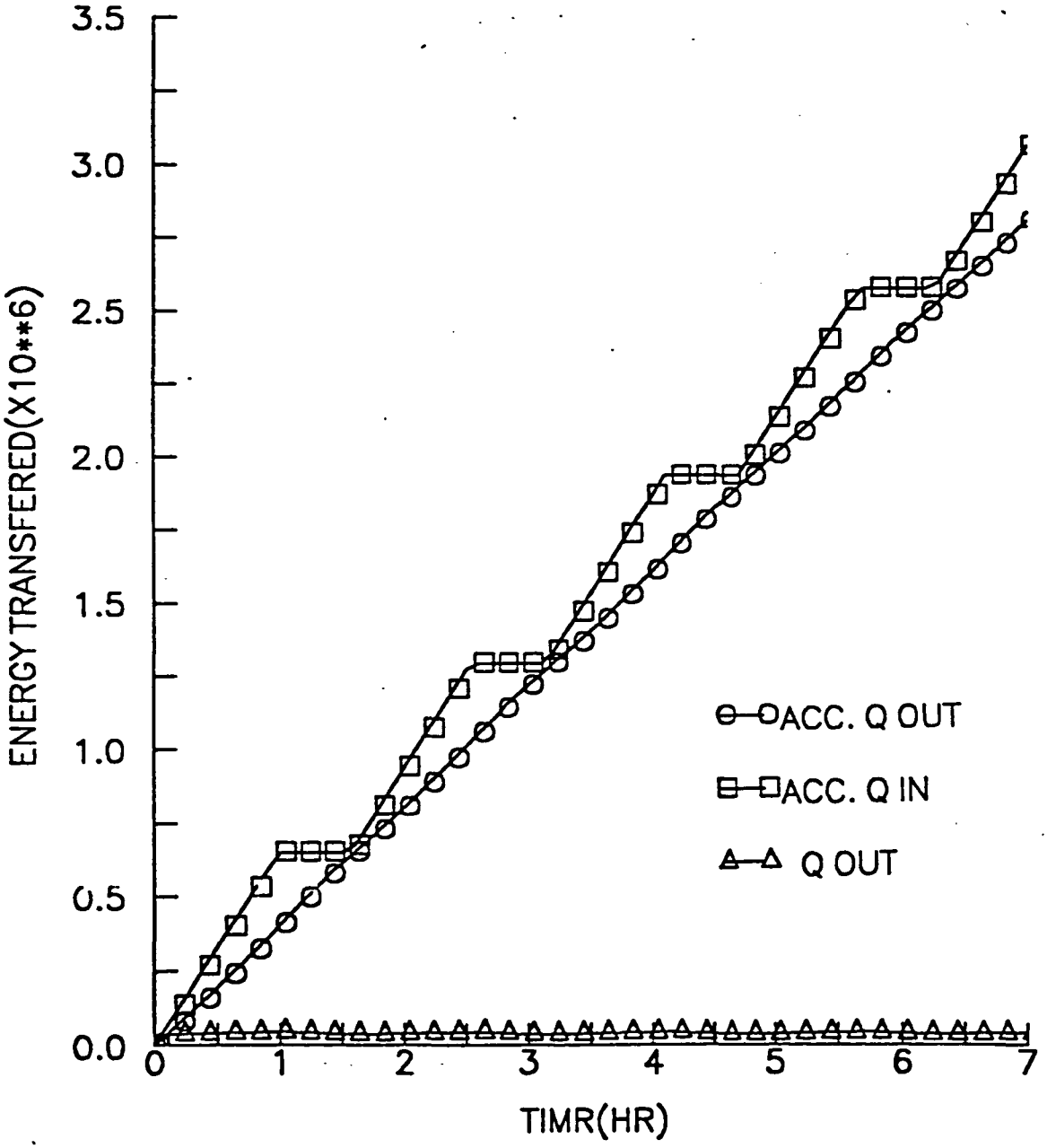

Figure 4.16 Energy transfered in and out of the receiver as a function of time.

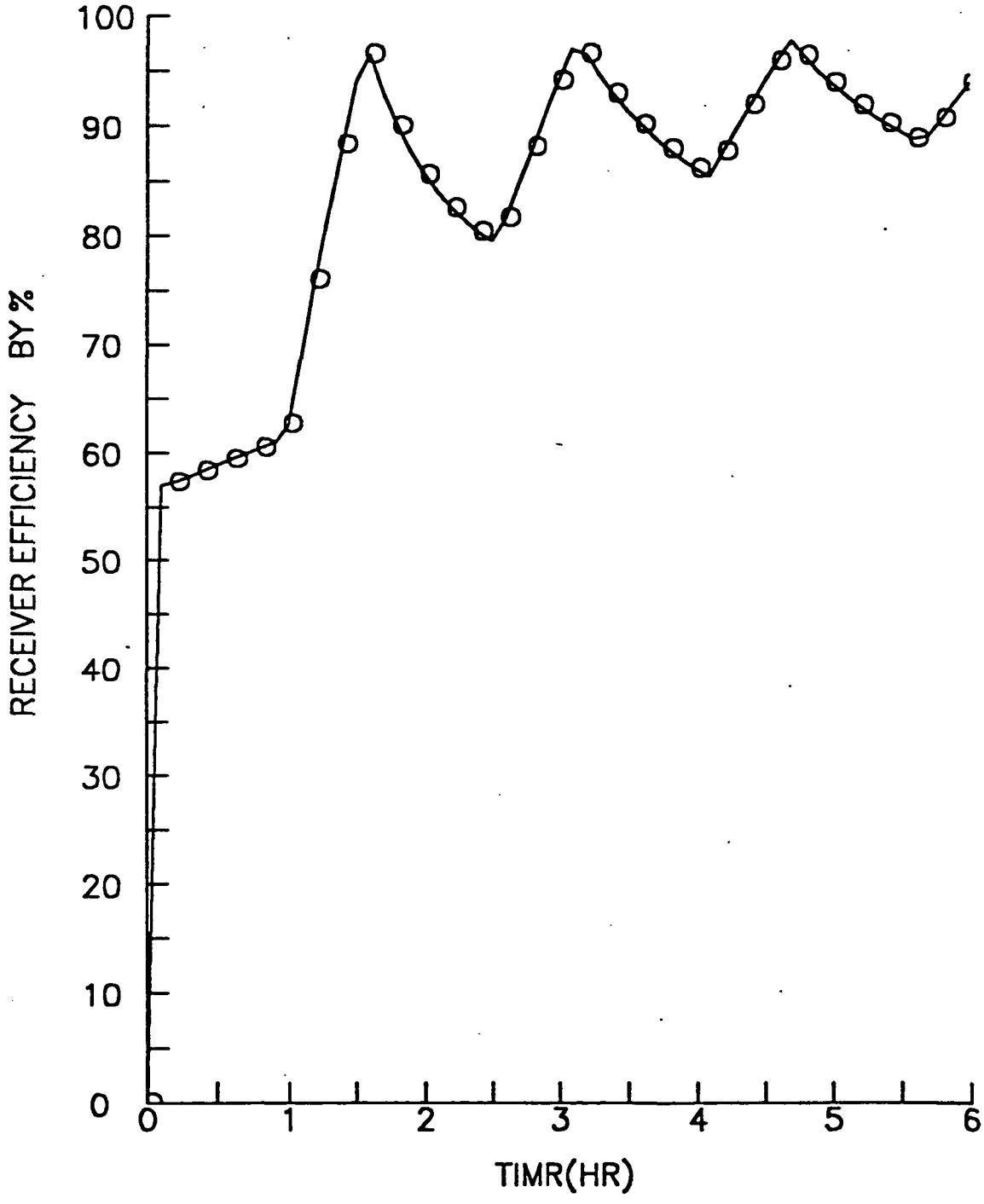

Figure 4.17 Variation of the receiver efficiency with time.

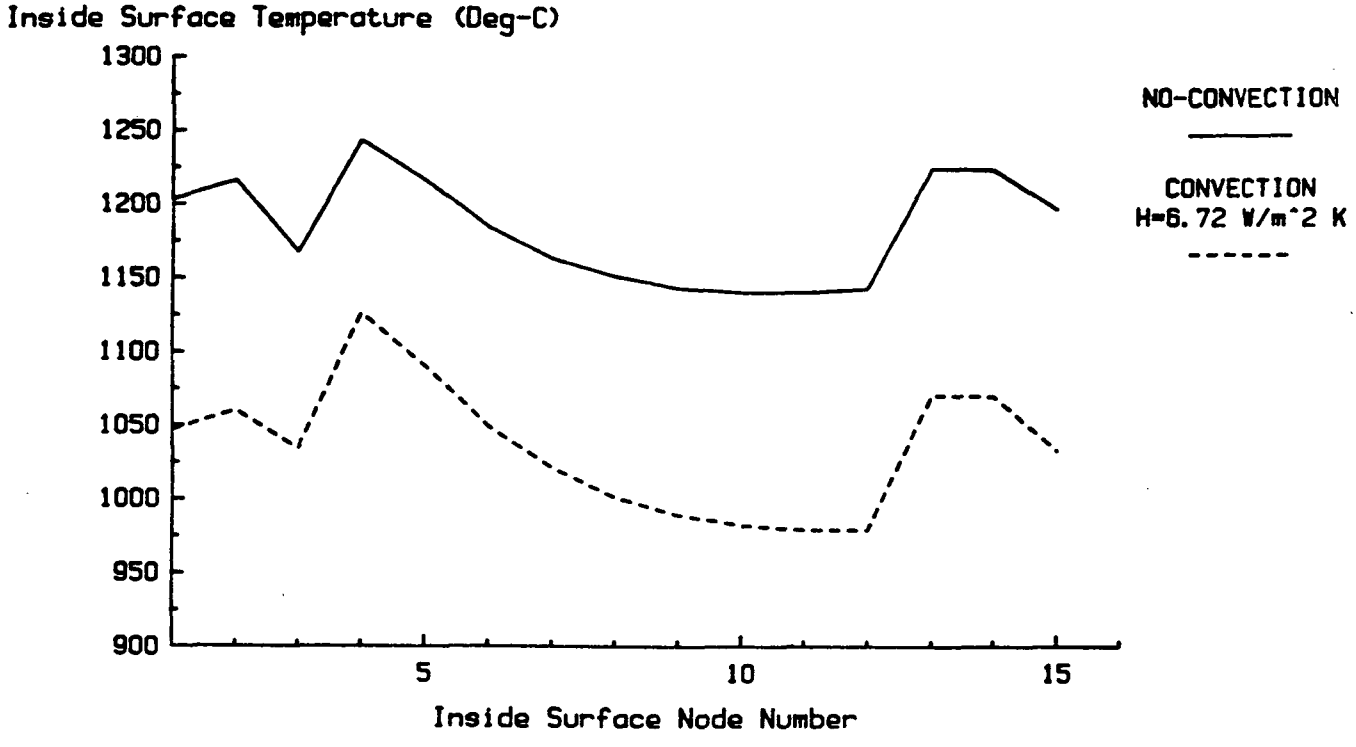

Figure 4.18 Temperature distribution of the cavity surface using $h = 6.86 \quad \mathrm{W/m^2 \cdot K}$.

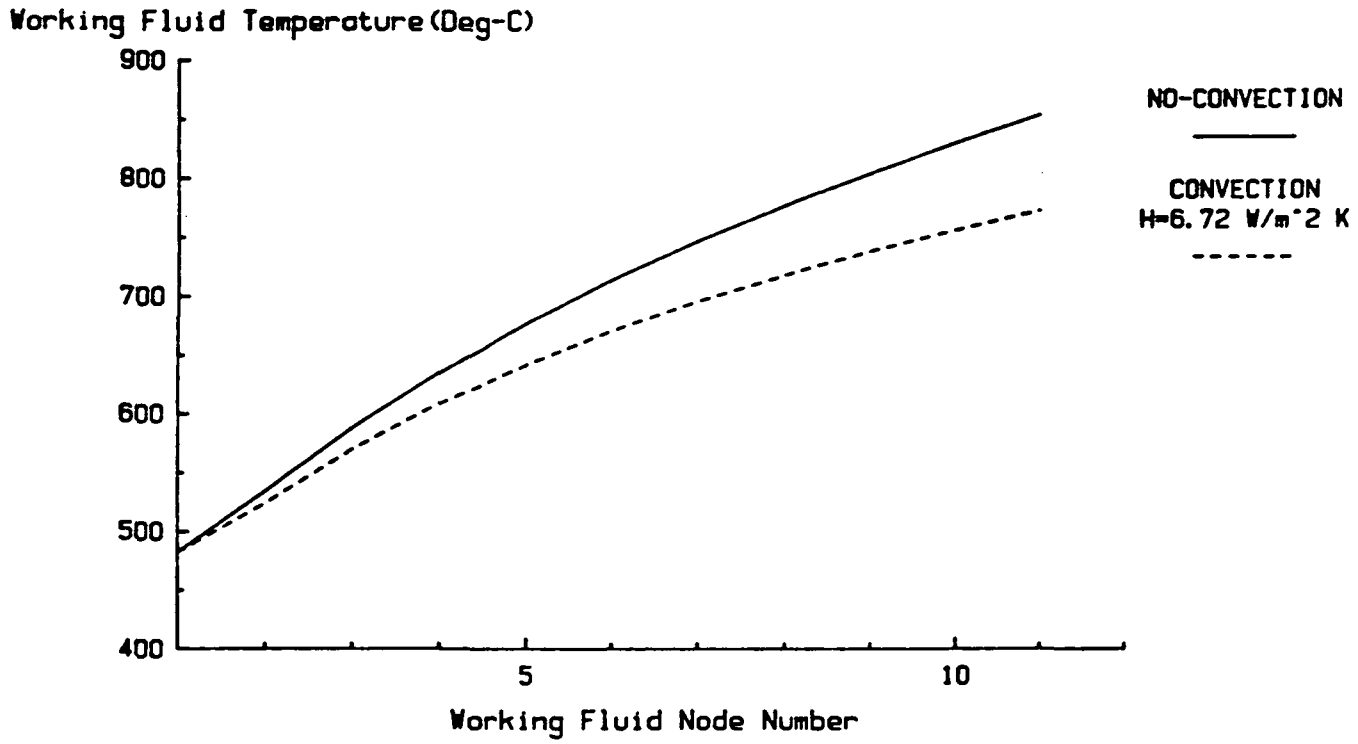

Figure 4.19 Working fluid temperature distribution using $h = 6.86 \ \mathrm{W/m^2 \cdot K}$.

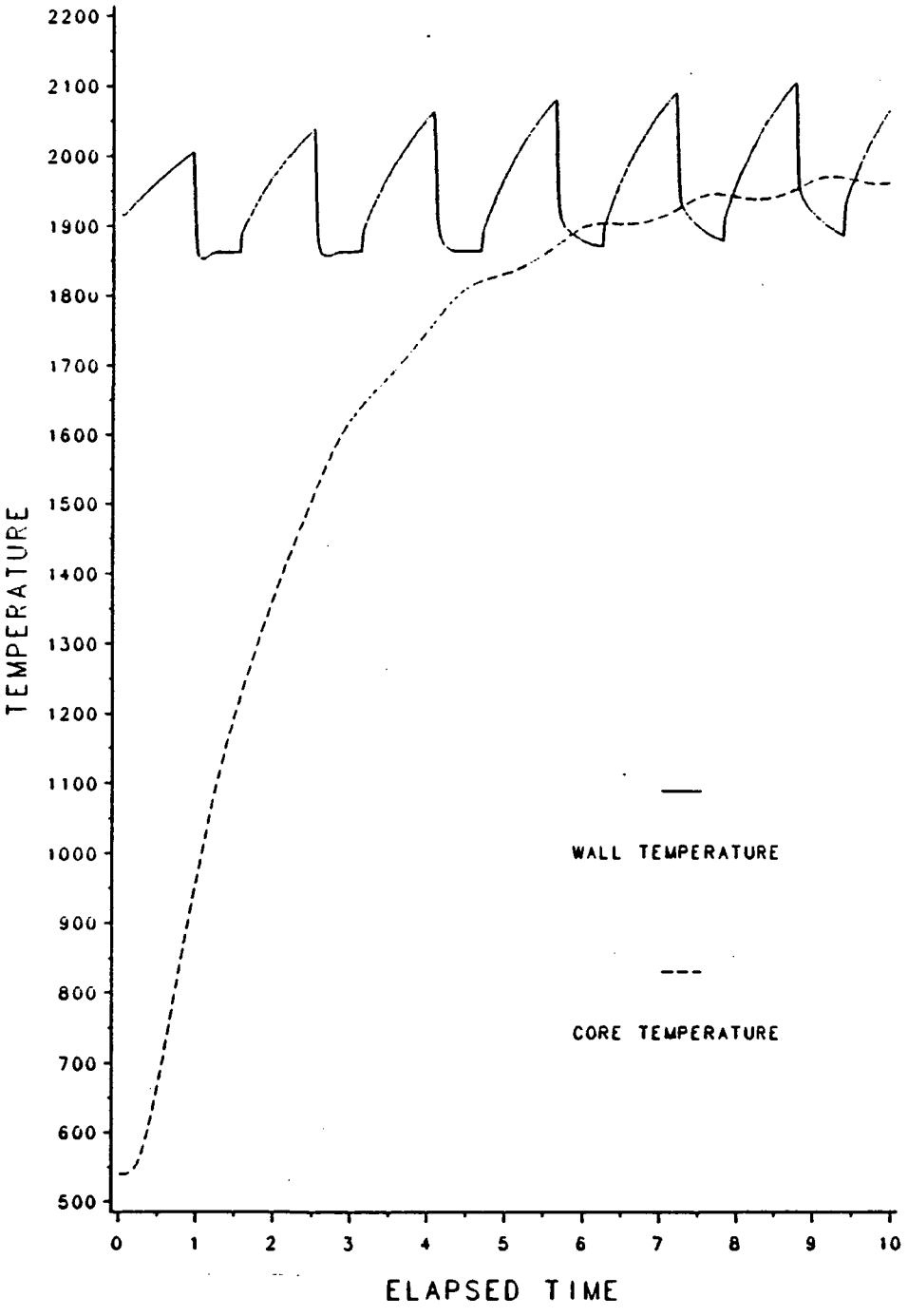

Figure 4.21 The core temperature variations of the air with time at z/L=0.1.

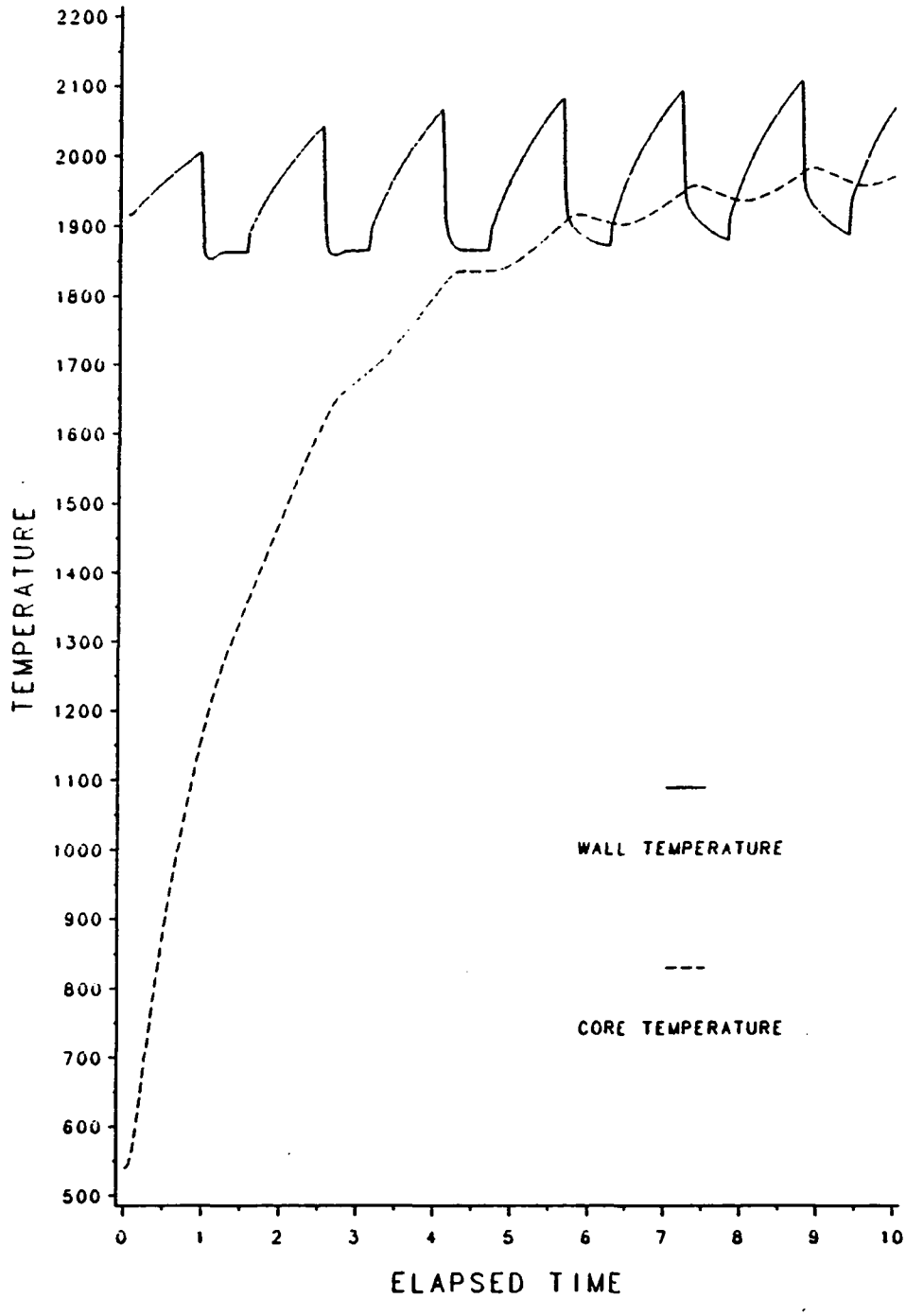

Figure 4.22 The core temperature variations of the air with time at z/L=0.4.

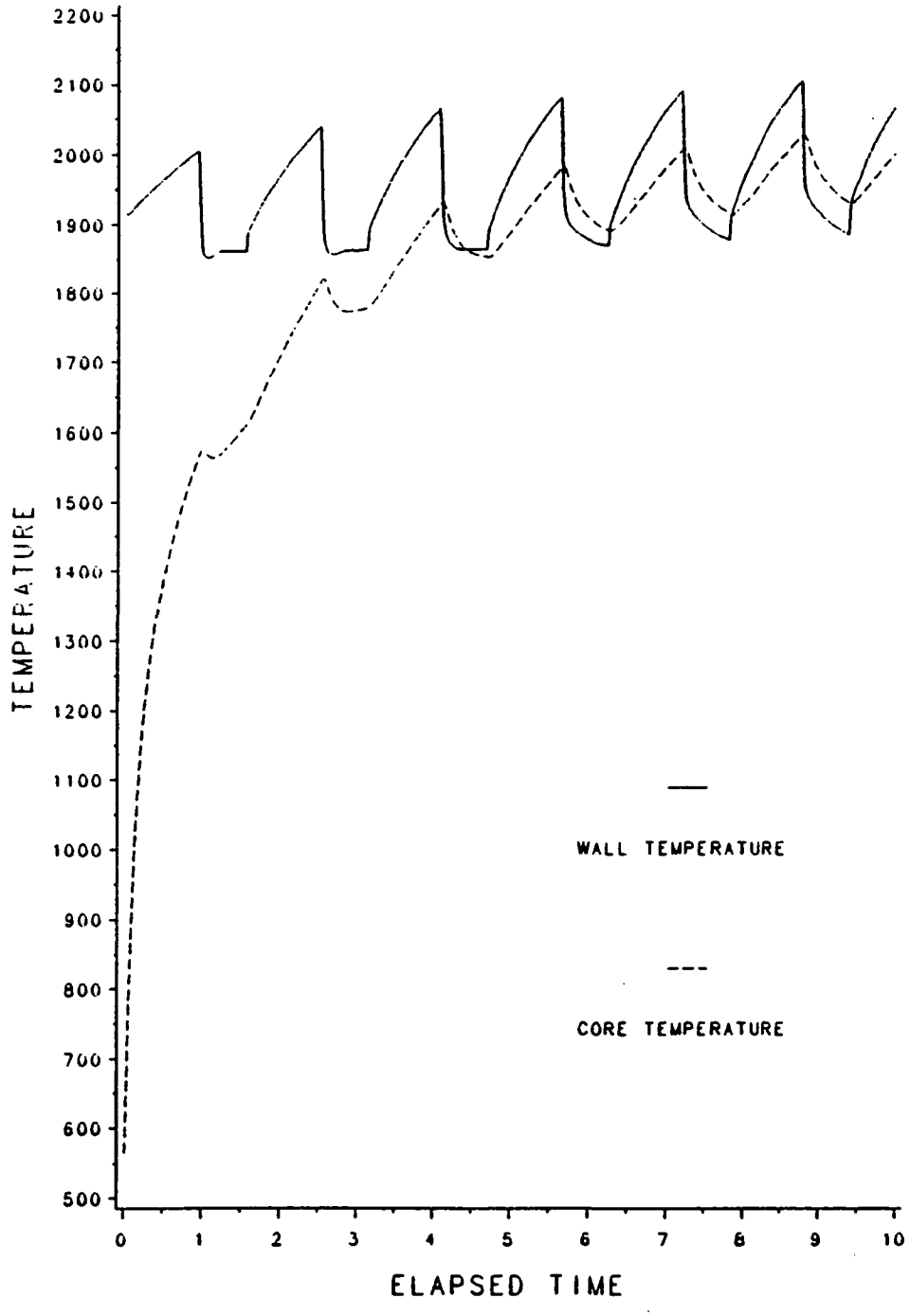

Figure 4.23 The core temperature variations of the air with time at z/L=0.7.

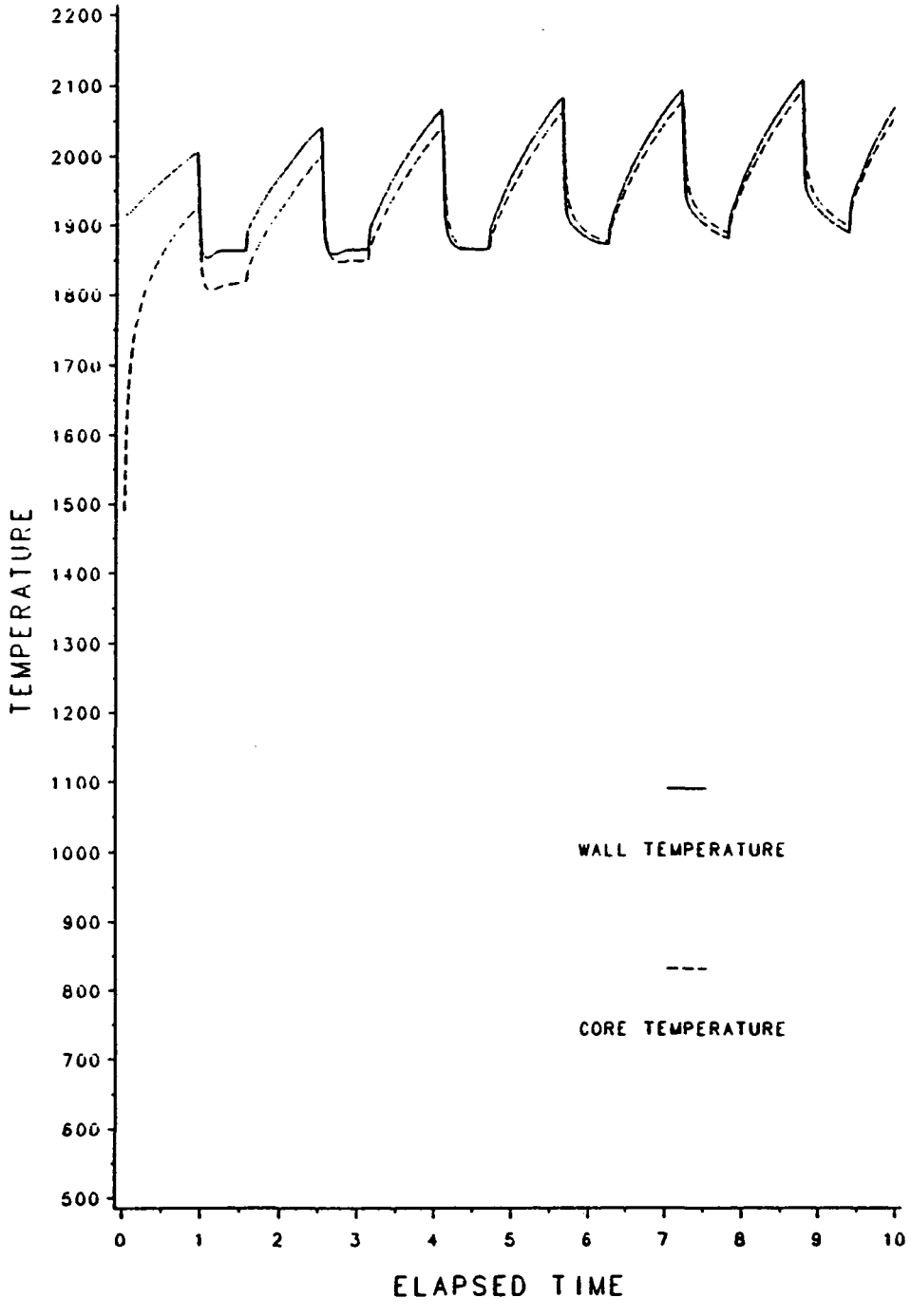

Figure 4.24 The core temperature variations of the air with time at z/L=0.9.

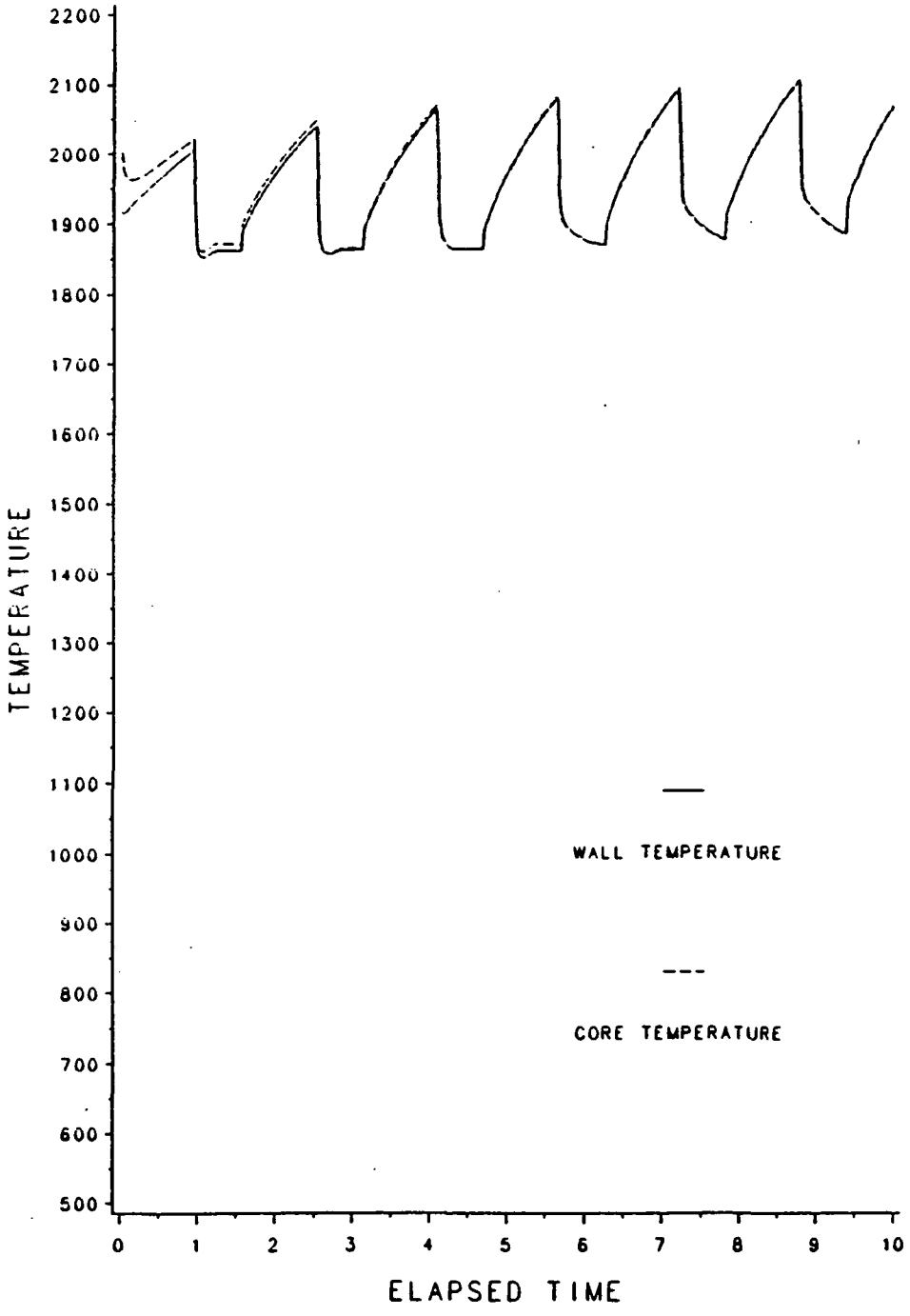

Figure 4.25 The temperature variations of the air with time in mixing region, $0.9 \leq z/L \leq 1.0$.

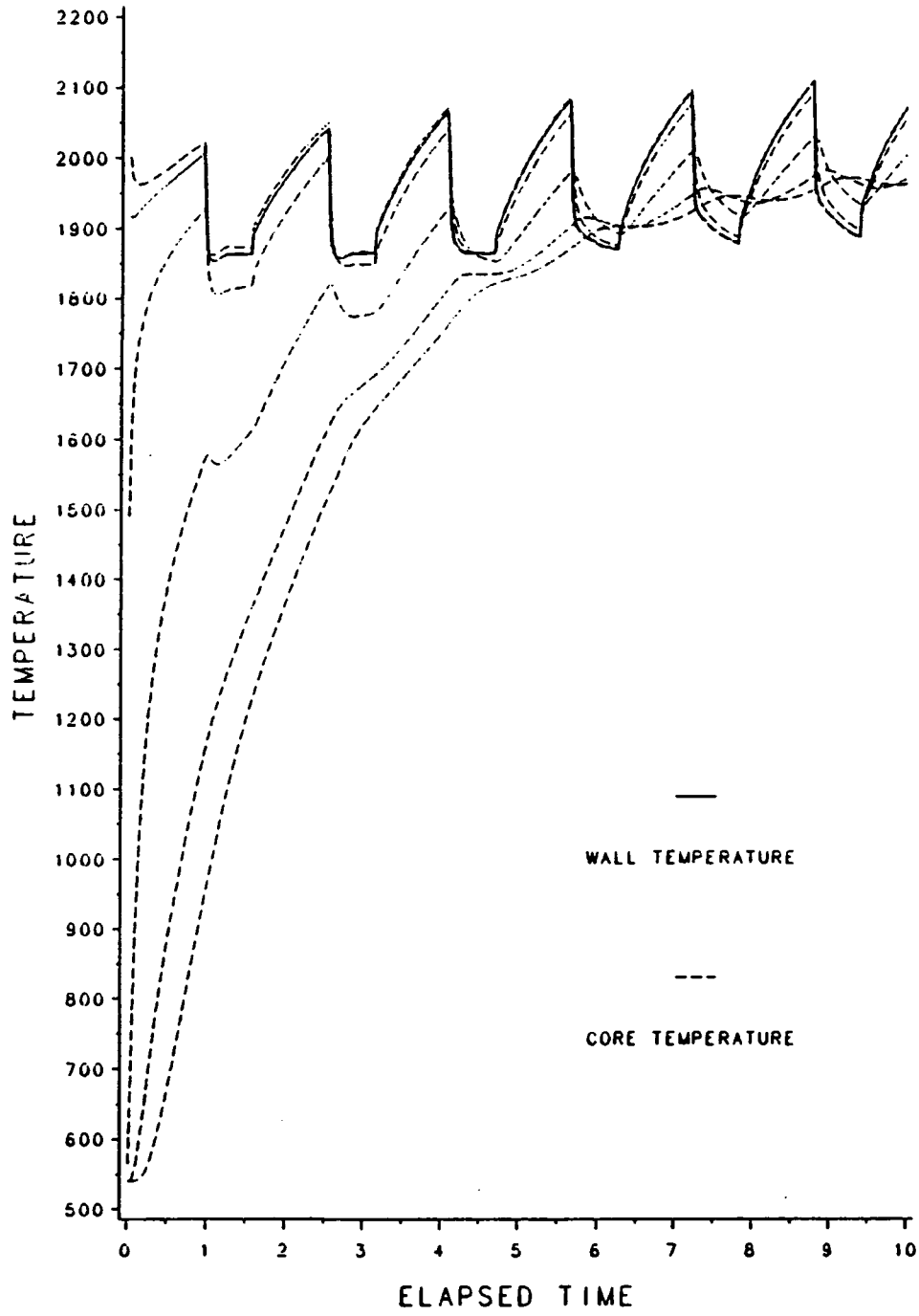

Figure 4.26 The temperature variations of the air with time at z/L=.1, .4, .7, .9, and .95.

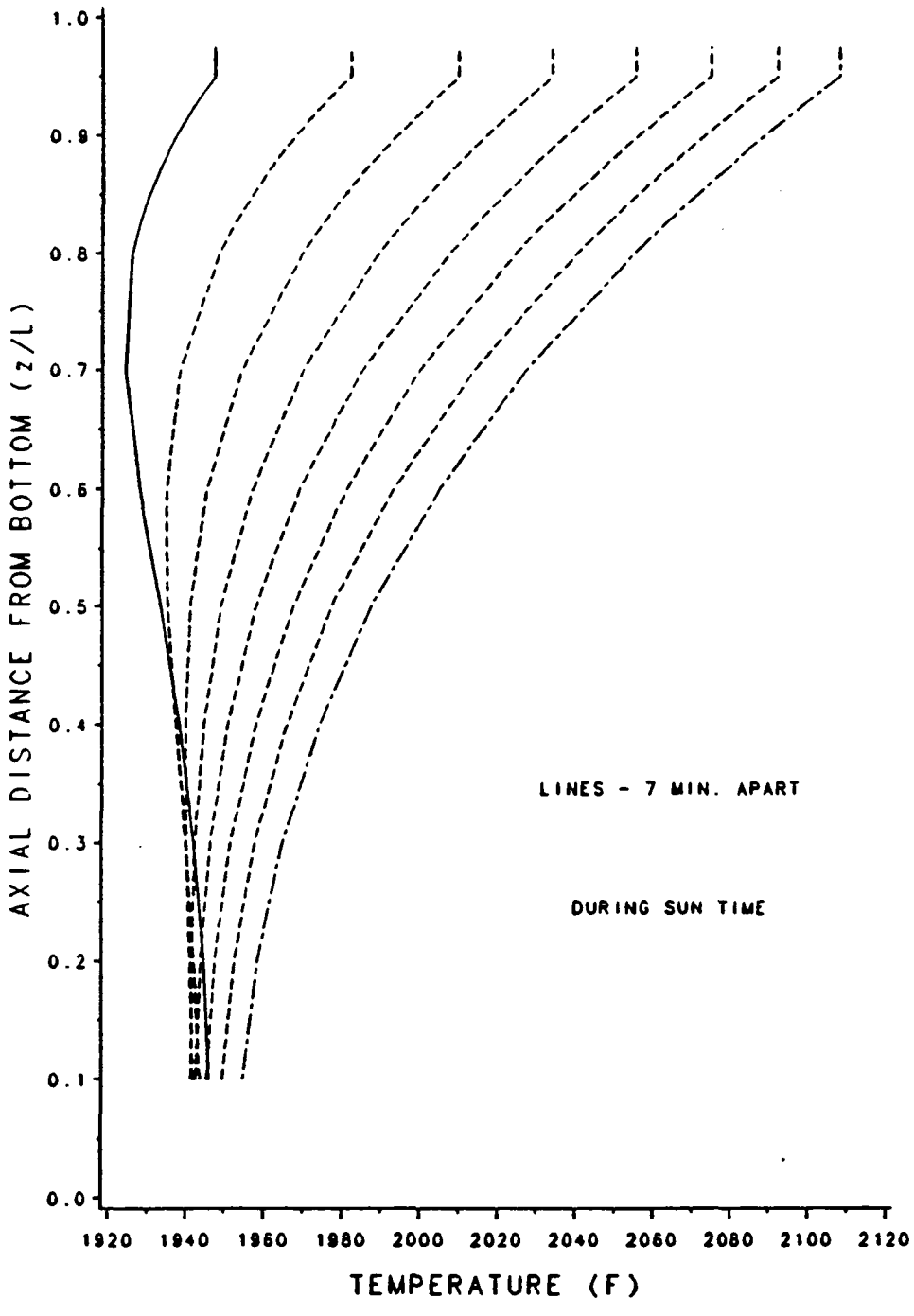

Figure 4.27 Axial variation of the air temperature during the sun period, $7.825 \leq t(hr) \leq 8.792$.

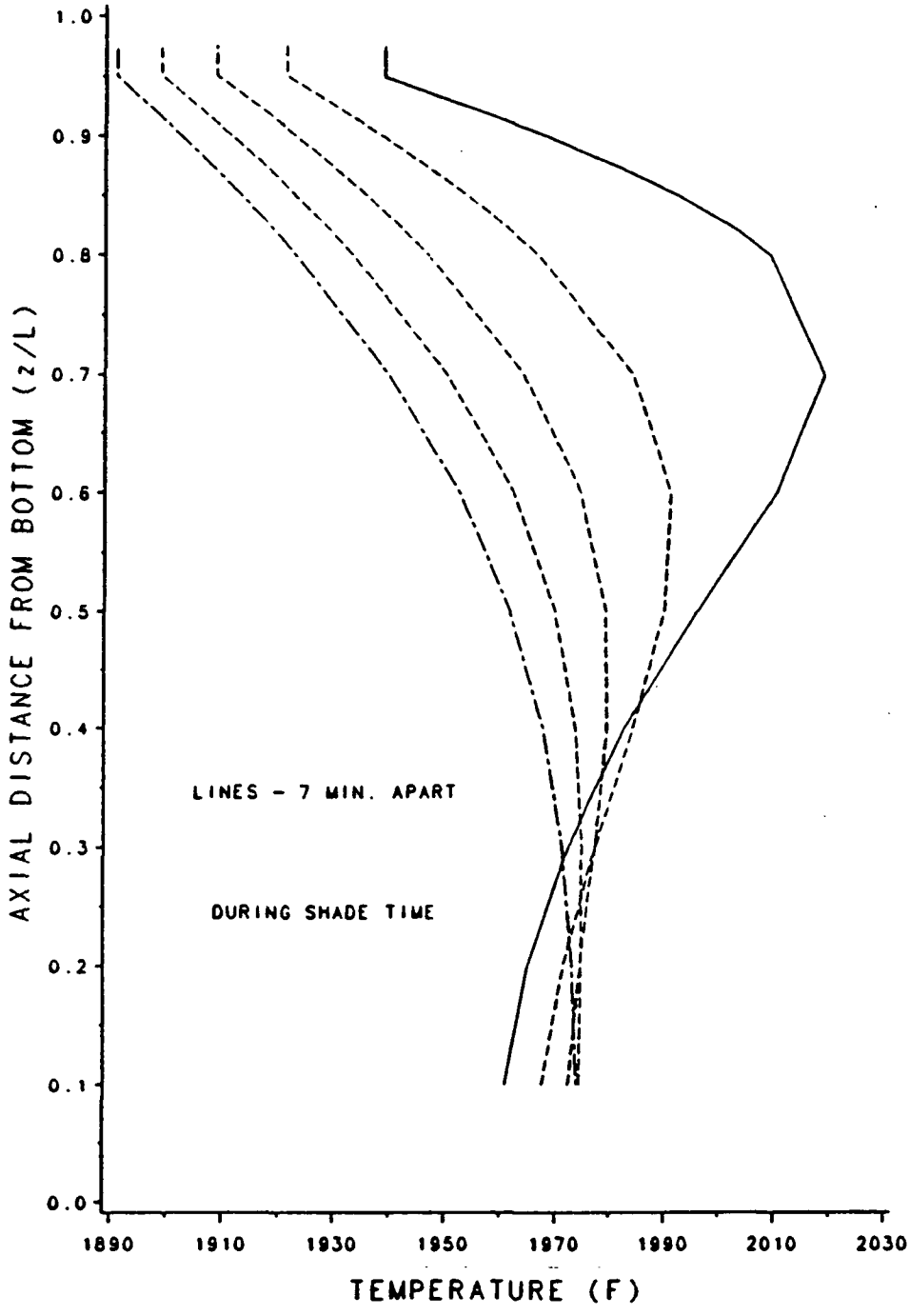

Figure 4.28 Axial variation of the air temperature during the shade period, $8.792 \leq t(hr) \leq 9.39$.

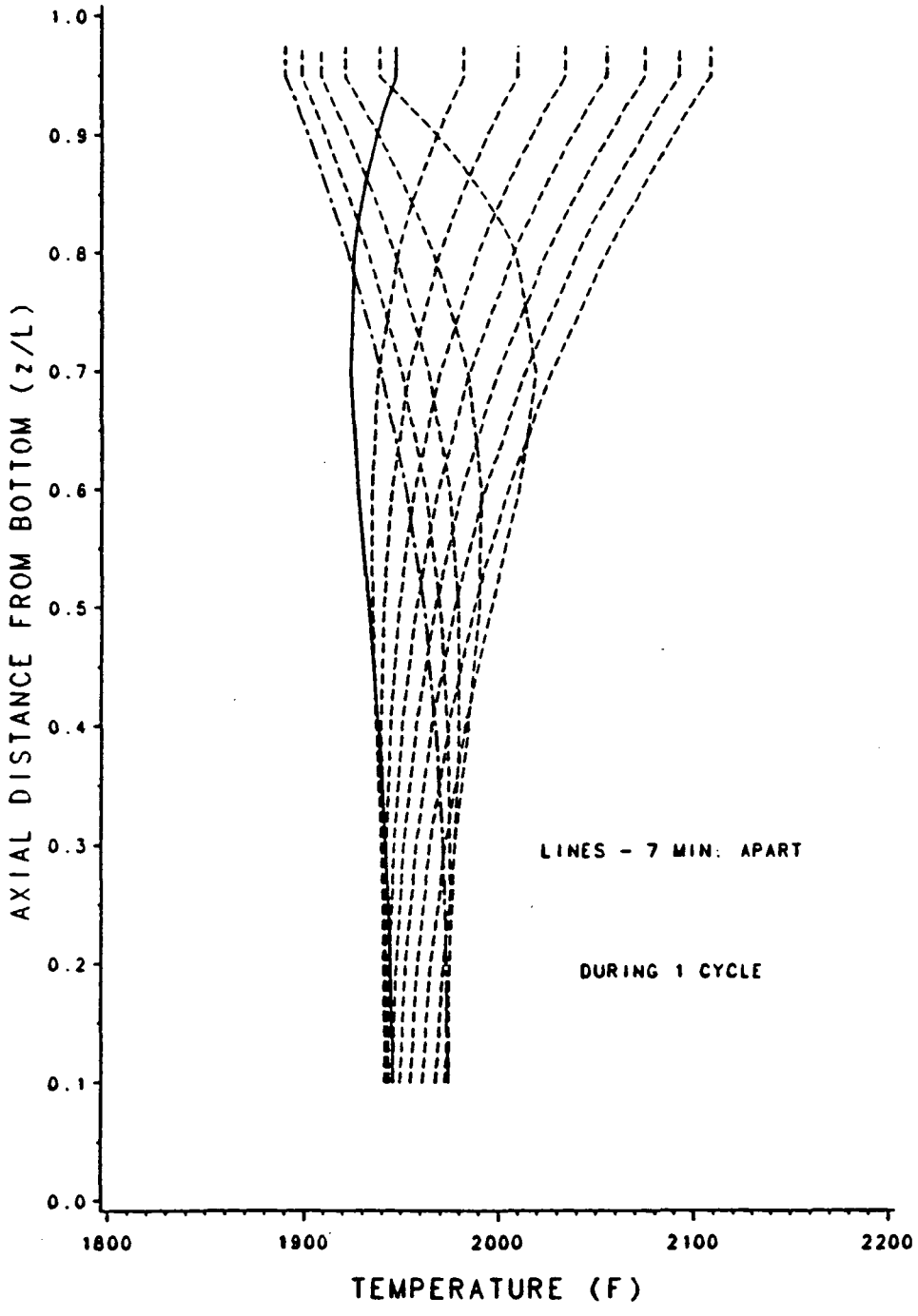

Figure 4.29 Axial variation of the air temperature during one cycle, $7.825 \leq t(hr) \leq 9.39$.

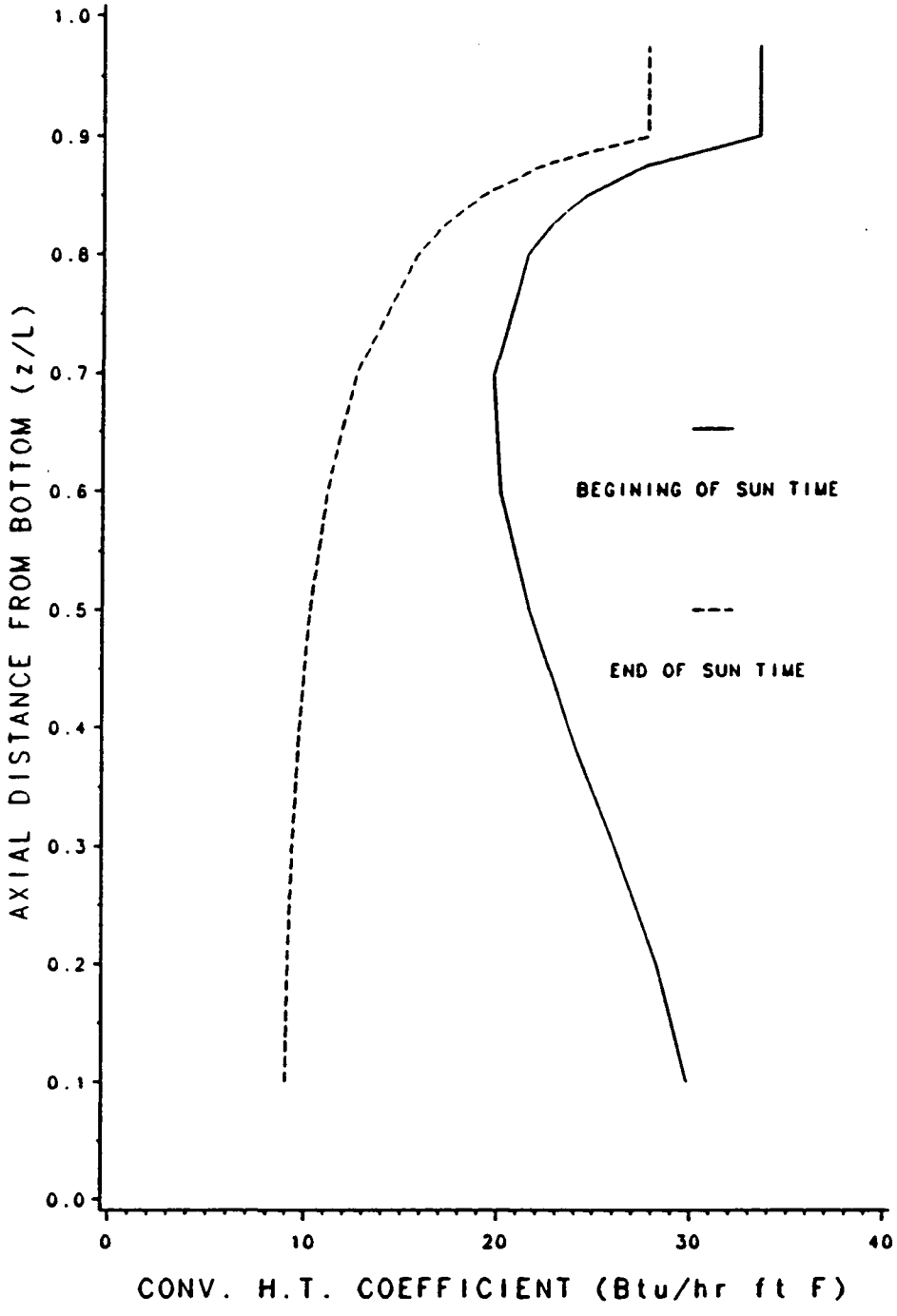

Figure 4.30 Axial distribution of local convective heat transfer coefficient at the beginning and the end of the sun time, $t(hr) = 7.83$ and $t(hr) = 8.79$.

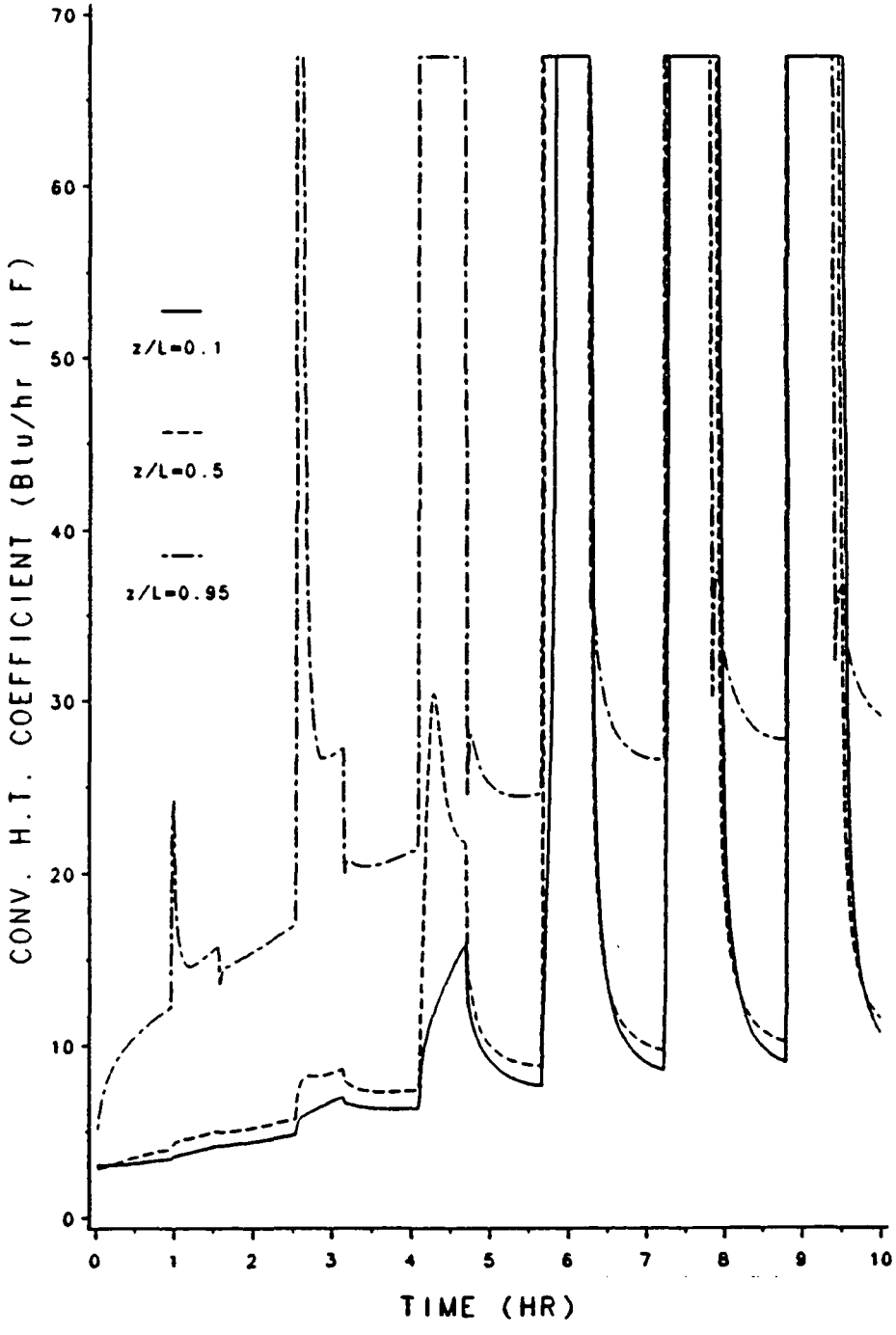

Figure 4.31 Cyclic variation of the convective heat transfer coefficient at three different axial locations, z/L=0.1, 0.5 , and 0.95.

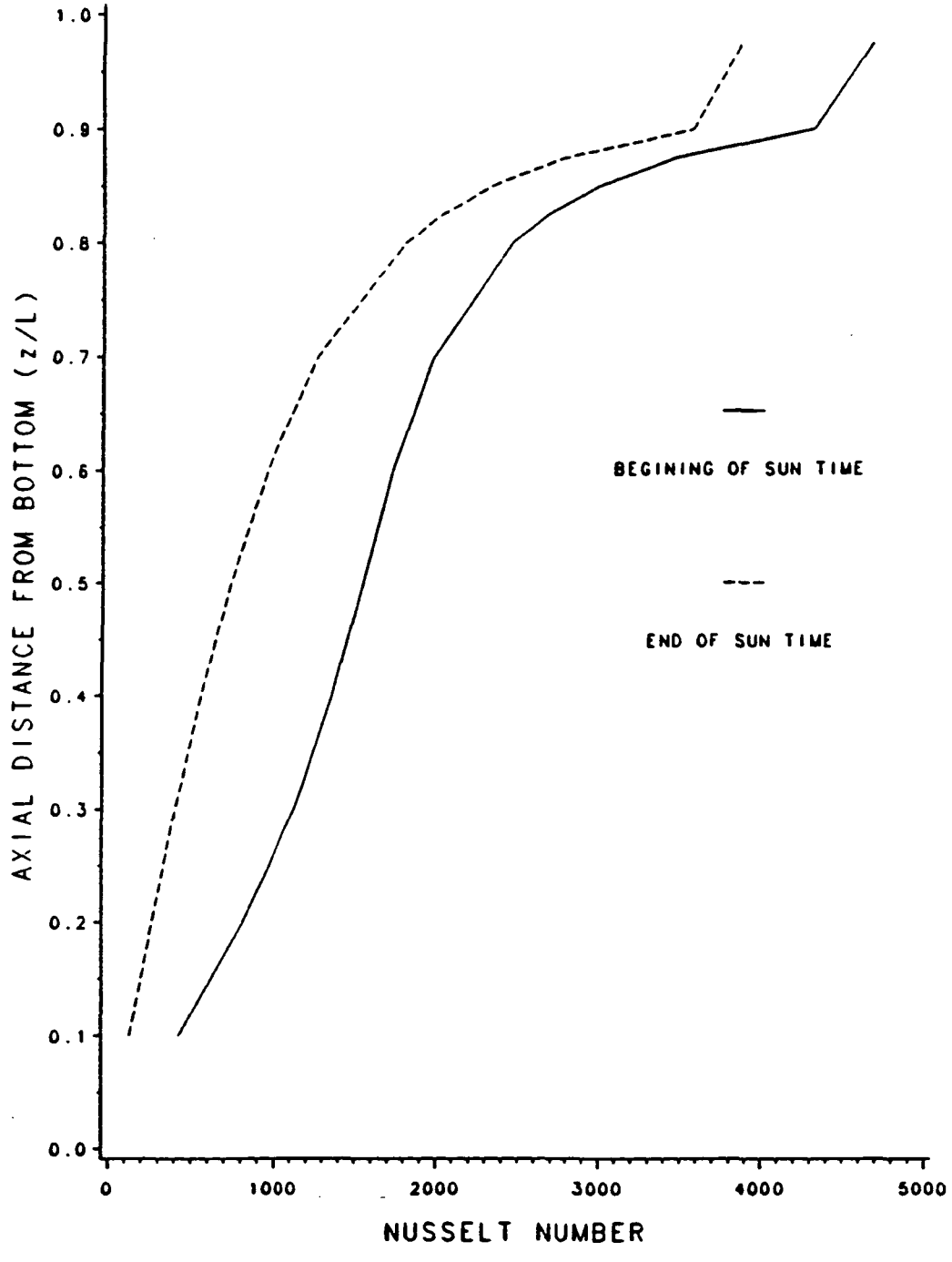

Figure 4.32 Axial distribution of local Nusselt number at the beginning and the end of the sun time, $t(hr) = 7.83$ and $t(hr) = 8.79$.

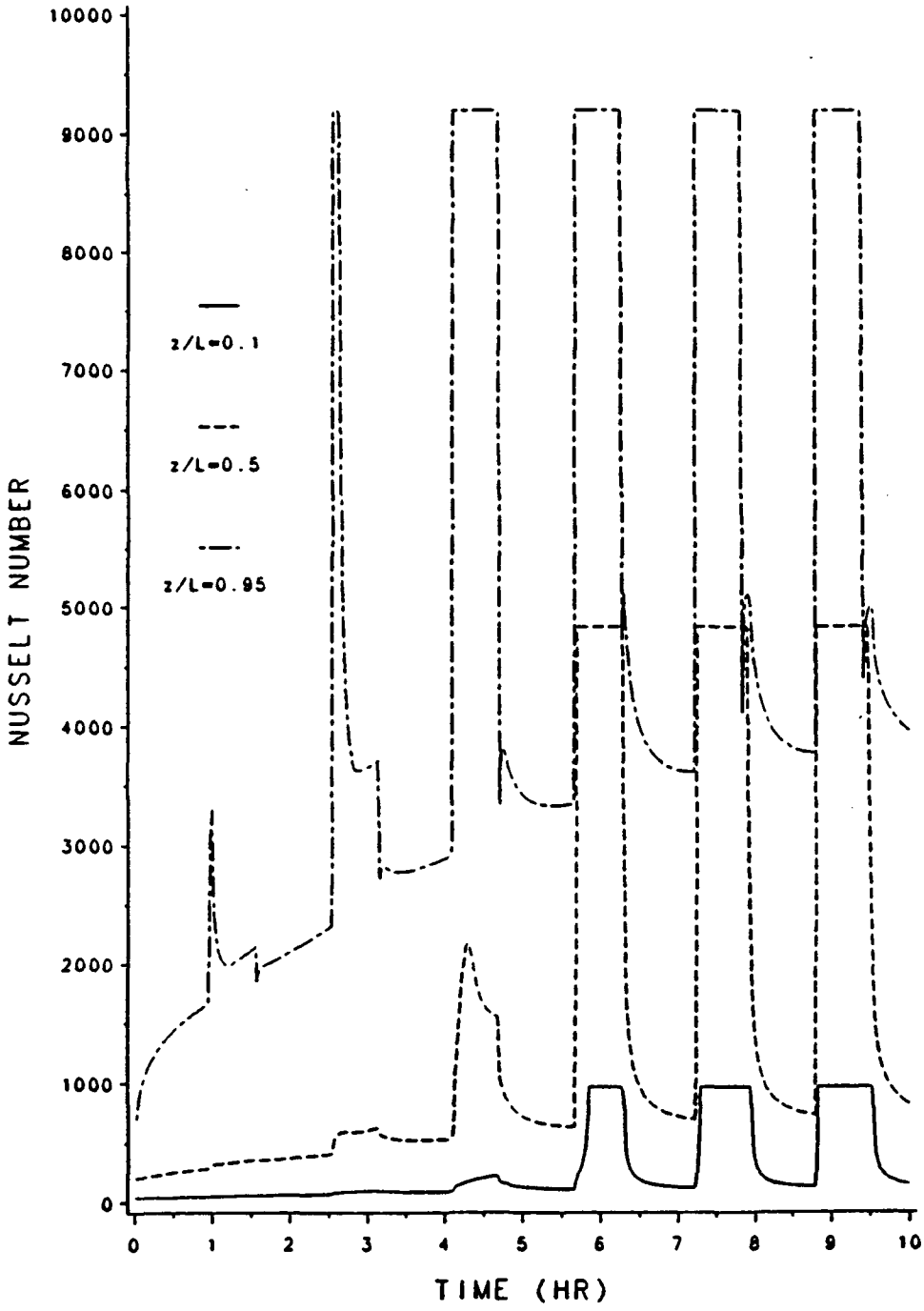

Figure 4.33 Cyclic variation of the Nusselt number at three different axial locations, z/L=0.1, 0.5 , and 0.95.

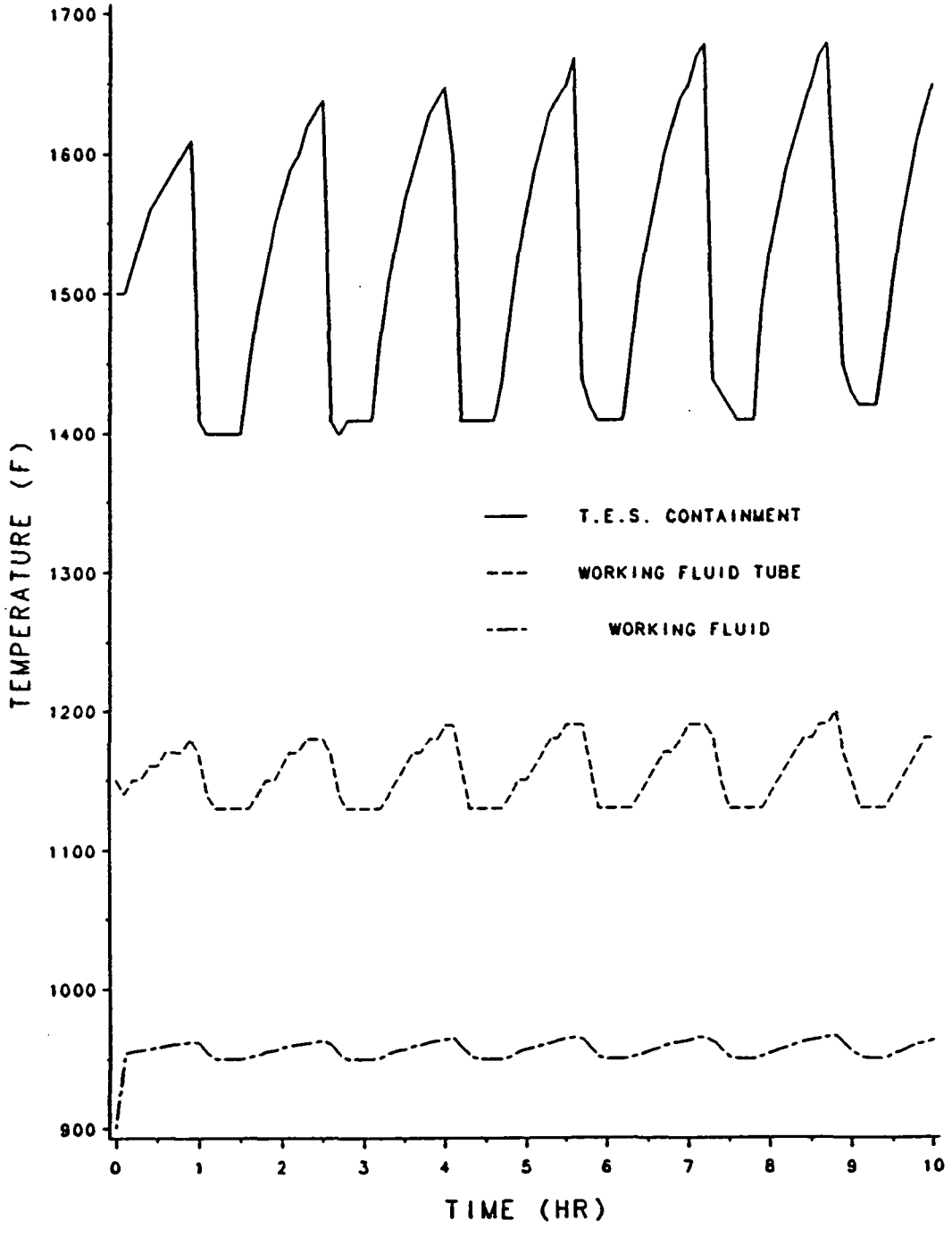

Figure 4.34 Temperature variation of the receiver components with time at the inlet section of the working gas. (with natural convection)

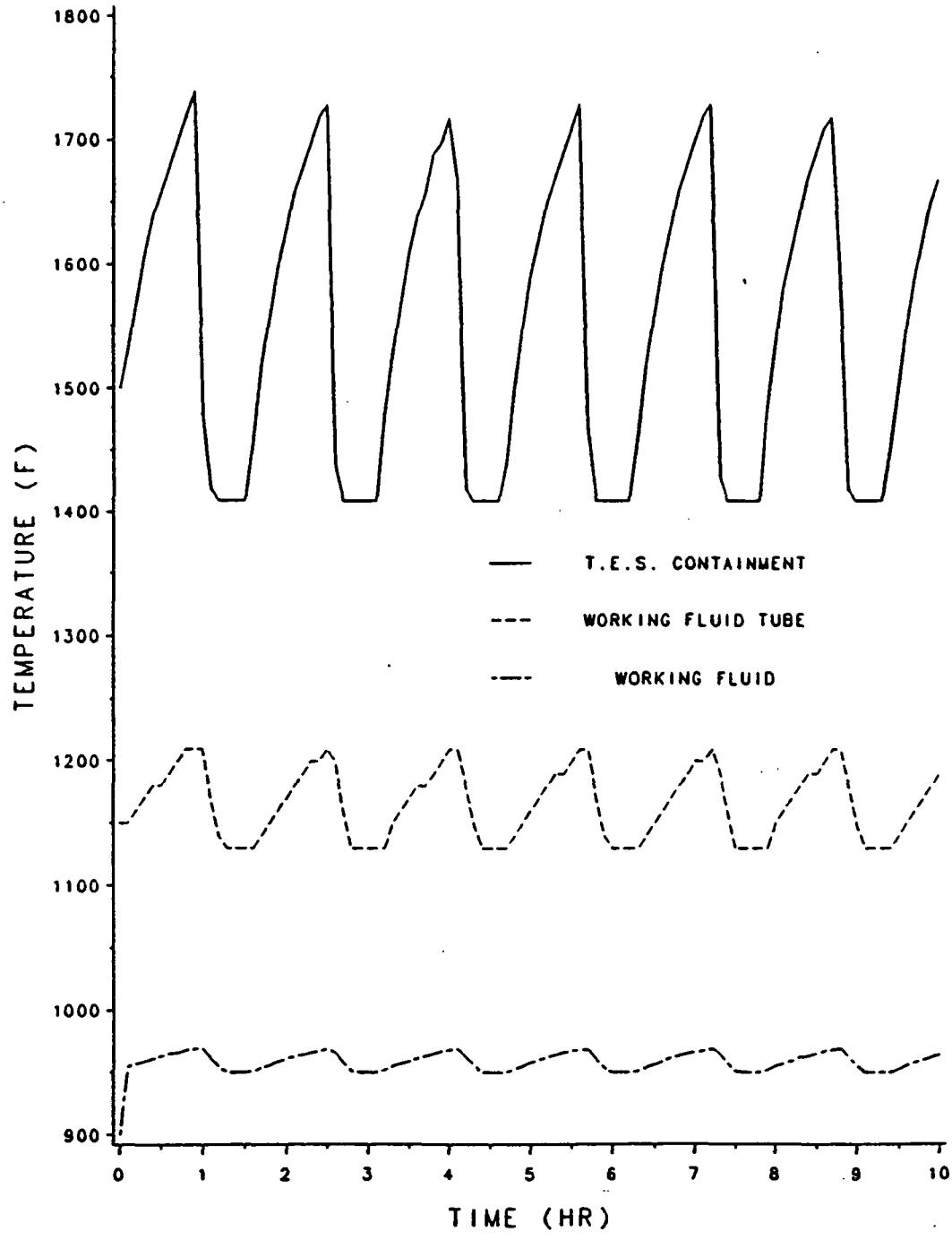

Figure 4.35 Temperature variation of the receiver components with time at the inlet section of the working gas. (without natural convection)

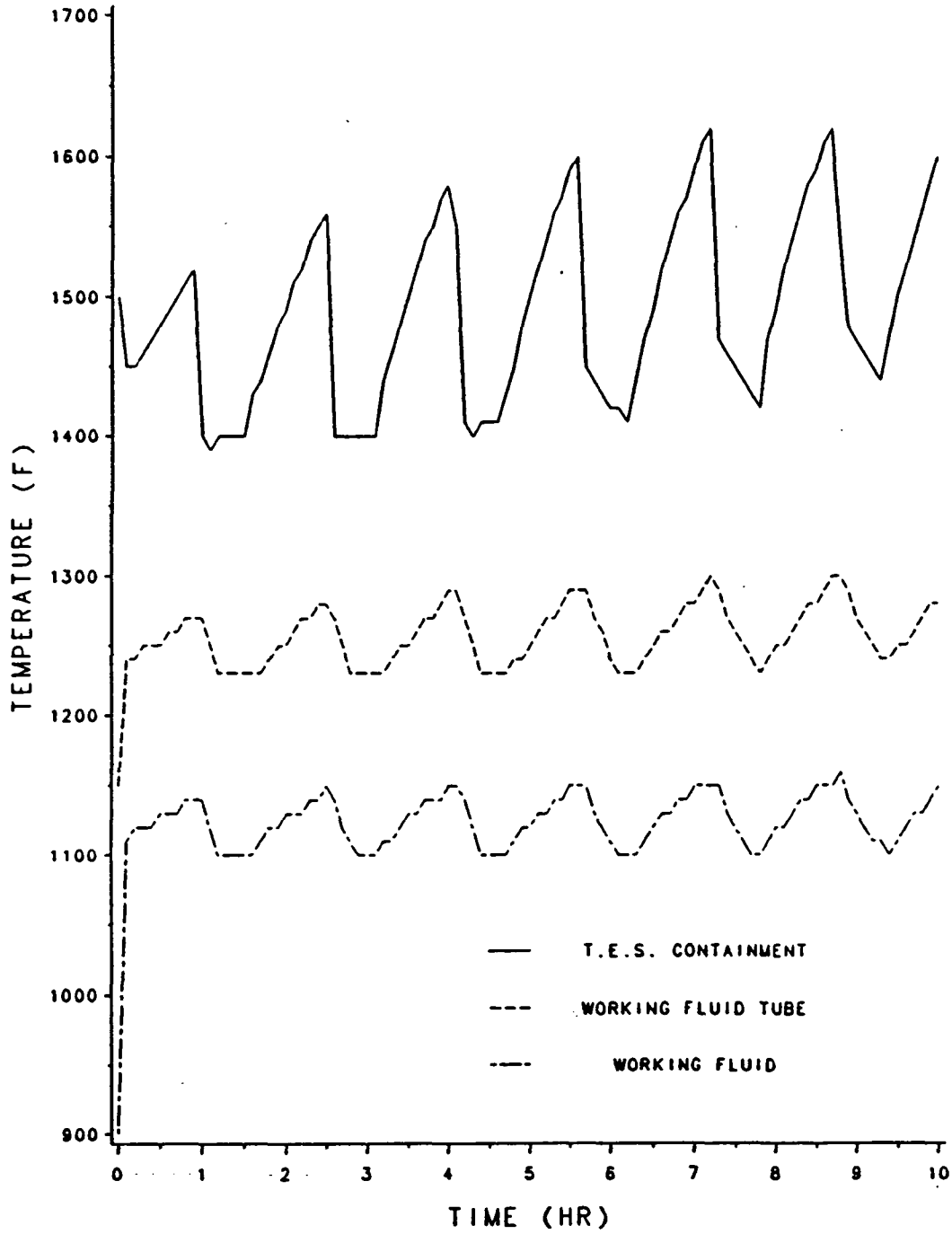

Figure 4.36 Temperature variation of the receiver components with time at the middle section of the working gas. (with natural convection)

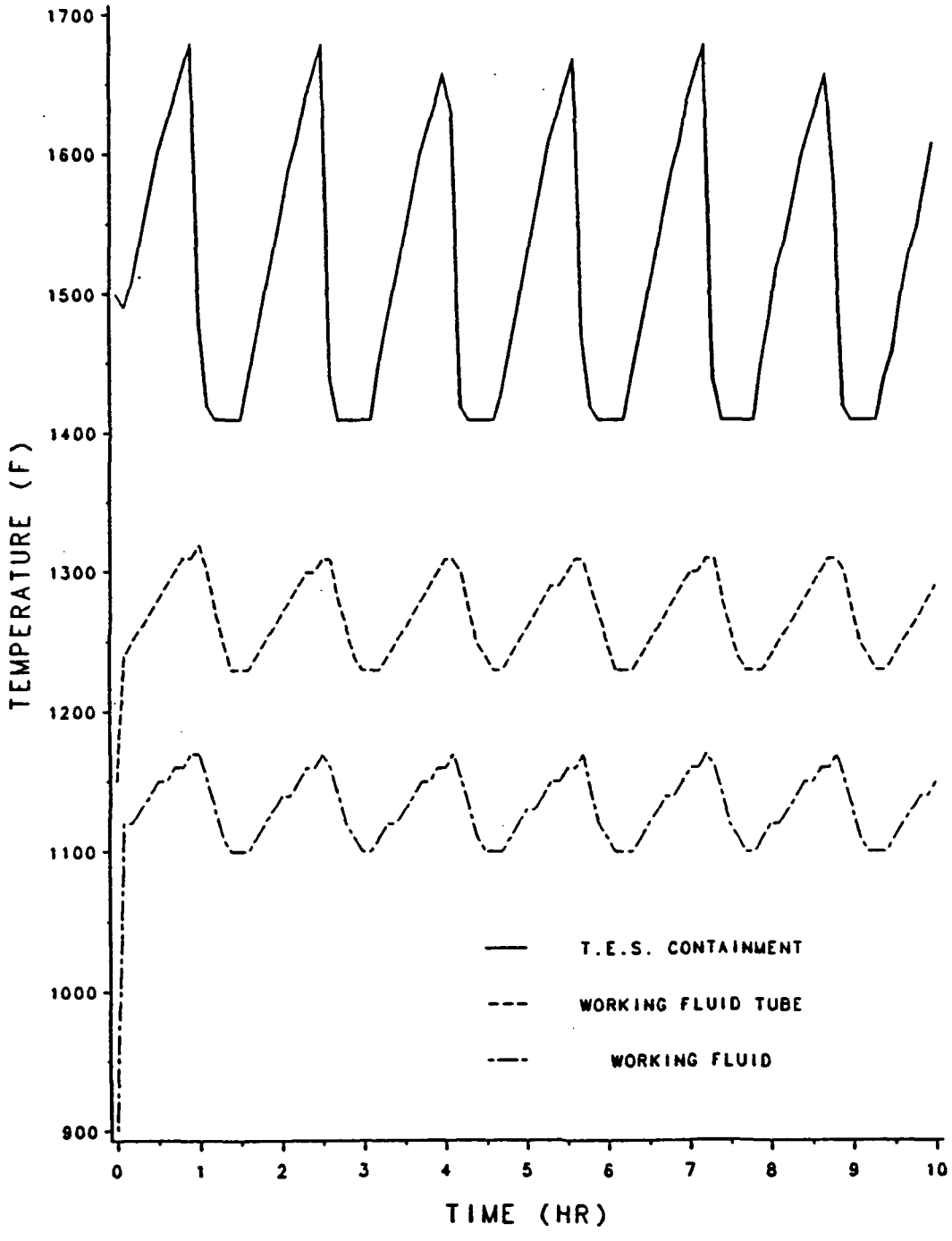

Figure 4.37 Temperature variation of the receiver components with time at the middle section of the working gas. (without natural convection)

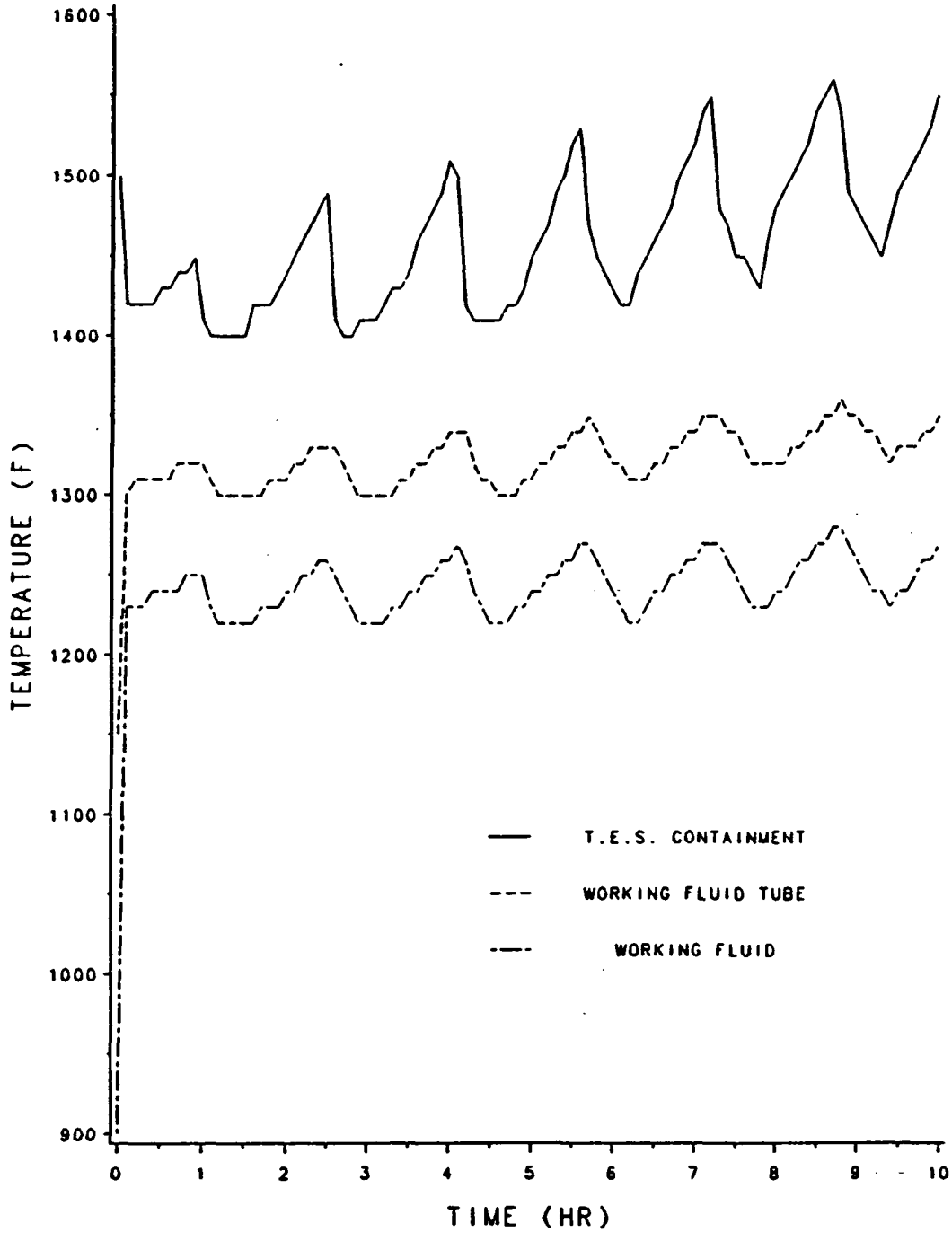

Figure 4.38 Temperature variation of the receiver components with time at the outlet section of the working gas. (with natural convection)

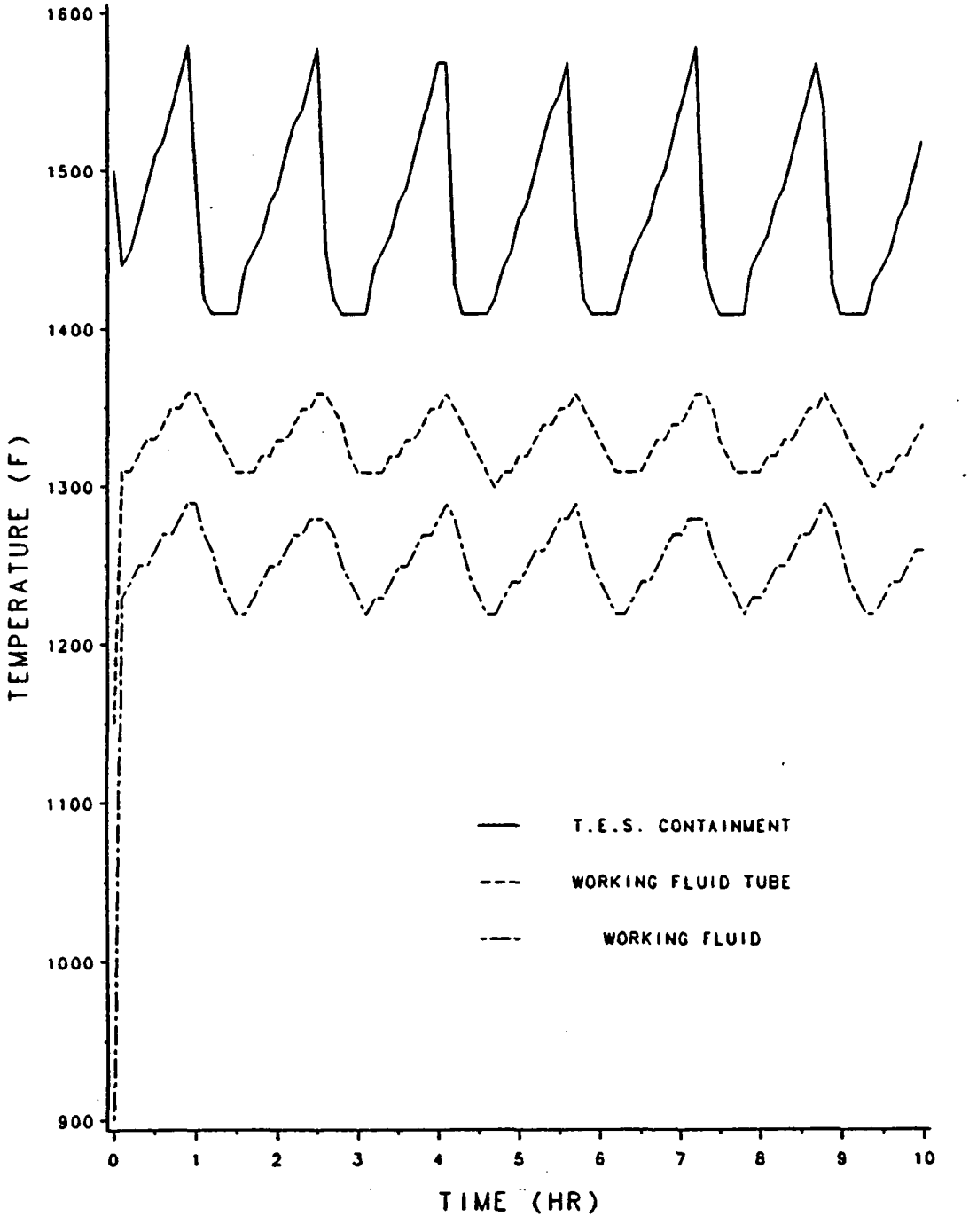

Figure 4.39 Temperature variation of the receiver components with time at the outlet section of the working gas. (without natural convection)

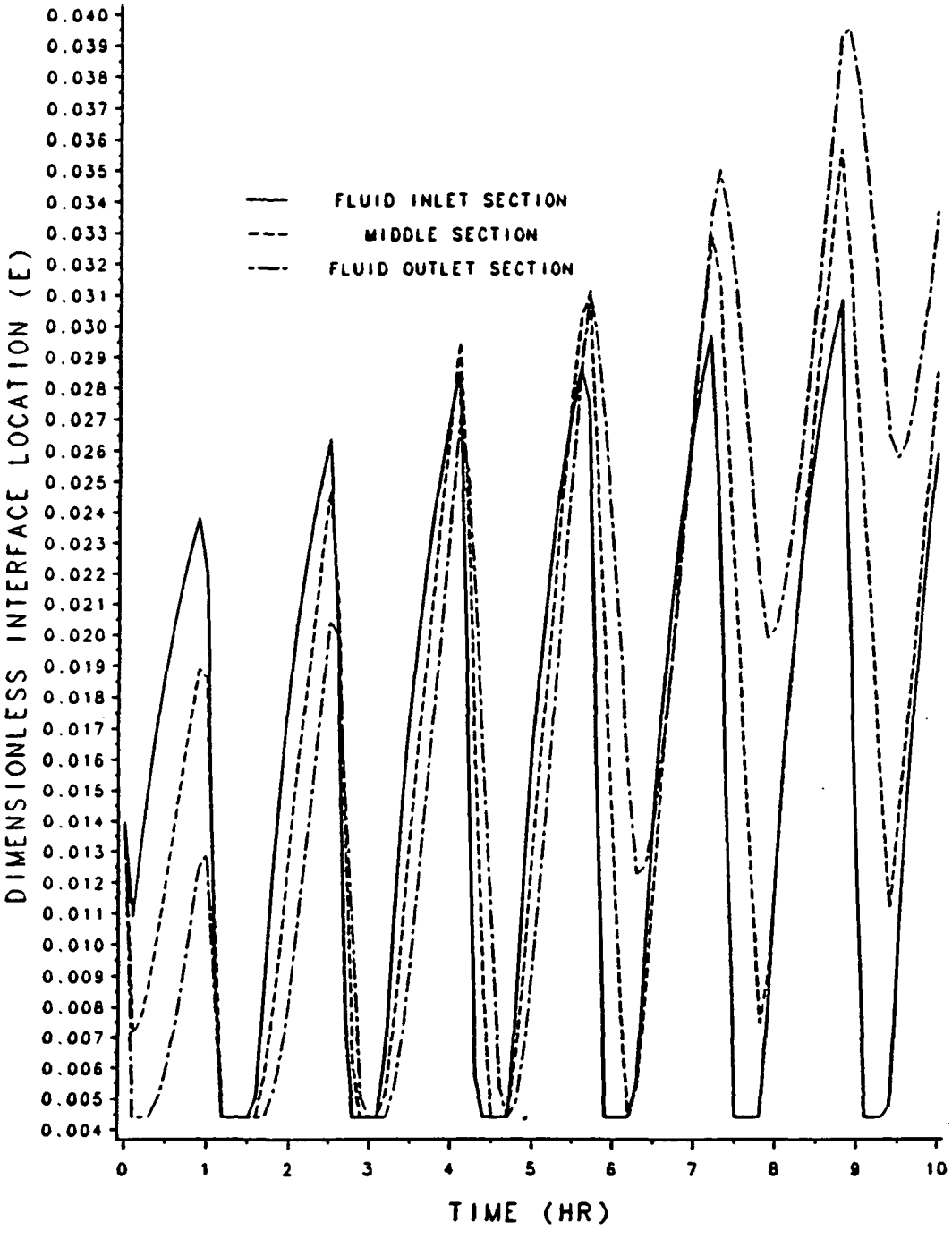

Figure 4.40 Dimensionless interface location as function of time at different axial location. (with natural convection)

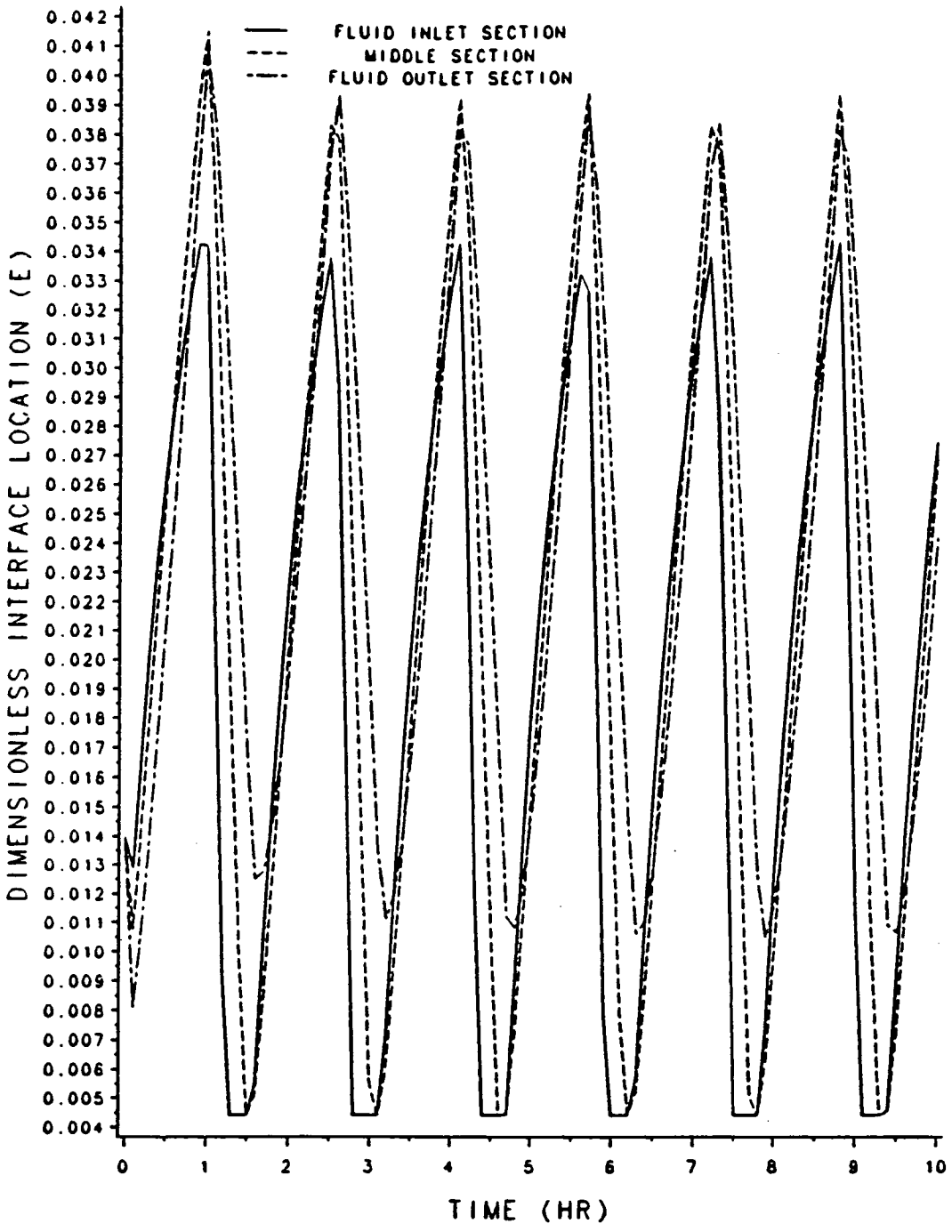

Figure 4.41 Dimensionless interface location as function of time at different axial location. (without natural convection)

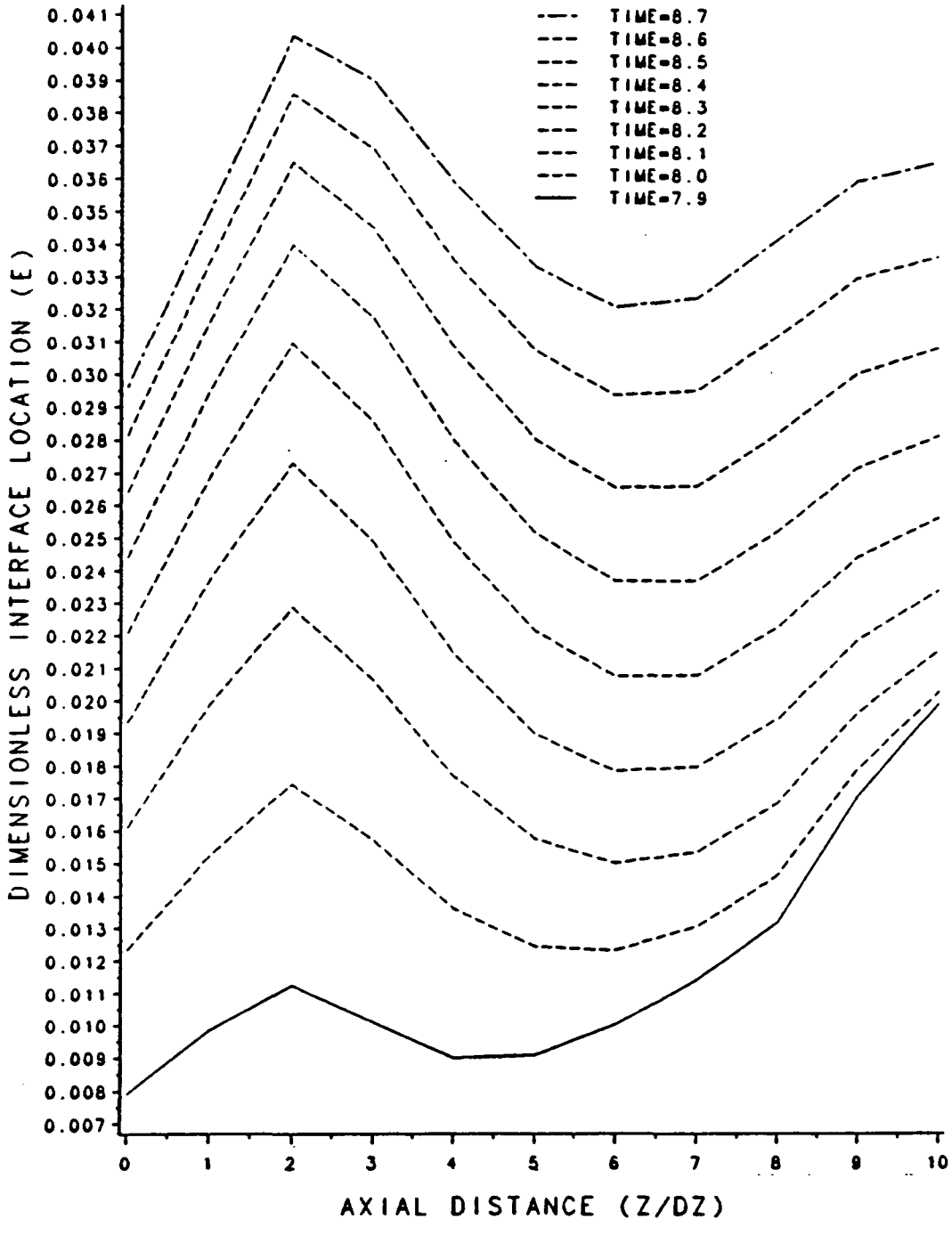

Figure 4.42 Two-dimensional interface motion during sun time for different times. (with natural convection)

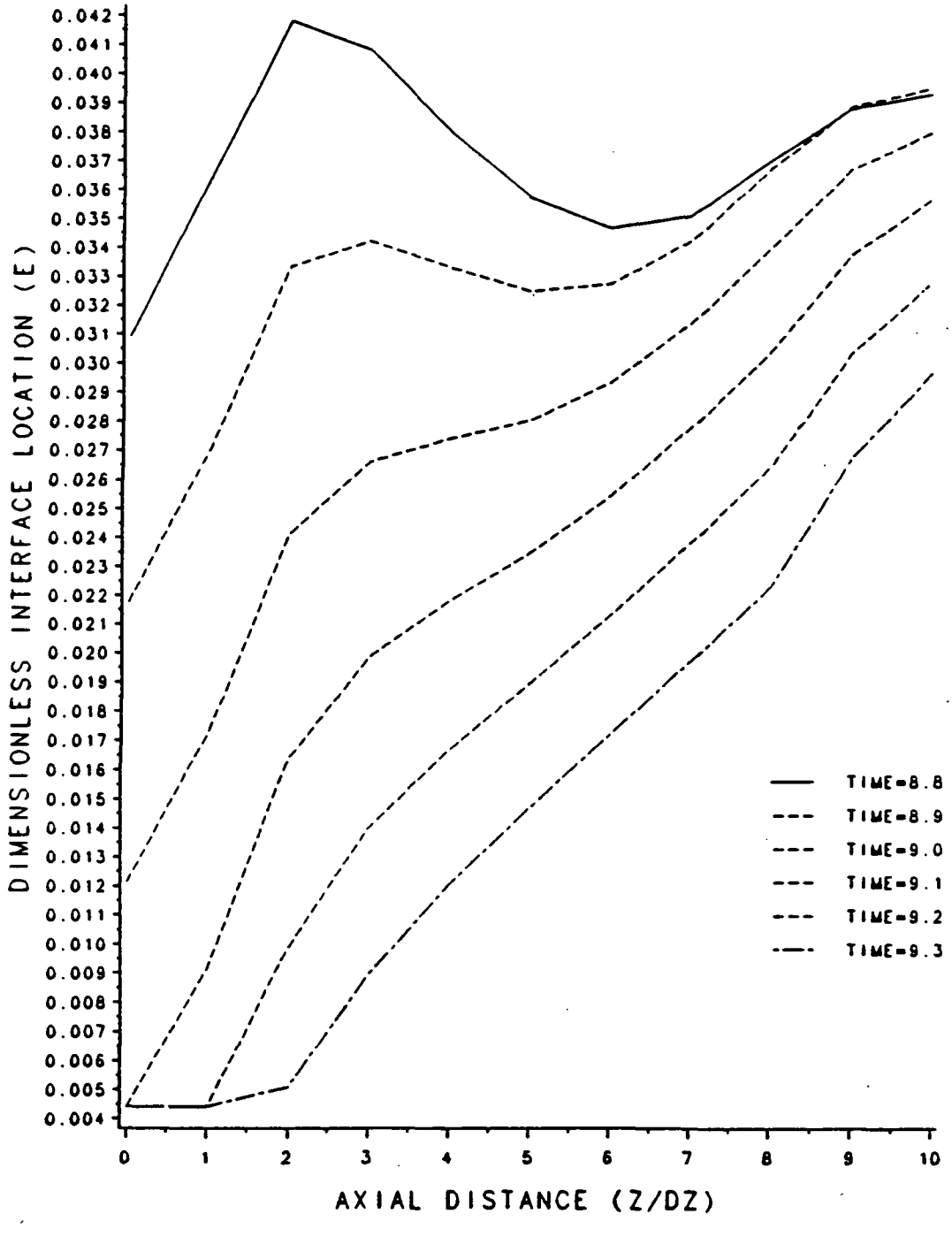

Figure 4.43 Two-dimensional interface motion during shade time for different times. (with natural convection)

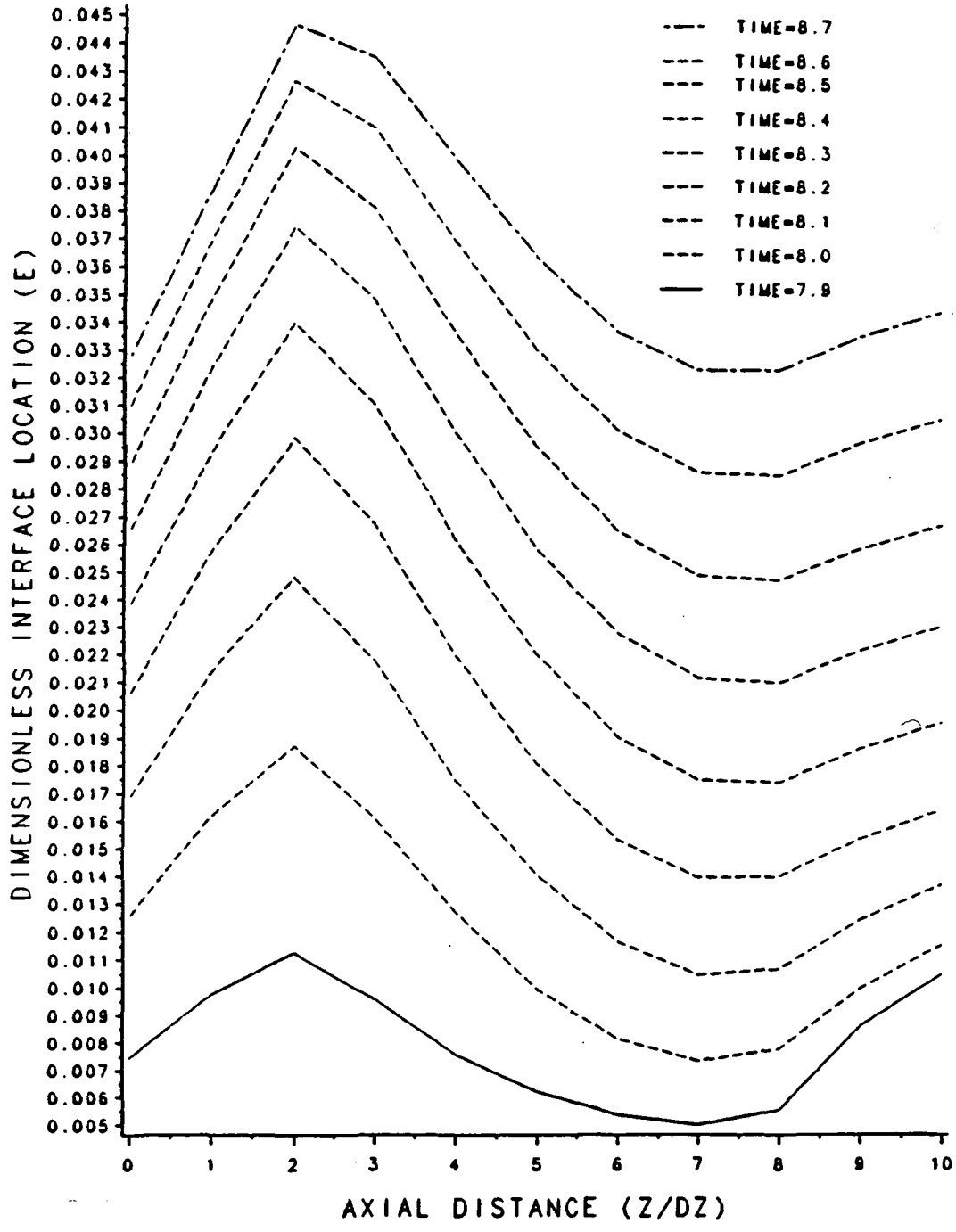

Figure 4.44 Two-dimensional interface motion during sun time for different times. (without natural convection)

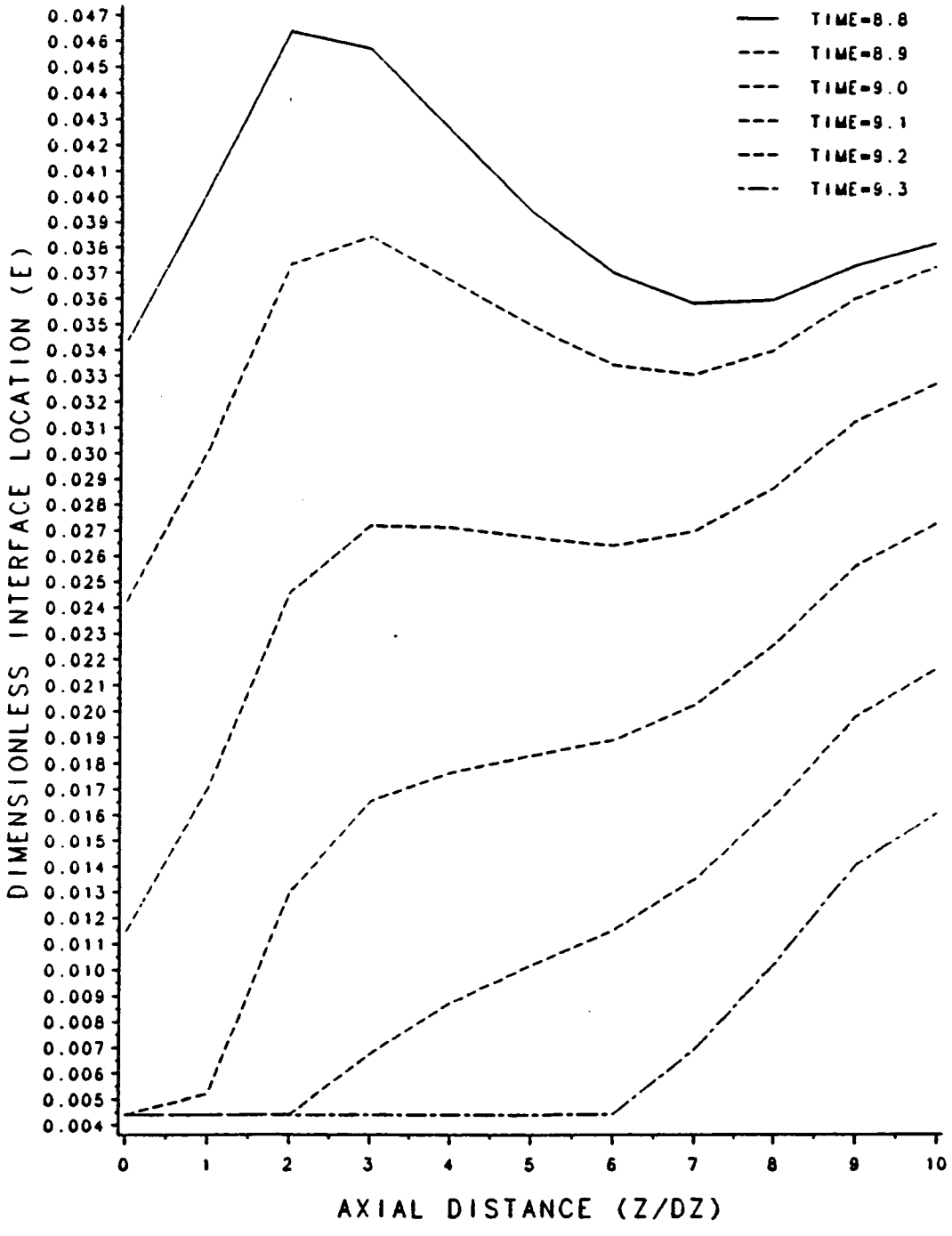

Figure 4.45 Two-dimensional interface motion during shade time for different times. (without natural convection)

CHAPTER V

SUMMARY AND CONCLUSIONS

5.1 Summary

The Space Station Freedom solar dynamic power generating system concept utilizes solar energy as the heat source in a closed Brayton cycle to develop auxiliary electrical power in space. In the present work, attention has been given to the solar receiver. The solar receiver is a combination of heat exchanger and thermal energy storage device which transfers a certain amount of heat to a Brayton cycle working gas during both sun and shade periods of an earth orbit. During a sun period, a parabolic collector has been used to focus solar radiation into the receiver through an aperture located at the collector focal point. The solar energy input is normally designed to be greater than that required for Brayton power system operation during a sun period. Now the excess energy can be stored within the receiver energy storage device as heat of fusion of phase change material (PCM) and then can be withdrawn during the following shade period to maintain power system operation.

Heat transfer analysis of phase change material has been made to identify the accurate location of the solid-liquid interface and this analysis is then applied to the the receiver thermal energy storage subsystem to evaluate the var-

ious parameters involving heat transfer through the PCM. Because of extreme complexity of the PCM thermal behavior, such as natural convection due to density difference between the two phases and void formation due to thermal expansion, present solution scheme is confined to heat conduction analysis without void or natural convection effects. However, this simplified thermal model makes the analysis tractable and yet retains the most important characteristics of the receiver.

Due to time and cost constraints it is likely that most components of the space station solar dynamic power system will undergo extensive earth-based testing as opposed to orbital testing. This will expose them to gravity driven effects due to the presence of the gravity and the air. The presence of gravity and the air has been identified as the parameter that can significantly alter the performance of the receiver during a 1-g test operation of the system.

Hereby, in the present work, another attention is given to the natural convection inside a receiver cavity to estimate its effects on the receiver performance during 1-g operation. Due to the lack of appropriate emperical formula for internal natural convection problem which can be assumed to be suitable for the receiver cavity geometry, more rigorous method has been presented which includes entire flow field inside a cavity and identify different flow characteristics within the domain.

As a first step to the proposed receiver thermal analysis described above, overall energy balance involved in the solar receiver has been studied to understand conceptual design objective and scope in Chapter I. Also, the method of approximating amount of energy requirements from the other given energies was obtained based on lumped capacitance assumption.

In Chapter II, the method of predicting thermal behavior of axisymmetrical phase change material resides between two concentric cylinder, has been

investigated using non dimentionalized variables. Both implicit and explicit numerical scheme was tested using different number of radial nodes of 4, 6, 9, 12, 15, 18 for the one dimentional ice formation problem which has been solved analytically. The location of the solid/liquid interface of the material as well as the temperature distribution of the phase change material has been calculated. From the results, implicit scheme has been identified unstable for this problem and explicit scheme gives stable results and the results are in good agreement with the analytical results. After estimating required CPU time and solution accuracy the explicit scheme with 9 radial nodes was selected and used in analizing receiver TES heat transfer. Instability of the implicit scheme has been presumed to result from the increasing round off error due to large number of arithmatic operations required to invert the matrix for the increasing number of radial nodes. As an alternative, solving the matrix using iteration method which is not used in present study, may overcome the difficulty. Or using alternate direction implicit (ADI) method which makes the matrix tridiagonal is considered worth to try to improve the results of the simple implicit scheme.

In Chapter III, the flow inside a closed cylindrial enclosure with side wall heated has been investigated using similar solution algorithm developed by Hess and Miller to analyze natural convection effects inside a receiver cavity during 1-g operation. The flow domain was divided into three regions (Figure 3.1), namely, boundary layer, mixing, core region as suggested by previous investigators. In each region, different method has been applied according to the flow characteristic. The velocity and temperature distribution are calculated in the boundary layer region using Karman-Pohlhausen method and the temperature of the mixing region is obtained by performing the energy balance over the control volume of mixing region. Also one dimensional velocity and temperature

has been calculated in the core region. The three regions are coupled with each other, therefore a solution of one region becomes the boundary condition of the other region.

Numerical data obtained for water inside a circular cylinder subject to two different boundary temperature at the top perimeter of the cylinder are compared with Miller's (1977) numerical solution which uses full Navior-Stokes equation and Hess's integral results. Velocity distribution inside the boundary layer and temperature distribution of the core region are in good agreement with Miller's results, and due to new temperature profile modefied from the parabolic profile suggested by Hess, excellant agreement were shown in predicting temperature distribution in mixing region which has been considered as important region connecting boundary layer and core region.

The numerical method of Chapter II and III has been applied to the Brayton cycle solar dynamic receiver thermal analysis. And two subroutines developed in Chapter II and III, for TES analysis and natural convection analysis respectively, have been incorporated into a computer program written for analizing solar receiver thermal performance which does not have capability of those analyses. In Chapter IV, the results are compared with the results obtained without TES analysis and/or natural convection analysis.

5.2 Conclusions

5.2.1 *Effect of TES on Receiver Thermal Performance*

It has been identified that the temperature variation of the working gas at the outlet section during an orbit cycle can be reduced more than 50 % by adding phase change material to the place between the inside cavity surface and working gas tube so that more constant power output of the entire system can

be obtained which is one of the most important objective of the solar dynamic power system. However, higher maximum surface temperature resulting from thermal energy storage, has been observed which might cause the damage or structural failure of the TES containment material.

During the sun time, incoming solar energy has been used to increase the surface temperature due to larger thermal resistance of the PCM while the energy is transfered to the working gas at much faster rate when no TES is present. As a result, different effect has been identified for different receiver components according to relative location of the receiver component to PCM of thermal energy storage. For working gas and gas tubing, temperature fluctuation during a cycle has been significantly reduced (60%) with almost same average temperature. For cavity surface, on the other hand, almost same temperature fluctuation was obtained with noticeably increased average temperature.

Since only 60 % of the PCM has been melted during the cycle and most PCM solidifies completely at the end of the shade time, it is desirable to increase the amount of the liquid PCM during the sun time in order to store more energy. If mass flow rate of the working gas is reduced during sun time then more heat would be stored in PCM due to reduced heat transfer to working gas.

5.2.2 *Effect of Natural Convection on Receiver Performance*

On the natural convection effects, nearly the same temperatures for the overall receiver component, including gas outlet temperature, has been obtained in terrestrial results as seen in orbital results. The effect of thermal stratification has been identified which forms the temperature gradient in the axial direction. As a result, local temperature increase at the outlet section and temperature drop at the inlet section of the gas tube was obtained.

The most noticeable outcome from this comparison is that the time aver-

aged temperatures of the receiver components during terrestrial test are almost equal to those obtained from orbital test, instead of giving reduced temperature as in the previous preliminary results. From the results obtained, it is found that the existance of the air and resulting free convection does not have considerable effects on the receiver temperature with the receiver in vertical position with aperature pointing downwards.

This is explained as follows by comparing with the preliminary results discussed in previous section. In the preliminary study, the temperature of the core region inside a cavity was considered as ambient temperature or reservoir temperature which is constant all the time, and no variation in core temperature was assumed. As a result, substantial amount of the convective heat is lost continuously and this heat loss causes the overall decrease in receiver temperature. On the contrary, the core temperature in the detailed study discussed in this section, was calculated neither same as the ambient temperature nor constant all the time during a cycle. Also, with shade time included, the heat loss during the sun time is balanced with the heat supply from the air during the shade time due to sudden change of the wall temperature which is below the air temperature.

It is worth noting that the range between the minimum temperature and the maximum temperature during a cycle is reduced due to natural convection, and one can see the thermal behavior of the air inside a cavity is very similar to that of energy storage material, i.e., cooling the receiver during sun time (storing the energy) and heating the receiver during shade time (liberating the energy). Therefore one should expect the receiver thermal performance would be worse in the orbit than the terrestrial results with free convection effects which predicts less temperature variation and lower maximum temperature of each component of the receiver which might ignore the material failure due to larger thermal

expansion and/or higher maximum temperature than expected during the orbit operation.

5.3 Future Work

Although the present model incorporates complicated aspects of the heat transfer and fluid mechanics in a consistant manner, the following areas can be further developed for an improved and more comprehensive model:

1.) The formation of the void in the phase change material (PCM) due to thermal contraction should be included in the analysis to determine more accurate heat resistance of the PCM .

2.) The convection heat transfer inside the liquid PCM should be included by allowing density variation between the solid and liquid PCM to obtain better approximation on the heat transfer phenomena that takes place in actuality.

3.) A reliable and stable linearizing procedures should be utilized to overcome the numerical difficulties experienced in solving coupled non-linear boundary layer PDE to allow larger time step size in implicit scheme.

4.) The properties variation of the receiver material due to high temperature range (300 °F maximum) during the orbit cycle, should be included to estimate more realistic heat transfer.

Despite some of the limitations of the present heat transfer and flow model, it is believed that the essential features of the phase change phenomena of the thermal energy storage system and flow fields inside a receiver cavity have been illustrated. The present work should be viewed as a first logical step towards a more detailed analysis of the phase change and enclosure free convection problem. In this regard, the future developments pointed above would provide a better

understanding for these problem.

BIBLIOGRAPHY

Barakat, J.Z., & Clack, J.A., [1966], Analytical and experimental study of the transient laminar natural convection flows in partially-filled liquid containers, *Int. Heat Transfer Conf.* **4**, 152.

Baxter, D.F., [1961], The fusion times of slaps and cylinders, *ASME Paper* No. 61-WA-179.

Biot, M.A., [1957], New Methods in heat flow analysis with applications to flight structures, *Journal Aero. Sci.* **24**, No.12, 857.

Carslaw, H.S., & Jaeger, J.C., [1959], *Conduction of Heat in Solids*, Oxford University Press, London, p. 296.

Chung, T.F., & Yeh, L.T., [1975], Solidification and melting of materials subject to convection and radiation, *J. Spacecraft* **12**, No. 6.

Clark, J.A., [1965], A review of pressurization, stratification, and interfacial phenomena, *International Advances in Cryorgenic Engineering*, Plenum Press, New York, p. 259.

Cochran, D.L., Rate of solidification, application and extension of theory, Tech. Report, No. 24, Stanford University, Stanford, California.

Crandall, S.H., [1956], *Engineering Analysis*, McGraw-Hill, New York, N.Y., p. 380.

Decev, A.B., [1955], On the two-dimensional Stafan's problem, *Dokl. Akad. Nauk SSSR.* **101**, 441.

Dewey, C.F., Schlesinger, S.I., & Sashkin, L., [1960], Temperature profiles in a finite solid with moving boundary, *J. Aero/Space Sci.* **27**, 59.

Evans, L.B., Reid, R.C., & Drake, E.M., [1968], Transient natural convection in a vertical cylinder, *A.I.Ch.E. J.* **14**(2), 251.

Goodling, J.S., & Khader, M.S., [1976], Results of the numerical Solution for outward solidification with flux boundary conditions, *Trans. ASME*, May.

Goodman, T.R., [1958], The heat balance integral and its applications to problems involving a change of phase, *Trans. Am. Soc. Mech. Engrs* **80**, 335

Hess, C.F., [1979] Experimental and numerical investigation of natural convection in cylindrical enclosures, Ph.D Thesis, University of California, Berkeley.

Hess, C.F., & Miller, C.W., [1979], Natural convection in a vertical cylinder subject to constant heat flux, *Int. J. of Heat and Mass Transfer* **22** , 421.

Ingersoll, L.R., Adler, F.T., Plass, H.J., & Ingersoll, A.C., [1950], Theory of earth heat exchagers for the heat pump, *Heat. Pip. Air Condit.* **22**, 113.

Jacob, M., [1957], *Heat Transfer*, Vol. **2**, p. 208. John Wiley, New York.

Kreith, F., & Romie, F.E., [1955], A study of the thermal diffusion equation with boundary conditions corresponding to solidification or melting of materials initially at fusion temperature, *Proc. Phys. Soc., London* **68**, (B), 283.

Koeger, P.G., & Ostrach, S., [1974], The solution of a two dimensional freezing problem including convection effects in the liquid region, *Int. J. Heat Transfer* **17**, 1191.

Lajaridis, A., [1970], A numerical solution of the multi-dimensional solidification (or melting) problem, *Int. J. of Heat and Mass Transfer* **13**, 1459.

Lighthill, M.J., [1953], Theoretical considerations on free convection in tubes, *Quart. J. Mech. Appl. Math.* **6**, 398.

London, A.L., & Seban, R.A., [1943], Rate of ice-formation, *Trans. Am. Soc. Mech. Engrs.* **65**, 771.

Lowan, A.N., [1957], Operator approach to problems of stability and convergence, *scripta mathematica*, Yechiva university.

Miles, J.W., [1950], A note on Riemann's method applied to the diffusion equation, *Quart. J. Mech. Appl. Math.* **8**, 95.

Miller, C.W., [1977], The effect of a thermally-conducting wall on a stratified fluid in a cylinder, *Heat Transfer and Thermal Control Systems Progress in Astronautics and Aeronautics* **60**, 190.

Murray, W.D., & Landis, F., [1959], Numerical and machine solutions of transient heat-conduction problems involving melting or freezing, *J. Heat Transfer, Trans. ASME*, (C), **81**, p. 106.

Ostrach S. & Thornton, P.R., [1958], On the stagnation of natral convection flows in closed-end tubes, *Trans. Am. Soc. Mech. Engrs.* **80**(2), 363.

Pekeris, C.L., & Slichter, L.B., [1939], Problem of ice formation, *J. Appl. Phys.* **10**, 135.

Rubinstein, L.I., [1951], Heat transfer in a two-phase medium in the case of cylindrical symmetry, *Dokl. Akad. Nauk. SSSR.* **79**, 945.

Sfeir, P.G., & Clumpner, J.A., [1977], Continuous casting of cylindrical ingots, *J. of Heat Transfer*, February, p. 29.

Shamsunder, N., & Sparrow, E.M., [1975], Analysis of multi-dimensional condition phase change via the enthalpy model, *ASME J. of Heat Transfer*, August, p. 330.

Siegel, R., [1958], Transient Free convection from a vertical flat plate, *Trans. Am. Soc. Mech. Engrs* **80**(2), 347.

Sparrow, E.M., & Gregg, J.L., [1956], Laminar free convection from a vertical plate with uniform surface heat flux, *Trans. Am. Soc. Mech. Engrs* **78**, 435

Springer, G.S., & Olson, D.R., [1963], Axisymmetric solidifidation and melting of materials, *ASME Paper* No. 63-WA-185.

Springer, G.S., & Olson, D.R., [1962], Method of solution of axisymmetric solidifidation and melting problems, *ASME Paper* No. 62-WA-246.

Stefan, J., *Ann. Phys., Chem.* **42**, 269.

Veryeri, E., [1978], A theoretical and experimental study of a thermally conducting wall on a stratified fluid in a cylinder with a step increase temperature at the top, Ms. thesis, University of California, Berkeley.

Yan. M.M., & Huang, P.N.S., [1977], Perturbation solutions to phase change problem subject to radiation and convection, *J. of Heat Transfer.*

Yeh., L.T., & Chung, B.T.F., [1976], Transient heat conduction in a finite medium with phase change, *J. of Heat Transfer*, July.

APPENDIX

FOURIER (von NEUMANN) STABILITY ANALYSIS FOR 2-D AXISYMMETRIC HEAT EQUATION

A finite-difference approximation to a partial differential equation may be consistent but the solution will not necessarily converge to the solution of the PDE. According to the Lax Equivalence theorem [see Anderson, 1984] a stable numerical method must also be used. Purpose of the analysis in this section is to derive a conditional atability requirement on the time step and the spatial mesh spacing for the heat equation which was treated in Chapter II via Fourier or von Neumann stability analysis.

Consider the two-dimensional axisymmetric heat equation (see Equation 2.2):

$$\frac{\partial u}{\partial t} = \beta \left(\frac{\partial^2 u}{\partial r^2} + \frac{1}{r}\frac{\partial u}{\partial r} + \frac{\partial^2 u}{\partial z^2} \right) \tag{1}$$

The simple explicit finite-difference approximation for this problem is:

$$\frac{u_{j,k}^{n+1} - u_{j,k}^{n}}{\Delta t} = \beta \left[\left(\frac{u_{j+1,k}^{n} - 2u_{j,k}^{n} + u_{j-1,k}^{n}}{(\Delta r)^2} \right) + \frac{1}{j\Delta r}\left(u_{j+1,k}^{n} - u_{j-1,k}^{n} \right) \left(\frac{u_{j,k+1}^{n} - 2u_{j,k}^{n} + u_{j,k-1}^{n}}{(\Delta z)^2} \right) \right] \tag{2}$$

Or

$$u_{j,k}^{n+1} = u_{j,k}^{n} + r_1\left(u_{j+1,k}^{n} - 2u_{j,k}^{n} + u_{j-1,k}^{n}\right) + r_2\left(u_{j+1,k}^{n} - u_{j-1,k}^{n}\right) + r_3\left(u_{j,k+1}^{n} - 2u_{j,k}^{n} + u_{j,k-1}^{n}\right) \tag{3}$$

where

$$\begin{aligned} r_1 &= \beta(\Delta t/\Delta r^2) \\ r_2 &= \beta(\Delta t/2j\Delta r^2) \\ r_3 &= \beta(\Delta t/\Delta z^2) \end{aligned} \tag{4}$$

In this case a Fourier component of the form is assumed:

$$u_{j,k}^{n} = e^{at}\, e^{ik_r r}\, e^{ik_z z} \tag{5}$$

where k_r and k_z are the wave numbers for r and z coordinates respectively.

If Equation (5) is substituted into Equation (3) we obtain

$$\begin{aligned} e^{a(t+\Delta t)}\, e^{ik_r r}\, e^{ik_z z} = e^{at}\, e^{ik_r r}\, e^{ik_z z} &+ (r_1 + r_2)e^{at}\, e^{ik_r(r+\Delta r)}\, e^{ik_z z} \\ &+ (r_1 - r_2)e^{at}\, e^{ik_r(r-\Delta r)}\, e^{ik_z z} \\ &- 2(r_1 + r_3)e^{at}\, e^{ik_r r}\, e^{ik_z z} \\ &+ r_3 e^{at}\, e^{ik_r r}\, e^{ik_z(z+\Delta z)} \\ &+ r_3 e^{at}\, e^{ik_r r}\, e^{ik_z(z-\Delta z)} \end{aligned} \tag{6}$$

if we divide by $e^{at}\, e^{ik_r r}\, e^{ik_z z}$ and utilize the relation

$$\cos\beta = \frac{e^{i\beta} + e^{-i\beta}}{2} \quad \text{and} \quad \sin\beta = \frac{e^{i\beta} - e^{-i\beta}}{2}$$

the above expression in Equation (6) becomes

$$
\begin{aligned}
e^{a\Delta t} &= 1 + (r_1 + r_2)e^{ik_r\Delta r} + (r_1 - r_2)e^{-ik_r\Delta r} - 2(r_1 + r_3) \\
&\quad + r_3(e^{ik_z\Delta z} + e^{-ik_z\Delta z}) \\
&= 1 + r_1(e^{ik_r\Delta r} + e^{-ik_r\Delta r}) + r_2(e^{ik_r\Delta r} - e^{-ik_r\Delta r}) \\
&\quad + r_3(e^{ik_z\Delta z} + e^{-ik_z\Delta z}) - 2r_1 - 2r_3 \\
&= 1 + 2r_1\left(\frac{e^{ik_r\Delta r} + e^{-ik_r\Delta r}}{2} - 1\right) + 2r_2\left(\frac{e^{ik_r\Delta r} - e^{-ik_r\Delta r}}{2}\right) \\
&\quad + 2r_3\left(\frac{e^{ik_z\Delta z} + e^{-ik_z\Delta z}}{2} - 1\right) \\
&= 1 + 2r_1(\cos\beta_1 - 1) + 2r_3(\cos\beta_2 - 1) + 2r_2\, i \sin\beta_1
\end{aligned}
$$

where $\beta_1 = k_r\Delta r$ and $\beta_2 = k_z\Delta z$. Employing the trigonometric identity

$$\sin^2\frac{\beta}{2} = \frac{1 - \cos\beta}{2}$$

the amplification factor is

$$G = e^{a\Delta t} = 1 - 4r_1\sin^2\frac{\beta_1}{2} - 4r_3\sin^2\frac{\beta_2}{2} + 2r_2\, i\sin\beta_1 \tag{7}$$

Thus for stability;

$$|G| \le 1 \tag{8}$$

where

$$
\begin{aligned}
|G| &= \left|1 - 4r_1\sin^2\frac{\beta_1}{2} - 4r_3\sin^2\frac{\beta_2}{2} + 2r_2\, i\sin\beta_1\right| \\
&= \sqrt{\left\{1 - 4r_1\sin^2\frac{\beta_1}{2} - 4r_3\sin^2\frac{\beta_2}{2}\right\}^2 + (2r_2\, i\sin\beta_1)^2}
\end{aligned} \tag{9}
$$

After rearranging the Equation (9), the stability requirement Equation (8) is then

$$
\begin{aligned}
&1 + 16r_1^2\sin^4\frac{\beta_1}{2} + 16r_3^2\sin^4\frac{\beta_2}{2} - 8r_1\sin^2\frac{\beta_1}{2} - 8r_3\sin^2\frac{\beta_2}{2} \\
&\quad 32r_1r_3\sin^2\frac{\beta_1}{2}\sin^2\frac{\beta_2}{2} + 4r_2^2\sin^2\beta_1 \le 1
\end{aligned} \tag{10}
$$

Further reduction yields

$$4r_1^2 + 4r_3^2 - 2r_1 - 2r_3 + 8r_1r_3 + r_2^2 \leq 0$$

Substituting r_1, r_2, and r_3 from Equation (4) gives

$$\frac{4\beta^2\Delta t^2}{\Delta r^4} + \frac{4\beta^2\Delta t^2}{\Delta z^4} - 2\frac{\beta\Delta t}{\Delta r^2} - 2\frac{\beta\Delta T}{\Delta z^2} + 8\frac{\beta^2\Delta t^2}{\Delta r^2\Delta z^2} + \frac{\beta^2\Delta t^2}{4\Delta r^2} \leq 0$$

which yields the following constraint on the size of the time step relative to the size of the mesh spacing:

$$\Delta t \leq \frac{8}{\beta}\frac{\Delta r^2\,\Delta z^2\,(\Delta r^2 + \Delta z^2)}{16\Delta r^4 + 16\Delta z^4 + 32\Delta r^2\Delta z^2 + \Delta r^2\Delta z^4} \tag{11}$$

The Equation (11) ,which is the same equation as Equation 2.3 in Chapter II, has been used for explicit method of phase change problem in the chapter.